ABSTRACT

Title of Document: PIEZOELECTRIC VIBRATION ENERGY HARVESTING FROM COUPLED STRUCTURAL-ACOUSTIC SYSTEMS

Abdulaziz Aladwani
Doctor of Philosophy, 2013

Directed By: Professor Amr Baz
Department of Mechanical Engineering

A comprehensive theoretical and experimental study of the fundamentals and the underlying phenomena governing the operation of piezoelectric vibration energy harvesting from coupled structural-acoustic systems is presented. Analytical and finite element models are developed based on variational formulations to describe the energy harvesting from uncoupled structural elements as well as structural elements coupled with acoustic cavities. The models enable the predictions of the structural displacement, output electric voltage, and fluid pressure for various loading conditions on the energy harvesting system. The developed models also include dynamic magnification means to enhance the energy harvesting capabilities and enable harnessing of the vibration energy over a broader operating frequency range.

The predictions of all the models are experimentally validated by using structural elements varying from beams to plates. Close agreements are demonstrated between the theoretical predictions and the obtained experimental results.

The theoretical and experimental tools developed, in this dissertation, provide invaluable means for designing a wide variety of efficient energy harvesters for harnessing the vibrational energy inside automobiles, helicopters, aircrafts, and other types of structures that interact internally or externally with a fluid medium. With such harnessed energy, a slew of on-board sensors can be powered to enable the continuous monitoring of the condition and health of these structures without the need for external power sources.

PIEZOELECTRIC VIBRATION ENERGY HARVESTING FROM COUPLED STRUCTURAL-ACOUSTIC SYSTEMS

By

Abdulaziz Aladwani

Dissertation submitted to the Faculty of the Graduate School of the
University of Maryland, College Park, in partial fulfillment
of the requirements for the degree of
Doctor of Philosophy
2013

Advisory Committee:
Professor Amr Baz, Chair
Professor Balakumar Balachandran
Professor Don DeVoe
Professor Jin-Oh Hahn
Professor Inderjit Chopra (Dean's Representative)

© Copyright by
Abdulaziz Aladwani
2013

Dedication

To …

first and foremost …

my parents, *Khadija* and *Ebrahim*

and my children *Ghalia* and *Saoud*

… for their invaluable support and patience.

and my country *Kuwait*

… for giving me the opportunity to pursue my graduate studies

Acknowledgements

I would like to thank my professor, Prof. Amr Baz for he has been more than an academic advisor over the last four years. Throughout my entire PhD study, he has been available for any kind of support. He has been a great mentor who provided me with endless amount of technical as well as non-technical advice.

I would like to express my gratitude to the most beloved person in my life, my mother Khadija for giving me all her time. My daughter Ghalia and my son Saoud for their patience.

Last but not least, I would like to extend my thanks to all my friends who have given me helpful encouragement and support and for making the lab such a joyful place to work at. They provided a very pleasant academic environment inside the lab and were more than friends outside the lab. I would like to thank Mostafa for taking the time to teach me everything I needed about the lab instruments. I would like to thank my very close friend Hajid for his continuous advice. Yaser, Laith, Mohammed Raafat, Saeed, Mohammed Maqsoud, Yaqoub, Jason, Abdullah, and all other friends.

Table of Contents

Table of Contents iv
List of Tables vi
List of Figures vii
Chapter 1 1
1. Introduction 1
1.1. Energy Harvesting using Piezoelectric Vibration 1
1.2. Objective and Scope of Dissertation 4
Chapter 2 6
2. Piezoelectric Energy Harvester with a Dynamic Magnifier: Analytical and Numerical Analysis 6
2.1. Introduction 6
2.2. Concept of Energy Harvester with a Dynamic Magnifier 6
2.3. Analytical Modeling of Energy Harvester with a Dynamic Magnifier 8
2.3.1. Kinetic Energy (T) 9
2.3.2. Potential Energy (U) 10
2.3.3. Electric Energy (W_e) 11
2.3.4. Undamped Equations of Motion 13
2.3.5. Damped Equations of Motion 18
2.4. Finite Element Modeling of Energy Harvester with a Dynamic Magnifier 21
2.4.1. *Kinetic Energy* (T) 22
2.4.2. Potential Energy (U) 24
2.4.3. Electric Energy (W_e) 26
2.4.4. Undamped Equations of Motion 28
2.4.5. Damped Equations of Motion 29
2.5. Performance of the cantilevered piezoelectric energy harvester 32
2.5.1. Performance of the CPEH 32
2.5.2. Performance of the CPEHDM 35
2.6. Conclusions 43
Chapter 3 44
3. Experimental Implementation of a Piezoelectric Energy Harvester with a Dynamic Magnifier 44
3.1. Introduction 44
3.2. Finite Element Modeling 45
3.3. Experimental and Numerical Results 47
3.4. Conclusions 52
Chapter 4 53
4. Finite Element Modeling of Piezoelectric Vibration Energy Harvesting from Coupled Structural-Acoustic Systems 53
4.1. Introduction 53
4.2. Theoretical Formulation 54

4.3. A Two-Dimensional Energy Harvesting System 57
4.4. Finite Element Discretization 60
4.5. Structure and Fluid Damping 65
4.6. Numerical Results 66
4.7. A Two-Dimensional Energy Harvester with a Dynamic Magnifier 75
4.8. A Three-Dimensional Energy Harvesting System 83
4.9. Conclusions 94
Chapter 5 96
5. Experimental Implementation of Piezoelectric Vibration Energy Harvesting from Coupled Structural-Acoustic Systems 96
5.1. Introduction 96
5.2. Finite Element Modeling 98
5.3. Experimental and Numerical Results 100
5.4. Summary 104
Chapter 6 106
6. Conclusions and Future Work 106
6.1. Summary 106
6.2. Recommendations and Future Work 108
Bibliography 112
Appendices 110

List of Tables

Table 2.1: Geometric and material properties of the energy harvester [40] 34
Table 4.1: Geometric, structure, fluid, and electromechanical properties of the coupled system..... 67
Table 4.2: First six natural frequencies (*Hz*) of the composite beam alone..... 68
Table 4.3: First six natural frequencies (*Hz*) of the cavity alone 69
Table 4.4: First six natural frequencies (*Hz*) of the coupled system for all-rigid fluid boundary condition 70
Table 4.5: First six natural frequencies (*Hz*) of the coupled system for one-side open fluid boundary condition..... 70
Table 4.6: First six natural frequencies (*Hz*) of the composite plate alone..... 87
Table 4.7: First six natural frequencies (*Hz*) of the cavity alone 87
Table 4.8: Geometric, structure, fluid, and electromechanical properties of the coupled system..... 88
Table 4.9: First six natural frequencies (*Hz*) of the coupled system for all-rigid fluid boundary condition 90
Table 4.10: First six natural frequencies (*Hz*) of the coupled system for one-side open fluid boundary condition..... 91
Table 5.1: Geometric, structure, fluid, and electromechanical properties of the experimental setup shown in Figure 5.1 101

List of Figures

Figure 2.1: *CPEH* with series connection of piezoelectric patches 7
Figure 2.2: *CPEHDM* with series connection of piezoelectric patches 8
Figure 2.3: Original and deflected positions of the cantilevered piezoelectric energy harvester with dynamic magnifier 9
Figure 2.4: *CPEHDM* with series connection of piezoelectric patches 22
Figure 2.5: Effect of the load resistance on the peak amplitude of the electric power output of the *CPEH* for base excitations at the short-circuit (▬▬▬ distributed parameter, ○ finite element) and open-circuit (▪▪▪▪▪▪▪▪▪ distributed parameter, □ finite element) resonant frequencies of the first vibration mode 35
Figure 2.6: Effect of the excitation frequency on the peak amplitude of the electric power output of the *CPEH* for the short-circuit resonant condition (▬▬▬ distributed parameter, ○ finite element)..... 36
Figure 2.7: Effect of the load resistance (a) and excitation frequency (b) on the peak amplitude of the electric power output for the *CPEHDM* (▬▬▬ distributed parameter, ○ finite element) with $M_f=M$ and the *CPEH* (▪▪▪▪▪▪▪▪▪ distributed parameter, □ finite element) at the short-circuit condition of the first vibration mode 39
Figure 2.8: Effect of the load resistance (a) and excitation frequency (b) on the peak amplitude of the electric power output for the *CPEHDM* (▬▬▬ distributed parameter, ○ finite element) with $M_f=5M$ and the *CPEH* (▪▪▪▪▪▪▪▪▪ distributed parameter, □ finite element) at the short-circuit condition of the first vibration mode 40
Figure 2.9: Effect of the load resistance (a) and excitation frequency (b) on the peak amplitude of the electric power output for the *CPEHDM* (▬▬▬ distributed parameter, ○ finite element) with $M_f=10M$ and the *CPEH* (▪▪▪▪▪▪▪▪▪ distributed parameter, □ finite element) at the short-circuit condition of the first vibration mode 41
Figure 2.10: Effect of the load resistance (a) and excitation frequency (b) on the peak amplitude of the electric power output for the *CPEHDM* (▬▬▬ distributed parameter, ○ finite element) with $M_f=15M$ and the *CPEH* (▪▪▪▪▪▪▪▪▪ distributed parameter, □ finite element) at the short-circuit condition of the first vibration mode 42
Figure 3.1: A photograph showing the experimental setup of the *CPEHDM* system 45
Figure 3.2: Test arrangements of the *CPEH* and *CPEHDM* systems 48
Figure 3.3: Experimental ○ vs. numerical ▬▬▬ output voltage of the test arrangement shown 49
Figure 3.4: Experimental ○ vs. numerical ▬▬▬ output voltage of the test arrangement shown 50
Figure 3.5: Experimental ○ vs. numerical ▬▬▬ output voltage of the test arrangement shown 51
Figure 3.6: Experimental ○ vs. numerical ▬▬▬ output voltage of the test arrangement shown 51
Figure 4.1: A general interior-fluid/piezoelectric-structure coupled problem 54

Figure 4.2: The two-dimensional coupled system: (a) square cavity filled with air, (b) bimorph energy harvester with series connection of piezoelectric patches 58
Figure 4.3: First six mode shapes of the composite beam alone 68
Figure 4.4: First six mode shapes of the rigid cavity alone 69
Figure 4.5: First six mode shapes of the one-side open cavity alone 70
Figure 4.6: First six mode shapes of the coupled system with rigid cavity at the short-circuit condition 71
Figure 4.7: First six mode shapes of the coupled system with open cavity at the short-circuit condition 72
Figure 4.8: Voltage FRF of the piezoelectric energy harvester for different resistive loads 73
Figure 4.9: Current FRF of the piezoelectric energy harvester for different resistive loads 74
Figure 4.10: Power FRF of the piezoelectric energy harvester for different resistive loads 74
Figure 4.11: Variation of electric power with load resistance at the *SC* and *OC* resonant conditions of the first coupled vibration mode..... 75
Figure 4.12: The two-dimensional coupled system with a dynamic magnifier: (a) square cavity filled with air, (b) bimorph energy harvester with series connection of piezoelectric patches and attached to a dynamic magnifier..... 76
Figure 4.13: Power FRF of the piezoelectric energy harvester for different resistive loads 82
Figure 4.14: Variation of electric power with load resistance at the *SC* resonant conditions of the first coupled vibration mode (——— with magnifier, ▪▪▪▪▪▪▪▪▪ without magnifier) 83
Figure 4.15: The three-dimensional structural-acoustic coupled energy harvesting system 84
Figure 4.16: First six mode shapes of the composite plate alone 89
Figure 4.17: First six mode shapes of the rigid cavity alone 89
Figure 4.18: First six mode shapes of the one-side open cavity alone 90
Figure 4.19: First six mode shapes of the coupled system with rigid cavity at the short-circuit condition..... 91
Figure 4.20: First six mode shapes of the coupled system with open cavity at the short-circuit condition..... 92
Figure 4.21: Voltage *FRF* of the piezoelectric energy harvester plate for different resistive loads..... 93
Figure 4.22: Current FRF of the piezoelectric energy harvester plate for different resistive loads..... 93
Figure 4.23: Power *FRF* of the piezoelectric energy harvester plate for different resistive loads..... 94
Figure 5.1: A photograph showing the experimental setup of the structural-acoustic coupled system..... 97
Figure 5.2: Piezoelectric patches connected to the front view (a) and back view (b) of the all-fixed aluminum plate substructure..... 97
Figure 5.3: Fundamental mode shape of the coupled system: (a) Experimental (plate), (b) Numerical (plate and acoustic cavity)..... 102

Figure 5.4: Experimental ○ vs. numerical ▬▬▬ output voltage of the coupled system for: (a) R_L=*1 kohm*, (b) R_L=*10 kohm*, (c) R_L=*100 kohm*, and (d) R_L=*1 Mohm* 103
Figure 5.5: Variation of electric power with load resistance at the SC resonant conditions of the first coupled vibration mode (Experimental ○ vs. numerical ▬▬▬) 104

Nomenclature

A_r	modal amplitude constant
b	width of beam and piezoelectric layers
$\mathbf{B}$	global vector of piezoelectric action
$\mathbf{B}_e$	element vector of piezoelectric action
c_a	viscous air damping coefficient
c_F	speed of sound in the fluid
c_{11}^E	Young's modulus of the piezoelectric layers at constant electric field
c_{ijkl}	elastic material constants
C_p	internal capacitance of a single piezo-layer
$c_s I_t$	equivalent damping term due to structural viscoelasticity
$\mathbf{C}_{up}$	global fluid-structure coupling matrix
$\bar{\mathbf{C}}_{up}$	mass normalized fluid-structure coupling matrix
$\mathbf{C}_{uV}$	global electromechanical coupling matrix
$\bar{\mathbf{C}}_{uV}$	mass normalized electromechanical coupling matrix
d_{31}	piezoelectric strain constant
D_i	electrical displacement vector components
$\mathbf{D}_a$	global damping matrix due to viscous air damping
$\mathbf{D}_s$	global damping matrix due to structural viscoelasticity
$\mathbf{D}_{uu}$	total global mechanical damping matrix
$\bar{\mathbf{D}}_{uu}$	total global mechanical mass normalized damping matrix
$\bar{\mathbf{D}}_{pp}$	mass normalized fluid damping matrix
e_{kij}	piezoelectric material constants
E_k	electric field vector components
$E_b I_b$	flexural rigidity of the beam
$E_t I_t$	flexural rigidity of the piezo-beam
f_r	modal mechanical forcing function
F_r	amplitude modal mechanical forcing function
$\mathbf{F}$	global vector of applied mechanical force
$\bar{\mathbf{F}}$	modal mechanical forcing vector
$\bar{\mathbf{F}}_0$	amplitude of modal mechanical forcing vector
h	half the thickness of the beam
$\mathbf{h}_u$	structure vector of modal coordinates
$\mathbf{h}_p$	fluid vector of modal coordinates
$H(x)$	Heaviside function

$\mathbf{H}_{ou}$	amplitude of structure vector of modal coordinates
$\mathbf{H}_{op}$	amplitude of fluid vector of modal coordinates
I	electric current
j	unit imaginary number
k_f	stiffness of the magnifier spring
$\mathbf{K}_b$	global stiffness matrix of the piezo-beam
$\mathbf{K}_e$	element stiffness matrix of the piezo-beam
$\mathbf{K}_F$	global stiffness matrix of the magnifier spring
$\mathbf{K}_{uu}$	total global mechanical stiffness matrix
$\bar{\mathbf{K}}_{uu}$	total global mechanical mass normalized stiffness matrix
$\mathbf{K}_{pp}$	global fluid stiffness matrix
$\bar{\mathbf{K}}_{pp}$	mass normalized fluid stiffness matrix
$\mathbf{K}_{VV}$	global electric stiffness matrix
L	length of the piezo-beam
L_e	length of the eth element of the piezo-beam
L	Lagrangian
m_b	mass per unit length of the beam
m_p	mass per unit length of a single piezo-layer
m_t	mass per unit length of the piezo-beam
M	end mass
M_f	magnifier mass
$\mathbf{M}_b$	global mass matrix of the piezo-beam
$\mathbf{M}_e$	element mass matrix of the piezo-beam
$\mathbf{M}_F$	global mass matrix of the magnifier mass
$\mathbf{M}_L$	global mass matrix of the end mass
$\mathbf{M}_{uu}$	total global mechanical mass matrix
$\bar{\mathbf{M}}_{uu}$	total global mechanical mass normalized mass matrix
$\mathbf{M}_{pp}$	global fluid mass matrix
$\bar{\mathbf{M}}_{pp}$	mass normalized fluid mass matrix
n_i^S	unit normal external to Ω_S
n_i	unit normal external to Ω_F
N	total number of finite elements
$\mathbf{N}$	appropriate interpolating vector
$\mathbf{N}_S$	matrix of structure shape functions
$\mathbf{N}_F$	matrix of fluid shape functions
p	interior-fluid pressure

p_n	fluid pressure of node n
P	output electrical power of the energy harvester
$\mathbf{P}$	global vector of fluid degrees of freedom
$\mathbf{P}^e$	element vector of fluid degrees of freedom
Q	electric charge collected in the piezoelectric layers
Q_0	amplitude of the electric charge collected in the piezoelectric layers
Q_{nc_Q}	non-conservative electrical potential associated with the electrical charge
$\mathbf{Q}_{nc_\mathbf{U}}$	non-conservative mechanical force vector associated with the deflection vector
$\mathbf{Q}$	global vector of electric charge densities
R_L	electrical load resistance
S_1	strain in the piezoelectric layers
t	time
t_b	thickness of the beam
t_p	thickness of a single piezoelectric layer
T	total kinetic energy
T_0	kinetic energy of the magnifier mass
T_1	stress in the piezoelectric layers
T_e	kinetic energy of the eth element of the piezo-beam
T_L	kinetic energy of the end mass
u_i	mechanical displacement components
U	total potential energy
U_0	potential energy of the magnifier spring
U_e	potential energy of the eth element of the piezo-beam
$\mathbf{U}$	global nodal deflection vector of the piezo-beam relative to x-z
$\mathbf{U}_b$	element nodal displacement vector of the base relative to X-Z
$\mathbf{U}_{base}$	global nodal displacement vector of the base relative to X-Z
$\mathbf{U}_e$	element nodal deflection vector of the piezo-beam relative to x-z
V_P	electrical voltage across P^{th} piezoelectric patch
V_T	electrical voltage across the resistive electrical load
$\mathbf{V}$	global vector of electric degrees of freedom
w_b	displacement of the base relative to X-Z
w_e	transverse deflection of the eth element of the piezo-beam relative to x-z
w_{e_0}	transverse deflection of the magnifier mass relative to x-z
w_{e_L}	transverse deflection of the end mass relative to x-z
w_{e_i}	transverse deflection of the eth element of the piezo-beam at node i

$w_{e_i,x'}$	slope of the eth element of the piezo-beam at node i
w_{e_j}	transverse deflection of the eth element of the piezo-beam at node j
$w_{e_j,x'}$	slope of the eth element of the piezo-beam at node j
$w_{e_{x'}}$	transverse deflection of the eth element of the piezo-beam at x' relative to x-z
w_0	transverse deflection of the magnifier mass relative to X-Z
w_L	transverse deflection of the end mass relative to X-Z
w_m	structure transverse displacement of node m
W_r	mass normalized eigenfunction of the rth mode
W_e	electrical energy
X, Z	inertial coordinates
x, z	base-fixed coordinates
x', z'	element local coordinates
$\bar{\mathbf{Z}}_u$	structure impedance matrix
$\bar{\mathbf{Z}}_p$	fluid impedance matrix

Greek Symbols

α, β	weighting constants of proportionality for fluid damping matrix
δ	variation operator
$\delta(x)$	Dirac delta function
$\mathbf{\Delta}_r$	mass normalized eigenvector of the rth mode
$\mathbf{\Delta}_b$	amplitude of the element nodal displacement vector of the base relative to X-Z
$\mathbf{\Delta}_{base}$	amplitude of the global nodal displacement vector of the base relative to X-Z
$\in_{33}^{S}$	permittivity at constant strain
$\in_{33}^{T}$	permittivity at constant stress
$\in_0$	permittivity of free space
$\in_{ik}$	dielectric material constants
ε_{kl}	strain tensor components
η_r	modal mechanical response of the rth mode
$\boldsymbol{\eta}$	global nodal vector of modal mechanical response
Π_r	amplitude of modal mechanical response of the rth mode
$\mathbf{\Pi}$	amplitude of the global nodal vector of modal mechanical response
ψ	electric potential
Ψ_r	electromechanical coupling term of the rth mode

$\mathbf{\Psi}$	electromechanical coupling vector
$\mathbf{\Phi}_u$	fluid mass normalized modal matrix
$\mathbf{\Phi}_p$	structure mass normalized modal matrix
Ω_p	volume of the piezoelectric layers in one finite element
Ω_F	domain occupying interior-fluid
Ω_S	domain occupying piezoelectric-structure
Γ_u	part of piezoelectric-structure exterior boundary subjected to prescribed displacement
Γ_σ	part of piezoelectric-structure exterior boundary subjected to prescribed force density
Γ_ψ	part of piezoelectric-structure exterior boundary subjected to prescribed electric potential
Γ_D	part of piezoelectric-structure exterior boundary subjected to prescribed electric charge density
Γ_p	part of interior-fluid exterior boundary subjected to pre*SC*ribed fluid pressure
ρ_F	fluid mass density
ρ_S	structure mass density
σ_{ij}	stress tensor components
Σ	interface between piezoelectric-structure and interior-fluid
Σ_R	interface between rigid cavity walls and interior-fluid
θ_m	structure rotation of node m
ω	excitation frequency
ω_r	natural frequency of the rth mode under *SC* condition
$\hat{\omega}_r$	natural frequency of the rth mode in the absence of the magnifier and the end mass
ζ_r	mechanical damping ratio of the rth mode
ζ_r^a	mechanical damping ratio of the rth mode due to viscous air damping
ζ_r^s	mechanical damping ratio of the rth mode due to structural viscoelasticity

Subscript

$1,2,3$	directions 1,2,3
a	air
b	base structure
d	prescribed quantity
e	elementary
f	dynamic magnifier

F	fluid
L	load
nc	non-conservative
p, P	piezoelectric
r	r^{th} mode of vibration
s, S	structural

Superscript

E	property measured at constant electric field
ε, S	property measured at constant strain
σ, T	property measured at constant stress

Chapter 1

1. Introduction

1.1. Energy Harvesting using Piezoelectric Vibration

Harnessing of energy from ambient vibration using piezoelectric materials has been recognized as a viable means for powering small electronic devices and remote sensors in order to eliminate their dependence on external power sources [2-4]. Piezoelectricity is a form of mechanical-to-electrical or electrical-to-mechanical coupling where piezoelectric materials are used to achieve this goal through the direct or the converse piezoelectric effects. With such self-powered capabilities, these devices and sensors can operate in an uninterrupted fashion over prolonged periods of time. In fact, there are three vibration based energy harvesting techniques as described by Williams and Yates [5]. These include electromagnetic, electrostatic, and piezoelectric transductions. However, the latter received more attention from researchers in the last decade. In the open literature, piezoelectric energy harvester models range from simple lumped parameter models to fairly sophisticated distributed parameter models [6-15]. These include both, deterministic and undeterministic models.

Most of the exerted efforts place a particular emphasis on maximizing the harvested power transmitted to the output load by using various innovative approaches. On the top of the list of these approaches is the exploitation of the concept of impedance matching between the piezoelectric energy harvester and the

electrical load as reported, for example, by Kong *et al*. [16], Liang and Liao [17], Stephen [18], and Chen *et al* [19]. However, several other concepts have also been considered. Among these concepts is the use of a tunable resonant frequency power harvesting device to continuously match the time-varying frequency of the external vibration in real time as reported by Wu *et al*. [20]. Another concept developed by Badel *et al.* [21] relies on the use of a harvester augmented with an electrical switching device in which the switch is triggered to maximize the output voltage of the harvester. Other approaches are devised by duToit [7] and duToit *et al.* [8] where the optimal parameters of single degree of freedom harvesters are selected to maximize the extracted power when mechanical damping is neglected. Daqaq *et al*. [6] and Renno *et al*. [22] extended the work of duToit [7] and duToit *et al.* [8] to include the effects of damping and electromechanical coupling when optimizing the harvester output power. These attempts have been extended to theoretically optimize and experimentally evaluate the performance of cantilevered piezoelectric harvesters by Erturk and Inman [10,11] and DeMarqui *et al*. [14]. El-Sabbagh and Baz [15] used topology optimization techniques to maximize the power output of a circular bimorph energy harvester by assuming that the capacitances attached to the electrodes are controllable and can be optimized to maximize the power output at a given excitation frequency. In their work, they changed the topology of the energy harvester by making its thickness vary with the radius of the bimorph.

In the above studies, the interest has been focused on harvesters that are primarily linear systems. However, recent efforts are now considering maximizing the

harvested power over broad frequency range using multi-harvesters as in Xue *et al.* [23] or by exploiting different sources of nonlinearities [12,24-25].

On the other hand, problems related to fluid-structure interaction can be found in many engineering applications and is considered a relatively old and well established field as reported for example by Morand and Ohayon [27], Olson and Bathe [28], Everstine [29], and de Souza and Pedroso [30]. The field of structural-acoustic problems is an example which appears in cases of cavities containing fluid, limited by flexible and/or rigid walls [30-31]. However, most of the work done in this field over the past decade was devoted to the development, testing and modeling of noise reduction techniques using passive and/or active means [31-38]. It is well known that passive noise reduction methods are more effective at high frequencies and can be achieved by using sound absorbing materials. In the low frequency range, active techniques using piezoelectric materials are found to be more attractive.

In the open literature, most of the exerted research in energy harvesting has focused on vibration-based methods in which a piezoelectric structure is vibrated by attaching it to a vibrating base-structure [4]. However, more complex types of excitations, e.g. pressure, wind, or fluid flow have not seen as much attention so far. Recently, DeMarqui *et al*. [39] presented a frequency domain piezoaeroelastic analysis of a generator wing with continuous electrodes. The piezoaeroelastic model, they proposed, is obtained by combining an unsteady aerodynamic model with an electromechanically coupled finite element model. The subsonic unsteady aerodynamic model is based on the doublet lattice method. It was observed from their

presented work that increased electrical power output of the resistive-inductive case can be achieved with increased flutter speed.

In the present work, focus is placed on developing a comprehensive finite element modeling of energy harvesting from the structural-acoustic coupled problems. This goal is achieved by first considering a relatively simple two-dimensional model which is then generalized to the more realistic case of three-dimensional systems. The objective and scope of this thesis is explained in the following in more details.

1.2. Objective and Scope of Dissertation

The main objectives of this dissertation are to develop a comprehensive theoretical and experimental study of the fundamentals and the underlying phenomena governing the operation of piezoelectric vibration energy harvesting from coupled fluid-structure systems. With the development of theoretical and experimental tools to be presented in this dissertation, it would be possible to design a wide variety of efficient energy harvesters for harnessing the vibrational energy inside automobiles, helicopters, aircrafts, and other types of structures that interact internally and/or externally with a fluid medium. With such harnessed energy, a slew of on-board sensors can be powered to enable the continuous monitoring of the condition and health of these structures without the need for external power sources.

In order to achieve these objectives, first, a brief review is presented in Chapter 1 on the literature of energy harvesting from vibrating structures and in particular from structures interacting internally or externally with a fluid medium. Chapter 2 presents analytical and numerical analyses of piezoelectric energy

harvesters with dynamic magnification capabilities for vibrating beams. Chapter 3 includes experimental demonstration of the feasibility of the concept of energy harvesting with dynamic magnification as well as detailed comparisons between the obtained experimental results and the theoretical predictions of the models introduced in Chapter 2. In Chapter 4, 2-D and 3-D finite element modeling of piezoelectric vibration energy harvesting from coupled structural-acoustic systems is presented with and without dynamic magnification capabilities. The model enables the predictions of the energy harvesting power and efficiency at various loading conditions in an attempt to determine the optimal performance of the harvesters. Details of the modal characteristics of the uncoupled structure and the uncoupled acoustic cavity are presented along with the effect of the fluid-structure interaction when the structure is coupled with the cavity. Chapter 5 includes the experimental validation of the 3-D finite element model developed in Chapter 4. Chapter 6 summarizes the main conclusions reached at this dissertation and includes also the recommendations for future studies.

Chapter 2

2. Piezoelectric Energy Harvester with a Dynamic Magnifier: Analytical and Numerical Analysis

2.1. Introduction

Conventional energy harvesters typically consist of a cantilevered composite piezoelectric beam which has a proof mass at its free end while its fixed end is mounted on a vibrating base structure. The resulting relative motion between the beam and the base structure produces a mechanical strain in the piezoelectric layers which is converted into electric power by virtue of the direct piezoelectric effect. In this chapter, a radically different approach is considered whereby a conventional energy harvester is provided with a dynamic magnifier which consists of a spring-mass system that is placed between the fixed-end of the composite piezoelectric beam and the vibrating base structure. The main function of the dynamic magnifier, as the name implies, is to magnify the strain induced in the piezoelectric layers in order to amplify the electric power output. With proper selection of the design parameters of the dynamic magnifier, the harvested electric power can be significantly enhanced and the effective frequency bandwidth can be improved.

2.2. Concept of Energy Harvester with a Dynamic Magnifier

Figure 2.1 shows a schematic drawing of a conventional piezoelectric energy harvester (*CPEH*). Generally, the *CPEH* consists of a cantilevered composite piezoelectric beam that has an end mass M connected to its free end while its fixed end is mounted on a vibrating base structure. The resulting relative motion between

the beam and the base structure produces a mechanical strain S_1 in the piezoelectric patches which is converted to electric power by virtue of the direct piezoelectric effect. The generated power can be used to drive the resistive load R_L.

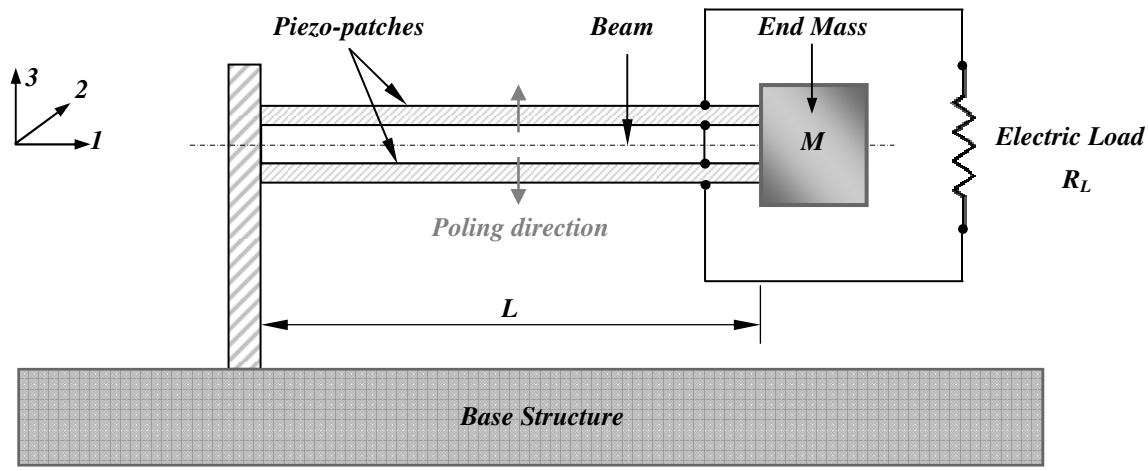

Figure 2.1: *CPEH* with series connection of piezoelectric patches

Figure 2.2 shows the proposed *CPEHDM* system which consists of a *CPEH* augmented with a dynamic magnifier. The magnifier is basically a spring k_f - mass M_f system placed between the fixed end of the composite piezoelectric beam and the base structure. The main purpose of the dynamic magnifier is to magnify the strain induced in the piezoelectric layers in order to amplify the electric power output. The obtained results demonstrate the feasibility of the *CPEHDM* as a simple and effective means for enhancing the magnitude and spectral characteristics of the *CPEH*.

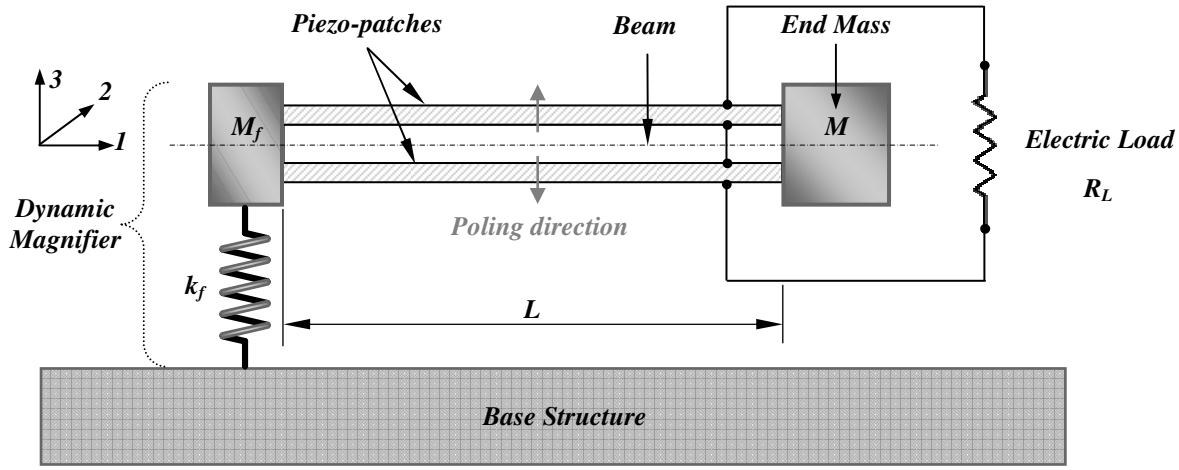

Figure 2.2: *CPEHDM* with series connection of piezoelectric patches

2.3. Analytical Modeling of Energy Harvester with a Dynamic Magnifier

In this section, an analytical model is developed to simulate the vibrations of the *CPEHDM* during its transverse oscillation around the original position as outlined in Figure 2.3. Two coordinate systems are considered here to clearly explain the kinematics of the problem. These systems are the inertial frame of reference $X-Z$ (fixed in space) and the base-fixed coordinate system $x-z$ (moving with the base).

Let $w_b(x,t)$ denote the displacement of the base relative to the inertial frame of reference $X-Z$ and $w_{rel}(x,t)$ denote the transverse deflection of the beam relative to the base-fixed coordinate system $x-z$ at any location x. Accordingly, one can write

$$w(x,t) = w_{rel}(x,t) + w_b(x,t) \tag{2.1}$$

where $w(x,t)$ is the transverse deflection of the beam relative to the inertial frame of reference $X-Z$ at the same location x where $w_{rel}(x,t)$ was defined. In addition,

$w_{rel}(0,t)$ and $w_{rel}(L,t)$ denote, respectively, the transverse deflection of the magnifier mass M_f and the end mass M relative to the moving coordinate system $x-z$.

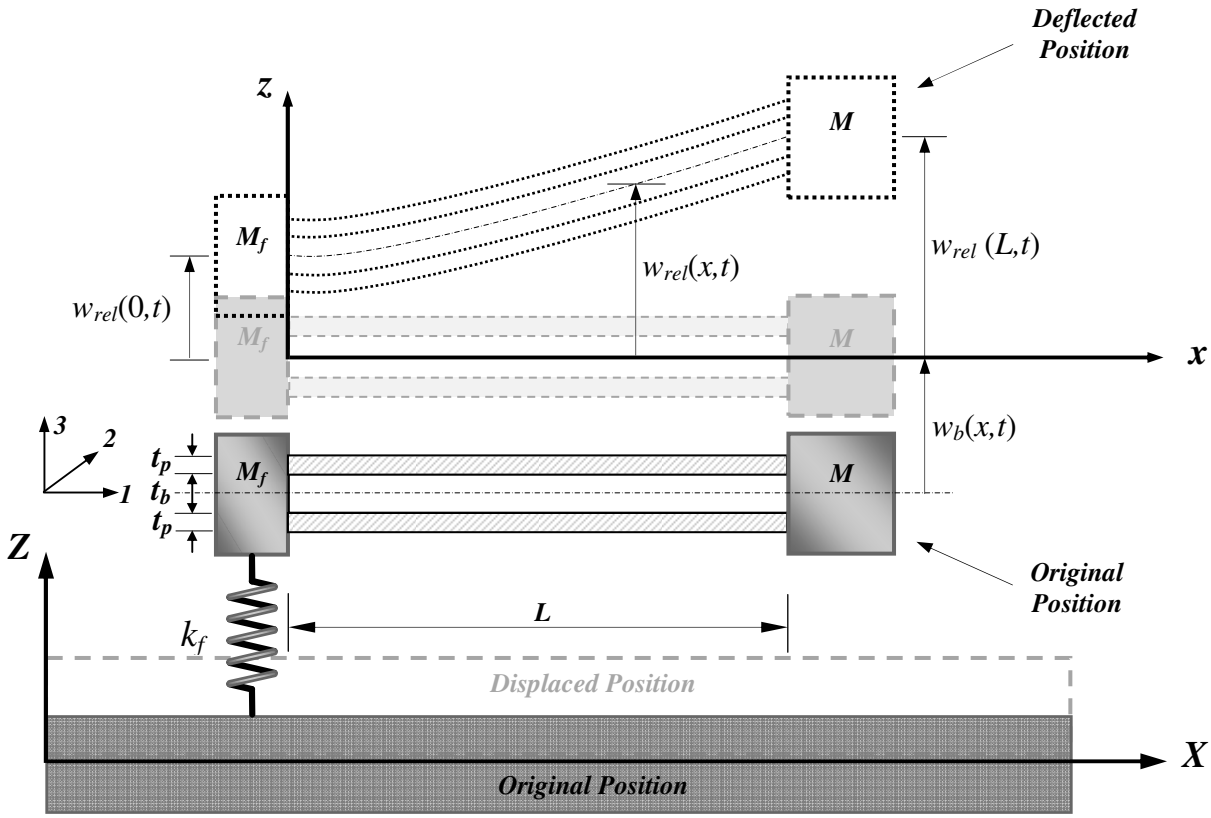

Figure 2.3: Original and deflected positions of the cantilevered piezoelectric energy harvester with dynamic magnifier

2.3.1. Kinetic Energy (T)

The kinetic energy of the *CPEHDM* system is given by

$$T = \frac{1}{2}\int_0^L m_t \left(\frac{\partial w}{\partial t}\right)^2 dx + \frac{1}{2}M_f\left(\frac{\partial w(0,t)}{\partial t}\right)^2 + \frac{1}{2}M\left(\frac{\partial w(L,t)}{\partial t}\right)^2 \tag{2.2}$$

where $m_t = m_b + 2m_p$ with m_b and m_p denoting the mass per unit length of the beam and a single piezoelectric patch, respectively.

On substituting Equation (2.1) into Equation (2.2), gives

$$T = \frac{1}{2}\int_0^L m_t \left(\frac{\partial w_{rel}}{\partial t} + \frac{\partial w_b}{\partial t} \right)^2 dx + \frac{1}{2} M_f \left(\frac{\partial w_{rel}(0,t)}{\partial t} + \frac{\partial w_b(0,t)}{\partial t} \right)^2 + \frac{1}{2} M \left(\frac{\partial w_{rel}(L,t)}{\partial t} + \frac{\partial w_b(L,t)}{\partial t} \right)^2 \tag{2.3}$$

2.3.2. Potential Energy (U)

The potential energy of the *CPEHDM* system is given by

$$U = \frac{1}{2}\int_0^L E_b I_b \left(\frac{\partial^2 w_{rel}}{\partial x^2} \right)^2 dx + \frac{1}{2}\int_{\Omega_p} T_1 S_1 d\Omega_P + \frac{1}{2} k_f w_{rel}^2(0,t) \tag{2.4}$$

where $E_b I_b$ is the flexural rigidity of the beam, T_1 is the stress in the piezoelectric layers, S_1 is the strain in the piezoelectric layers, and Ω_P is the volume of the piezoelectric layers.

After using the constitutive equations of piezoelectric materials (ANSI/IEEE STD 176-1987), we have

$$T_1 = c_{11}^E \left(S_1 - d_{31} E_3 \right) \tag{2.5}$$

where c_{11}^E is the Young's modulus at constant electric field, d_{31} is the piezoelectric strain coefficient, $S_1 = -z\left(\partial^2 w_{rel} / \partial x^2\right)$, and $E_3 = -V_T / 2t_p$ is the electric field for series connection of piezoelectric layers where V_T denotes the respective electric voltage across the resistive electric load R_L.

On substituting Equation (2.5) into Equation (2.4), it reduces to

$$U = \frac{1}{2}\int_0^L E_b I_b \left(\frac{\partial^2 w_{rel}}{\partial x^2} \right)^2 dx + \frac{1}{2}\int_{\Omega_p} c_{11}^E \left(S_1 - d_{31} E_3 \right) S_1 d\Omega_P + \frac{1}{2} k_f w_{rel}^2(0,t) \tag{2.6}$$

Equation (2.6) can be further expanded to

$$
\begin{aligned}
U &= \frac{1}{2}\int_0^L E_b I_b \left(\frac{\partial^2 w_{rel}}{\partial x^2}\right)^2 dx \\
&+ \frac{1}{2}\left[2c_{11}^E b \int_0^L \left\{ \int_h^{h+t_p} \left(-z\left(\frac{\partial^2 w_{rel}}{\partial x^2}\right) + d_{31}\frac{V_T}{2t_p}\right)\left(-z\left(\frac{\partial^2 w_{rel}}{\partial x^2}\right)\right) dz \right\} dx\right] \\
&+ \frac{1}{2} k_f w_{rel}^2 (0,t)
\end{aligned}
\tag{2.7}
$$

where $h = t_b / 2$.

Performing the integrations, Equation (2.7) reduces to

$$
U = \frac{1}{2}\int_0^L \left[E_t I_t \left(\frac{\partial^2 w_{rel}}{\partial x^2}\right)^2 - bc_{11}^E d_{31} V_T \left(h + t_p / 2\right)\left(\frac{\partial^2 w_{rel}}{\partial x^2}\right)\right] dx + \frac{1}{2} k_f w_{rel}^2 (0,t) \tag{2.8}
$$

where $E_t I_t = E_b I_b + \frac{2}{3} c_{11}^E b \left(3h^2 t_p + 3ht_p^2 + t_p^3\right)$.

As the electric voltage is related to the electric charge by

$$
V_T = R_L \frac{dQ}{dt} \tag{2.9}
$$

On substituting Equation (2.9) into Equation (2.8), it reduces to

$$
\begin{aligned}
U &= \frac{1}{2}\int_0^L \left[E_t I_t \left(\frac{\partial^2 w_{rel}}{\partial x^2}\right)^2 - bc_{11}^E d_{31} R_L \left(\frac{dQ}{dt}\right)\left(h + t_p / 2\right)\left(\frac{\partial^2 w_{rel}}{\partial x^2}\right)\right] dx \\
&+ \frac{1}{2} k_f w_{rel}^2 (0,t)
\end{aligned}
\tag{2.10}
$$

2.3.3. Electric Energy (W_e)

The electric energy of the *CPEH*DM system is given by

$$
W_e = \frac{1}{2}\int_{\Omega_p} E_3 D_3 d\Omega_P \tag{2.11}
$$

where D_3 is the electric displacement.

Now, from the constitutive equations of piezoelectric materials (ANSI/IEEE STD 176-1987), we have

$$D_3 = d_{31}T_1 + \in_{33}^{T} E_3 \tag{2.12}$$

where $\in_{33}^{T}$ is the permittivity at constant stress.

On substituting Equations (2.5) and (2.12) into Equation (2.11), the result is

$$\begin{aligned} W_e = \frac{1}{2}\Bigg[2b\int_0^L \Bigg\{ \int_h^{h+t_p} \Bigg(d_{31}c_{11}^E \left(-z\left(\frac{\partial^2 w_{rel}}{\partial x^2}\right)\right)\left(\frac{-V_T}{2t_p}\right) \\ -d_{31}^2 c_{11}^E \left(\frac{V_T}{2t_p}\right)^2 + \in_{33}^{T}\left(\frac{V_T}{2t_p}\right)^2 \Bigg) dz \Bigg\} dx \Bigg] \end{aligned} \tag{2.13}$$

Evaluating the integrals in Equation (2.13) and utilizing Equation (2.9), we get

$$\begin{aligned} W_e = \frac{1}{2}\int_0^L \left(bc_{11}^E d_{31} R_L \left(\frac{dQ}{dt}\right)\left(h + t_p/2\right)\left(\frac{\partial^2 w_{rel}}{\partial x^2}\right)\right) dx \\ -bLd_{31}^2 c_{11}^E \left(R_L^2/4t_p\right)\left(\frac{dQ}{dt}\right)^2 + bL\in_{33}^{T}\left(R_L^2/4t_p\right)\left(\frac{dQ}{dt}\right)^2 \end{aligned} \tag{2.14}$$

The permittivity component at constant strain is related to the permittivity at constant stress by

$$\in_{33}^{S} = \in_{33}^{T} - d_{d31}^2 c_{11}^E \tag{2.15}$$

On substituting Equation (2.15) into Equation (2.14), we get

$$W_e = \frac{1}{2}\int_0^L \left(bc_{11}^E d_{31} R_L \left(\frac{dQ}{dt}\right)\left(h + t_p/2\right)\left(\frac{\partial^2 w_{rel}}{\partial x^2}\right)\right) dx + bL\in_{33}^{S}\left(R_L^2/4t_p\right)\left(\frac{dQ}{dt}\right)^2 \tag{2.16}$$

2.3.4. *Undamped Equations of Motion*

The generalized Hamilton's principle will be used to derive the undamped electromechanical equations of motion associated with the mechanical and electrical degrees of freedom $w_{rel}(x,t)$ and $Q(t)$ as

$$\begin{aligned}
&\int_{t_1}^{t_2} \left(\delta T - \delta U + \delta W_e + \delta W \right) dt = 0, \\
&\delta w_{rel}(x,t) = 0, \quad \delta Q(t) = 0, \\
&0 \le x \le L, \quad t = t_1, t_2
\end{aligned} \tag{2.17}$$

where δW is the variation of the electrically extracted work. It is given by

$$\delta W = -R_L \frac{dQ}{dt} \delta Q \tag{2.18}$$

The variations of the kinetic energy, the potential energy, and the electric energy are given by

$$\begin{aligned}
\delta T = &\int_0^L m_t \left(\frac{\partial w_{rel}}{\partial t} + \frac{\partial w_b}{\partial t} \right) \delta \left(\frac{\partial w_{rel}}{\partial t} \right) dx \\
&+ M_f \left(\frac{\partial w_{rel}(0,t)}{\partial t} + \frac{\partial w_b(0,t)}{\partial t} \right) \delta \left(\frac{\partial w_{rel}(0,t)}{\partial t} \right) \\
&+ M \left(\frac{\partial w_{rel}(L,t)}{\partial t} + \frac{\partial w_b(L,t)}{\partial t} \right) \delta \left(\frac{\partial w_{rel}(L,t)}{\partial t} \right)
\end{aligned} \tag{2.19}$$

$$\begin{aligned}
\delta U = &\int_0^L \left[E_t I_t \left(\frac{\partial^2 w_{rel}}{\partial x^2} \right) \delta \left(\frac{\partial^2 w_{rel}}{\partial x^2} \right) - \frac{1}{2} b c_{11}^E d_{31} \left(h + t_p / 2 \right) R_L \delta \left(\frac{dQ}{dt} \right) w_{rel,xx} \right. \\
&\left. - \frac{1}{2} b c_{11}^E d_{31} \left(h + t_p / 2 \right) R_L \left(\frac{dQ}{dt} \right) \left[H(x) - H(x-L) \right] \delta w_{rel,xx} \right] dx \\
&+ k_f w_{rel}(0,t) \delta w_{rel}(0,t)
\end{aligned} \tag{2.20}$$

$$\delta W_e = \int_0^L \left[\frac{1}{2} b c_{11}^E d_{31} \left(h + t_p / 2 \right) R_L \delta \left(\frac{dQ}{dt} \right) w_{rel,xx} \right.$$
$$\left. + \frac{1}{2} b c_{11}^E d_{31} \left(h + t_p / 2 \right) R_L \left(\frac{dQ}{dt} \right) \left[H(x) - H(x-L) \right] \delta w_{rel,xx} \right] dx \tag{2.21}$$
$$+ 2bL \in_{33}^S \left(R_L^2 / 4t_p \right) \left(\frac{dQ}{dt} \right) \delta \left(\frac{dQ}{dt} \right)$$

where $H(x)$ is the Heaviside function.

The different integrations in Equation (2.17) are evaluated separately as follows

$$\int_{t_1}^{t_2} \delta T dt = -\int_{t_1}^{t_2} \left[\int_0^L m_t \left(\frac{\partial^2 w_{rel}}{\partial t^2} + \frac{\partial^2 w_b}{\partial t^2} \right) \delta w_{rel} dx + M_f \left(\frac{\partial^2 w_{rel}(0,t)}{\partial t^2} \right) \delta w_{rel}(0,t) \right.$$
$$+ M_f \left(\frac{\partial^2 w_b}{\partial t^2} \right) \delta(x) \delta w_{rel} + M \left(\frac{\partial^2 w_{rel}(L,t)}{\partial t^2} \right) \delta w_{rel}(L,t) \tag{2.22}$$
$$\left. + M \left(\frac{\partial^2 w_b}{\partial t^2} \right) \delta(x-L) \delta w_{rel} \right] dt$$

$$\int_{t_1}^{t_2} \delta U dt = \int_{t_1}^{t_2} \left[E_t I_t \left(\frac{\partial^2 w_{rel}}{\partial x^2} \right) \delta \left(\frac{\partial w_{rel}}{\partial x} \right) \Bigg|_{x=0}^{x=L} - E_t I_t \left(\frac{\partial^3 w_{rel}}{\partial x^3} \right) \delta w_{rel} \Bigg|_{x=0}^{x=L} \right.$$
$$+ \int_0^L E_t I_t \left(\frac{\partial^4 w_{rel}}{\partial x^4} \right) \delta w_{rel} dx + \frac{1}{2} \int_0^L b c_{11}^E d_{31} \left(h + t_p / 2 \right) R_L \left(\frac{\partial^3 w_{rel}}{\partial x^2 \partial t} \right) \delta Q dx \tag{2.23}$$
$$- \frac{1}{2} \int_0^L b c_{11}^E d_{31} \left(h + t_p / 2 \right) R_L \left(\frac{dQ}{dt} \right) \left[\frac{d\delta(x)}{dx} - \frac{d\delta(x-L)}{dx} \right] \delta w_{rel} dx$$
$$\left. + k_f w_{rel}(0,t) \delta w_{rel}(0,t) \right] dt$$

$$\int_{t_1}^{t_2} \delta W_e dt = \int_{t_1}^{t_2} \left[-\frac{1}{2} \int_0^L b c_{11}^E d_{31} R_L \left(h + t_p / 2 \right) \left(\frac{\partial^3 w_{rel}}{\partial x^2 \partial t} \right) \delta Q dx \right.$$
$$+ \frac{1}{2} \int_0^L b c_{11}^E d_{31} \left(h + t_p / 2 \right) R_L \left(\frac{dQ}{dt} \right) \left[\frac{d\delta(x)}{dx} - \frac{d\delta(x-L)}{dx} \right] \delta w_{rel} dx \tag{2.24}$$
$$\left. - 2bL \in_{33}^S \left(R_L^2 / 4t_p \right) \left(\frac{d^2 Q}{dt^2} \right) \delta Q \right] dt$$

where $\delta(x)$ is the Dirac delta function. It satisfies the following relation

$$\int_{-\infty}^{\infty} \frac{d^n \delta(x-x_0)}{dx^n} f(x)\,dx = (-1)^n \frac{df^n(x_0)}{dx^n} \tag{2.25}$$

Substituting Equation (2.18) and Equations (2.22)-(2.24) into Equation (2.17) and collecting terms, we get

$$\begin{aligned}
&\int_{t_1}^{t_2}\Bigg\{\int_0^L\Bigg[-m_t\left(\frac{\partial^2 w_{rel}}{\partial t^2}\right)-m_t\left(\frac{\partial^2 w_b}{\partial t^2}\right)-M_f\left(\frac{\partial^2 w_b}{\partial t^2}\right)\delta(x)-M\left(\frac{\partial^2 w_b}{\partial t^2}\right)\delta(x-L)\\
&-E_tI_t\left(\frac{\partial^4 w_{rel}}{\partial x^4}\right)+\Gamma\frac{dQ}{dt}\left[\frac{d\delta(x)}{dx}-\frac{d\delta(x-L)}{dx}\right]\Bigg]\delta w_{rel}dx\\
&-\left[E_tI_t\left(\frac{\partial^2 w_{rel}}{\partial x^2}\right)\right]\delta\left(\frac{\partial w_{rel}}{\partial x}\right)\Bigg|_{x=L}+\left[E_tI_t\left(\frac{\partial^2 w_{rel}}{\partial x^2}\right)\right]\delta\left(\frac{\partial w_{rel}}{\partial x}\right)\Bigg|_{x=0}\\
&+\left[-M\left(\frac{\partial^2 w_{rel}}{\partial t^2}\right)+E_tI_t\left(\frac{\partial^3 w_{rel}}{\partial x^3}\right)\right]\delta w_{rel}\Bigg|_{x=L}\\
&+\left[-M_f\left(\frac{\partial^2 w_{rel}}{\partial t^2}\right)-E_tI_t\left(\frac{\partial^3 w_{rel}}{\partial x^3}\right)-k_f w_{rel}\right]\delta w_{rel}\Bigg|_{x=0}\\
&+\Bigg[-\int_0^L bc_{11}^E d_{31}\left(h+t_p/2\right)R_L\left(\frac{\partial^3 w_{rel}}{\partial x^2\partial t}\right)dx\\
&-2bL\in_{33}^S\left(R_L^2/4t_p\right)\left(\frac{d^2Q}{dt^2}\right)-R_L\left(\frac{dQ}{dt}\right)\Bigg]\delta Q\Bigg\}dt=0
\end{aligned} \tag{2.26}$$

The resulting distributed parameter undamped electromechanical equations of the *CPEHDM* system are obtained by invoking the arbitrariness of the virtual displacement δw_{rel} and the virtual electric charge δQ as

$$\begin{aligned}
&m_t\left(\frac{\partial^2 w_{rel}}{\partial t^2}\right)+E_tI_t\left(\frac{\partial^4 w_{rel}}{\partial x^4}\right)-\Gamma\left(\frac{dQ}{dt}\right)\left[\frac{d\delta(x)}{dx}-\frac{d\delta(x-L)}{dx}\right]\\
&=-\left[m_t+M_f\delta(x)+M\delta(x-L)\right]\left(\frac{\partial^2 w_b}{\partial t^2}\right)
\end{aligned} \tag{2.27}$$

$$\int_0^L \Gamma\left(\frac{\partial^3 w_{rel}}{\partial x^2 \partial t}\right)dx + \frac{C_P}{2} R_L^2 \left(\frac{d^2 Q}{dt^2}\right) = -R_L\left(\frac{dQ}{dt}\right) \tag{2.28}$$

where $\Gamma = bc_{11}^E d_{31}\left(h + t_p/2\right)R_L$ and $C_P = bL\in_{33}^S / t_p$ is the internal capacitance of a single piezoelectric layer.

The corresponding boundary conditions for the relative motion of the undamped composite piezoelectric beam are

$$\begin{aligned} &\left.\frac{\partial w_{rel}}{\partial x}\right|_{x=0} = 0, \quad \left.\left[M_f\left(\frac{\partial^2 w_{rel}}{\partial t^2}\right) + E_t I_t\left(\frac{\partial^3 w_{rel}}{\partial x^3}\right) + k_f w_{rel}\right]\right|_{x=0} = 0, \\ &\left.E_t I_t\left(\frac{\partial^2 w_{rel}}{\partial x^2}\right)\right|_{x=L} = 0, \quad \left.\left[-M\left(\frac{\partial^2 w_{rel}}{\partial t^2}\right) + E_t I_t\left(\frac{\partial^3 w_{rel}}{\partial x^3}\right)\right]\right|_{x=L} = 0 \end{aligned} \tag{2.29}$$

Now, the relative vibration response of the undamped composite piezoelectric beam can be assumed in the following series form of eigenfunctions

$$w_{rel}\left(x,t\right) = \sum_{r=1}^{\infty} W_r\left(x\right)\eta_r\left(t\right) \tag{2.30}$$

where $W_r\left(x\right)$ is the mass normalized eigenfunction of the rth mode of vibration and $\eta_r\left(t\right)$ is the corresponding modal mechanical response.

The eigenfunctions $W_r\left(x\right)$ can be obtained using Equations (2.27) and (2.29) as

$$\begin{aligned} W_r\left(x\right) = A_r \{&\cosh\left(\beta_r L\right)\left[\sin\left(\beta_r x\right) - \sinh\left(\beta_r x\right)\right] \\ &+\left[\sin\left(\beta_r L\right) + \sinh\left(\beta_r L\right)\right]\cosh\left(\beta_r x\right) \\ &+\Lambda_r\left[\cosh\left(\beta_r L\right)\cos\left(\beta_r x\right) + \cos\left(\beta_r L\right)\cosh\left(\beta_r x\right)\right]\} \end{aligned} \tag{2.31}$$

where A_r is a modal amplitude constant and Λ_r is given by

$$\Lambda_r = \frac{\begin{array}{l} 1-\sin(\beta_r L)\sinh(\beta_r L)+\cos(\beta_r L)\cosh(\beta_r L) \\ -2(\beta_r L)\left(\dfrac{M}{m_t L}\right)\sin(\beta_r L)\cosh(\beta_r L) \end{array}}{\begin{array}{l} \sin(\beta_r L)\cosh(\beta_r L)+\cos(\beta_r L)\sinh(\beta_r L) \\ +2(\beta_r L)\left(\dfrac{M}{m_t L}\right)\cos(\beta_r L)\cosh(\beta_r L) \end{array}} \tag{2.32}$$

The modal amplitude constant A_r should be determined so as to satisfy the following orthogonality relations for the *CPEHDM* system

$$\begin{array}{l} \int_0^L W_s(x)\, m_t W_r(x) dx + W_s(L) M W_r(L) + W_s(0) M_f W_r(0) = \delta_{rs}, \\ \int_0^L W_s(x) E_t I_t \dfrac{d^4 W_r(x)}{dx^4} dx - \left[W_s(x) E_t I_t \dfrac{d^3 W_r(x)}{dx^3} \right]\Bigg|_{x=L} \\ + \left[W_s(x) E_t I_t \dfrac{d^3 W_r(x)}{dx^3} \right]\Bigg|_{x=0} + k_f W_s(0) W_r(0) = \omega_r^2 \delta_{rs} \end{array} \tag{2.33}$$

The rth natural frequency of the *CPEHDM* system is obtained under short-circuit conditions as

$$\omega_r = (\beta_r L)^2 \sqrt{\frac{E_t I_t}{m_t L^4}} \tag{2.34}$$

where $\beta_r L$ is the corresponding r^{th} eigenvalue which can be obtained from the following characteristic equation of the *CPEHDM* system

$$\begin{array}{l} \left[\dfrac{k_f L^3}{E_t I_t} - (\beta_r L)^4 \left(\dfrac{M_f}{m_t L} \right) \right] \{ \sin(\beta_r L) + \sinh(\beta_r L) \\ + \Lambda_r \left[\cos(\beta_r L) + \cosh(\beta_r L) \right] \} - 2(\beta_r L)^3 \cosh(\beta_r L) = 0 \end{array} \tag{2.35}$$

2.3.5. *Damped Equations of Motion*

Two types of mechanical damping are used in the analysis of the *CPEHDM* system. The first is referred to as the viscous air damping whereas the second is known as the strain rate damping due to structural viscoelasticity. In fact, the viscous air damping acts on the absolute velocity whereas the strain rate damping acts on the relative velocity of the composite piezoelectric beam [10].

Accordingly, Equation (2.27) can be written for the damped composite piezoelectric beam as

$$\begin{aligned} & m_t\left(\frac{\partial^2 w_{rel}}{\partial t^2}\right)+E_tI_t\left(\frac{\partial^4 w_{rel}}{\partial x^4}\right)+c_a\left(\frac{\partial w_{rel}}{\partial t}\right)+c_sI_t\left(\frac{\partial^5 w_{rel}}{\partial x^4\partial t}\right) \\ & -\Gamma\left(\frac{dQ}{dt}\right)\left[\frac{d\delta(x)}{dx}-\frac{d\delta(x-L)}{dx}\right] \\ & =-\left[m_t+M_f\delta(x)+M\delta(x-L)\right]\left(\frac{\partial^2 w_b}{\partial t^2}\right)-c_a\left(\frac{\partial w_b}{\partial t}\right) \end{aligned} \tag{2.36}$$

where c_a is the viscous air damping coefficient and c_sI_t is the equivalent damping term of the beam cross-section due to structural viscoelasticity.

The mechanical damping ratio ζ_r of the rth mode of vibration which includes the effect of both viscous air damping and strain rate damping is given by [10,11]

$$\zeta_r=\zeta_r^a+\zeta_r^s=\frac{c_a}{2m_t\hat{\omega}_r}+\frac{c_sI_t\hat{\omega}_r}{2E_tI_t} \tag{2.37}$$

where ζ_r^a is the viscous air damping component of the damping ratio, ζ_r^s is the strain rate damping component of the damping ratio, and $\hat{\omega}_r$ is the rth natural frequency of the composite piezoelectric beam in the absence of the dynamic magnifier and the end mass M .

Equation (2.37) indicates that the viscous air damping is assumed to be proportional to the mass per unit length whereas strain rate damping is assumed to be proportional to the flexural stiffness of the beam. This idealized modeling assumption allows the use of a standard modal analysis approach.

Experimental modal analysis under short circuit conditions is required to determine any two modal damping ratios so as to calculate the constants c_a and $c_s I_t$ using Equation (2.37). Once these proportionality constants are known, Equation (2.37) can be used again to find the rest of the modal damping ratios.

Substituting Equation (2.30) into Equations (2.28) and (2.36), and utilizing Equation (2.33), we get

$$\frac{d^2\eta_r(t)}{dt^2} + 2\zeta_r\omega_r\frac{d\eta_r(t)}{dt} + \omega_r^2\eta_r(t) - \Psi_r\frac{dQ(t)}{dt} = f_r(t) \tag{2.38}$$

$$\sum_{r=1}^{\infty}\Psi_r\frac{d\eta_r(t)}{dt} + \frac{C_P}{2}R_L^2\frac{d^2Q(t)}{dt^2} + R_L\frac{dQ(t)}{dt} = 0 \tag{2.39}$$

where Ψ_r is denoted as the rth mode electromechanical coupling term. It is given by

$$\Psi_r = \Gamma\left.\frac{dW_r(x)}{dx}\right|_{x=L} \tag{2.40}$$

and the modal mechanical forcing function $f_r(t)$ for a harmonic translating base can be written as follows

$$\begin{aligned} f_r(t) = &-\frac{d^2w_b(x,t)}{dt^2}\left[m_t\int_0^L W_r(x)\,dx + M_f W_r(L) + MW_r(L)\right] \\ &-c_a\frac{dw_b(t)}{dt}\int_0^L W_r(x)dx \end{aligned} \tag{2.41}$$

For harmonic base excitations at a frequency ω such that

$$w_b\left(x,t\right)=W_b e^{j\omega t} \tag{2.42}$$

Then, the corresponding solutions can be assumed to be

$$\eta_r\left(t\right)=\Pi_r e^{j\omega t},\quad Q=Q_0 e^{j\omega t} \tag{2.43}$$

Substituting Equations (2.42) and (2.43) into Equations (2.38) and (2.39), gives

$$\left(\omega_r^2-\omega^2+j2\zeta_r\omega_r\omega\right)\Pi_r-j\omega\Psi_r Q_0=F_r \tag{2.44}$$

$$j\omega\sum_{r=1}^{\infty}\Psi_r\Pi_r+\left(j\omega R_L-\omega^2\frac{C_P}{2}R_L^2\right)Q_0=0 \tag{2.45}$$

where F_r denotes the amplitude of the modal mechanical forcing function. It is given by

$$F_r=\omega^2 W_b\left[m_t\int_0^L W_r\left(x\right)dx+M_f W_r\left(0\right)+MW_r\left(L\right)\right]-j\omega W_b c_a\int_0^L W_r\left(x\right)dx \tag{2.46}$$

Equations (2.44) and (2.45) can be solved for the steady-state electric charge and the modal mechanical response as follows

$$Q\left(t\right)=\frac{\displaystyle\sum_{r=1}^{\infty}\frac{j\Psi_r F_r}{\omega_r^2-\omega^2+j2\zeta_r\omega_r\omega}}{\omega\dfrac{C_P}{2}R_L^2-jR_L+\displaystyle\sum_{r=1}^{\infty}\frac{\omega\Psi_r^2}{\omega_r^2-\omega^2+j2\zeta_r\omega_r\omega}}e^{j\omega t} \tag{2.47}$$

$$\eta_r\left(t\right)=\frac{F_r+j\omega\Psi_r Q_0}{\omega_r^2-\omega^2+j2\zeta_r\omega_r\omega}e^{j\omega t} \tag{2.48}$$

The steady-state relative vibration response of the composite piezoelectric beam can be found from Equation (2.30) as

$$w_{rel}\left(x,t\right)=\sum_{r=1}^{\infty}\left[\frac{F_r+j\omega\Psi_r Q_0}{\omega_r^2-\omega^2+j2\zeta_r\omega_r\omega}W_r\left(x\right)\right]e^{j\omega t} \tag{2.49}$$

Equations (2.47) and (2.49) will be used to predict the performance of the *CPEHDM* system as function of its design and load parameters.

2.4. Finite Element Modeling of Energy Harvester with a Dynamic Magnifier

In this section, a finite element model is developed to simulate the vibrations of the *CPEHDM* during its transverse oscillation around the original position as outlined in Figure 2.4. Three coordinate systems are considered here to clearly explain the kinematics of the *CPEHDM*. These systems are the inertial frame of reference $X-Z$ (fixed in space), the base-fixed coordinate system $x-z$ (moving with the base), and the element local coordinate system $x'-z'$ (moving with the base) which is needed to carry out the required integrations as we will see later.

Let w_b denote the displacement of the base relative to the inertial frame of reference $X-Z$ and $w_{e_{x'}}$ denote the transverse deflection of the eth beam element relative to the base-fixed coordinate system $x-z$ at any location x'. Accordingly, one can write

$$w_0=w_{e_0}+w_b,\quad w_e=w_{e_{x'}}+w_b,\quad w_L=w_{e_L}+w_b \tag{2.50}$$

where w_e is the transverse deflection of the eth beam element relative to the inertial frame of reference $X-Z$ at the same location x' where $w_{e_{x'}}$ was defined. In addition, w_{e_0} and w_{e_L} denote, respectively, the transverse deflection of the magnifier mass M_f and the end mass M relative to the moving coordinate system $x-z$. If the beam is divided into N finite elements, then w_{e_L} is denoted as w_{e_N}.

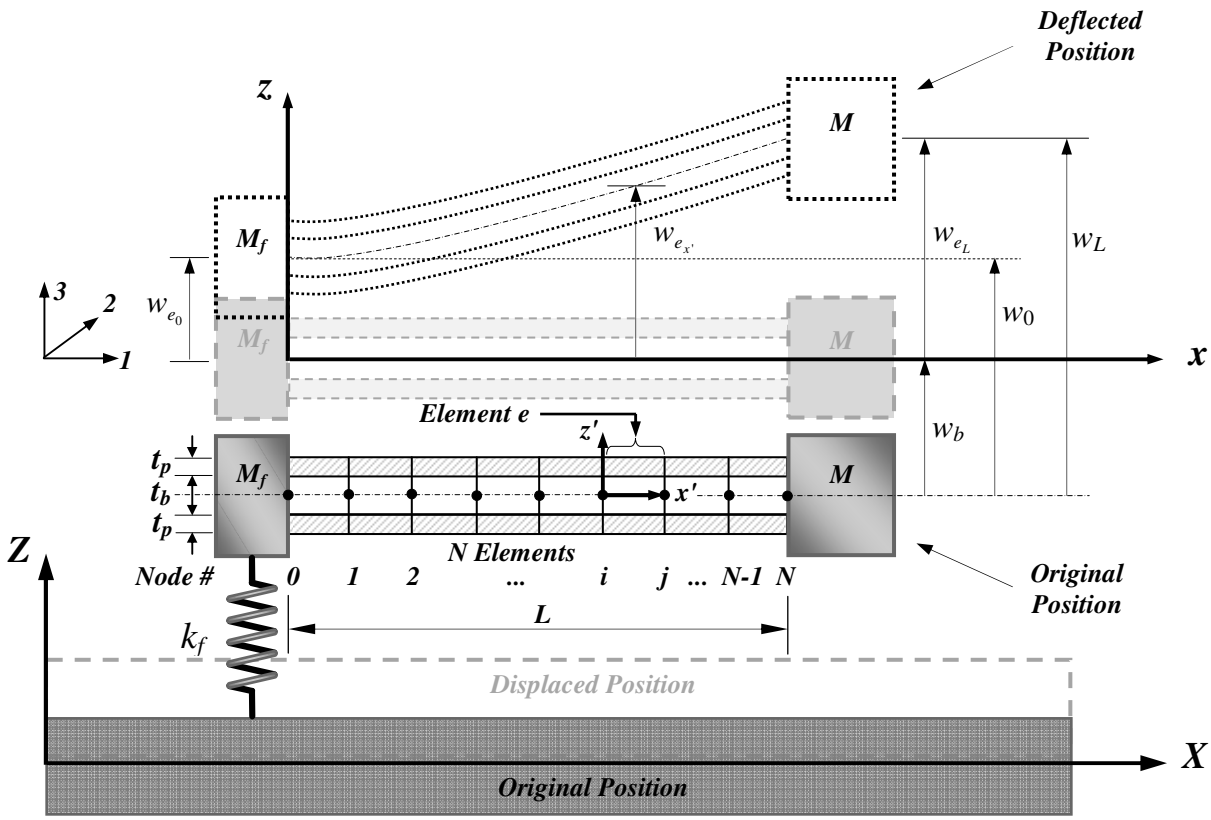

Figure 2.4: *CPEHDM* with series connection of piezoelectric patches

2.4.1. *Kinetic Energy* (T)

The different components of the kinetic energy of the *CPEHDM* system are given by

$$T_e = \frac{1}{2}\int_0^{L_e} m_t \dot{w}_e^2 dx', \quad T_0 = \frac{1}{2} M_f \dot{w}_0^2, \quad T_L = \frac{1}{2} M \dot{w}_L^2 \tag{2.51}$$

where T_e is the kinetic energy of the eth element of the beam, T_0 is the kinetic energy of the magnifier mass M_f, and T_L is the kinetic energy of the end mass M. Also, $m_t = m_b + 2m_p$ with m_b and m_p denoting the mass per unit length of the beam and a single piezoelectric patch, respectively.

Hence, the total kinetic energy of the *CPEHDM* system is given by

$$T = \sum_{e=1}^{N} T_e + T_0 + T_L \tag{2.52}$$

For the beam element, consider the following finite element interpolation relationship

$$w_{e_{x'}} = \mathbf{N}\mathbf{U}_e \tag{2.53}$$

where $\mathbf{N}$ is an appropriate interpolating vector and $\mathbf{U}_e$ is the element nodal deflection vector relative to the base-fixed coordinate system $x - z$. It is given by

$$\mathbf{U}_e = \left\{ w_{e_i} \quad w_{e_i,x'} \quad w_{e_j} \quad w_{e_j,x'} \right\}^T \tag{2.54}$$

where w_{e_i} and $w_{e_i,x'}$ are the transverse deflection and slope at node i whereas w_{e_j} and $w_{e_j,x'}$ are the transverse deflection and slope of the beam element e at node j, respectively.

Hence, from Equations (2.50) and (2.53), the transverse deflection w_e of the eth beam element relative to the inertial frame of reference $X - Z$ can be written as

$$w_e = w_{e_{x'}} + w_b = \mathbf{N}\left(\mathbf{U}_e + \mathbf{U}_b\right) \tag{2.55}$$

where $\mathbf{U}_b = \mathbf{\Delta}_b e^{j\omega t}$ is the element nodal displacement vector for a harmonic base motion with $\mathbf{\Delta}_b = \left\{ w_b \quad 0 \quad w_b \quad 0 \right\}^T$ in the case of a translating base. The convenient form of Equation (2.55) is made possible because of the special structure of the interpolating vector $\mathbf{N}$.

Substituting Equations (2.50) and (2.51) into Equation (2.52), the total kinetic energy of the *CPEHDM* system reduces to

$$T = \sum_{e=1}^{N} \left(\frac{1}{2} \int_0^{L_e} m_t \left(\dot{w}_{e_{x'}} + \dot{w}_b \right)^2 dx' \right) + \frac{1}{2} M_f \left(\dot{w}_{e_0} + \dot{w}_b \right)^2 + \frac{1}{2} M \left(\dot{w}_{e_L} + \dot{w}_b \right)^2 \tag{2.56}$$

Substituting Equation (2.55) into Equation (2.56), it reduces to

$$
\begin{aligned}
T = & \frac{1}{2}\sum_{e=1}^{N}\left[\left(\dot{\mathbf{U}}_e + \dot{\mathbf{U}}_b\right)^T \mathbf{M}_e \left(\dot{\mathbf{U}}_e + \dot{\mathbf{U}}_b\right)\right] \\
& + \frac{1}{2}\left(\dot{\mathbf{U}}_e + \dot{\mathbf{U}}_b\right)^T \mathbf{M}_F \left(\dot{\mathbf{U}}_e + \dot{\mathbf{U}}_b\right) \\
& + \frac{1}{2}\left(\dot{\mathbf{U}}_e + \dot{\mathbf{U}}_b\right)^T \mathbf{M}_L \left(\dot{\mathbf{U}}_e + \dot{\mathbf{U}}_b\right)
\end{aligned}
\tag{2.57}
$$

where $\mathbf{M}_e = \int_0^{L_e} m_t \mathbf{N}^T \mathbf{N} dx'$, $\mathbf{M}_F = \mathbf{a}_1^T M_f \mathbf{a}_1$ with $\mathbf{a}_1 = \left\{1 \quad \mathbf{0}_{1\times(2N+1)}\right\}$, and $\mathbf{M}_L = \mathbf{a}_2^T M \mathbf{a}_2$ with $\mathbf{a}_2 = \left\{\mathbf{0}_{1\times 2N} \quad 1 \quad 0\right\}$.

After assembly of all the beam elements, Equation (2.57) reduces to

$$
T = \frac{1}{2}\left(\dot{\mathbf{U}} + \dot{\mathbf{U}}_{base}\right)^T \left[\mathbf{M}_b + \mathbf{M}_F + \mathbf{M}_L\right]\left(\dot{\mathbf{U}} + \dot{\mathbf{U}}_{base}\right) \tag{2.58}
$$

where $\mathbf{M}_b$ is the global mass matrix of the composite piezoelectric beam, $\mathbf{U}_{base}$ is the global nodal displacement vector of the base, and $\mathbf{U}$ is the global nodal deflection vector of the *CPEH*DM system given by

$$
\mathbf{U} = \left\{w_{e_0} \quad w_{e_0,x'} \quad w_{e_1} \quad w_{e_1,x'} \quad \ldots \quad w_{e_N} \quad w_{e_N,x'}\right\}^T \tag{2.59}
$$

2.4.2. Potential Energy (U)

The different components of the potential energy of the *CPEHDM* system are given by

$$
U_e = \frac{1}{2}\int_0^{L_e} E_b I_b w_{e_{x'},x'x'}^2 dx' + \frac{1}{2}\int_{\Omega_P} T_1 S_1 d\Omega_P, \quad U_0 = \frac{1}{2} k_f w_{e_0}^2 \tag{2.60}
$$

where U_e is the potential energy of the eth element of the beam, U_0 is the potential energy of the magnifier spring k_f, $E_b I_b$ is the flexural rigidity of the beam, T_1 is the

stress in the piezoelectric layers, S_1 is the strain in the piezoelectric layers, and Ω_P is the volume of the piezoelectric layers of element e.

Hence, the total potential energy of the *CPEHDM* system is given by

$$U = \sum_{e=1}^{N} U_e + U_0 \tag{2.61}$$

Using the constitutive equations of piezoelectric materials (ANSI/IEEE STD 176-1987), we have

$$T_1 = c_{11}^E \left(S_1 - d_{31} E_3 \right) \tag{2.62}$$

where c_{11}^E is the Young's modulus at constant electric field, d_{31} is the piezoelectric strain coefficient, $S_1 = -z' w_{e_{x'},x'x'}$, and $E_3 = -V_T / 2t_p$ is the electric field for series connection of piezoelectric layers where V_T denotes the respective electric voltage across the resistive electric load R_L.

Substituting Equations (2.60) and (2.62) into Equation (2.61), it reduces to

$$U = \sum_{e=1}^{N} \left(\frac{1}{2} \int_0^{L_e} E_b I_b w_{e_{x'},x'x'}^2 dx' + \frac{1}{2} \int_{\Omega_p} c_{11}^E \left(S_1 - d_{31} E_3 \right) S_1 d\Omega_P \right) + \frac{1}{2} k_f w_{e_0}^2 \tag{2.63}$$

Equation (2.63) can be further expanded to

$$\begin{aligned} U = \sum_{e=1}^{N} \Bigg(& \frac{1}{2} \int_0^{L_e} E_b I_b w_{e_{x'},x'x'}^2 dx' \\ & + \frac{1}{2} \left[2 c_{11}^E b \int_0^{L_e} \left\{ \int_h^{h+t_p} \left(-z' w_{e_{x'},x'x'} + d_{31} \frac{V_T}{2t_p} \right) \left(-z' w_{e_{x'},x'x'} \right) dz' \right\} dx' \right] \Bigg) \\ & + \frac{1}{2} k_f w_{e_0}^2 \end{aligned} \tag{2.64}$$

where $h = t_b / 2$.

Performing the integrations, Equation (2.64) reduces to

$$U=\sum_{e=1}^{N}\left(\frac{1}{2}\int_{0}^{L_e}\left[E_tI_tw_{e_{x',x'x'}}^2-bc_{11}^Ed_{31}V_T\left(h+t_p/2\right)w_{e_{x',x'x'}}\right]dx'\right)+\frac{1}{2}k_fw_{e_0}^2 \qquad (2.65)$$

where $E_tI_t=E_bI_b+\frac{2}{3}c_{11}^Eb\left(3h^2t_p+3ht_p^2+t_p^3\right)$.

As the electric voltage is related to the electric charge by

$$V_T=R_L\dot{Q} \qquad (2.66)$$

Substituting Equations (2.53) and (2.66) into Equation (2.65), it reduces to

$$U=\frac{1}{2}\sum_{e=1}^{N}\left[\mathbf{U}_e^T\mathbf{K}_e\mathbf{U}_e-\left(bc_{11}^Ed_{31}R_L\dot{Q}\left(h+t_p/2\right)\mathbf{B}_e^T\mathbf{U}_e\right)\right]+\frac{1}{2}\mathbf{U}^T\mathbf{K}_F\mathbf{U} \qquad (2.67)$$

where $\mathbf{K}_e=\int_0^{L_e}E_tI_t\mathbf{N}_{,x'x'}^T\mathbf{N}_{,x'x'}dx'$, $\mathbf{K}_F=\mathbf{a}_3^Tk_f\mathbf{a}_3$ with $\mathbf{a}_3=\left\{1\quad \mathbf{0}_{1\times(2N+1)}\right\}$, and $\mathbf{B}_e=\left[\int_0^{L_e}\mathbf{N}_{,x'x'}dx'\right]^T$.

After assembly of all the beam elements, Equation (2.67) reduces to

$$U=\frac{1}{2}\mathbf{U}^T\left(\mathbf{K}_b+\mathbf{K}_F\right)\mathbf{U}-\frac{1}{2}\left(bc_{11}^Ed_{31}R_L\dot{Q}\left(h+t_p/2\right)\mathbf{B}^T\mathbf{U}\right) \qquad (2.68)$$

where $\mathbf{K}_b$ is the global stiffness matrix of the composite piezoelectric beam and $\mathbf{B}$ is the global vector of piezoelectric action.

2.4.3. Electric Energy (W_e)

The expression of electric energy of the *CPEHDM* system is given by

$$W_e=\sum_{e=1}^{N}\left(\frac{1}{2}\int_{\Omega_P}E_3D_3d\Omega_P\right) \qquad (2.69)$$

where D_3 is the electric displacement.

Now, from the constitutive equations of piezoelectric materials (ANSI/IEEE STD 176-1987), we have

$$D_3 = d_{31}T_1 + \in_{33}^{T} E_3 \tag{2.70}$$

where $\in_{33}^{T}$ is the permittivity at constant stress.

Substituting Equations (2.62) and (2.70) into Equation (2.69), gives

$$\begin{aligned} W_e = \sum_{e=1}^{N} \Bigg(\frac{1}{2} \Bigg[2b \int_0^{L_e} \Bigg\{ \int_h^{h+t_p} \Bigg(d_{31} c_{11}^{E} \left(-z' w_{e_{x'},x'x'} \right) \left(\frac{-V_T}{2t_p} \right) \\ -d_{31}^2 c_{11}^{E} \left(\frac{V_T}{2t_p} \right)^2 + \in_{33}^{T} \left(\frac{V_T}{2t_p} \right)^2 \Bigg) dz' \Bigg\} dx' \Bigg] \Bigg) \end{aligned} \tag{2.71}$$

Evaluating the integrals in Equation (2.71) and utilizing Equations (2.53) and (2.66), we get

$$\begin{aligned} W_e = \sum_{e=1}^{N} \Bigg(\frac{1}{2} \left(b c_{11}^{E} d_{31} R_L \dot{Q} \left(h + t_p / 2 \right) \right) \mathbf{B}_e^T \mathbf{U}_e \\ -b L_e d_{31}^2 c_{11}^{E} \left(R_L^2 / 4t_p \right) \dot{Q}^2 + b L_e \in_{33}^{T} \left(R_L^2 / 4t_p \right) \dot{Q}^2 \Bigg) \end{aligned} \tag{2.72}$$

The permittivity component at constant strain is related to the permittivity at constant stress by

$$\in_{33}^{S} = \in_{33}^{T} - d_{31}^2 c_{11}^{E} \tag{2.73}$$

Substituting Equation (2.73) into Equation (2.72), gives

$$W_e = \sum_{e=1}^{N} \left(\frac{1}{2} \left(b c_{11}^{E} d_{31} R_L \dot{Q} \left(h + t_p / 2 \right) \right) \mathbf{B}_e^T \mathbf{U}_e + b L_e \in_{33}^{S} \left(R_L^2 / 4t_p \right) \dot{Q}^2 \right) \tag{2.74}$$

After assembly of all the beam elements, Equation (2.74) reduces to

$$W_e = \frac{1}{2} \left(b c_{11}^{E} d_{31} R_L \dot{Q} \left(h + t_p / 2 \right) \right) \mathbf{B}^T \mathbf{U} + b L \in_{33}^{S} \left(R_L^2 / 4t_p \right) \dot{Q}^2 \tag{2.75}$$

2.4.4. *Undamped Equations of Motion*

The Lagrange's undamped electromechanical equations of motion associated with the mechanical and electric degrees of freedom $\mathbf{U}$ and Q are derived as

$$\frac{d}{dt}\left\{\frac{\partial \mathrm{L}}{\partial \dot{\mathbf{U}}}\right\}-\frac{\partial \mathrm{L}}{\partial \mathbf{U}}=\mathbf{Q}_{nc_{\mathrm{U}}} \tag{2.76}$$

$$\frac{d}{dt}\left\{\frac{\partial \mathrm{L}}{\partial \dot{Q}}\right\}-\frac{\partial \mathrm{L}}{\partial Q}=Q_{nc_Q} \tag{2.77}$$

where $\mathbf{Q}_{nc_{\mathrm{U}}}=\mathbf{0}$ is the nonconservative mechanical load vector associated with the deflection vector $\mathbf{U}$, and $Q_{nc_Q}=-R_L\dot{Q}$ is the nonconservative electric load associated with the electric charge Q.

The Lagrangian L is given by

$$\mathrm{L}=T-U+W_e \tag{2.78}$$

Substituting Equations (2.58), (2.68), and (2.75) into Equation (2.78), gives

$$\begin{aligned}\mathrm{L}=&\frac{1}{2}\left(\dot{\mathbf{U}}+\dot{\mathbf{U}}_{base}\right)^T\left[\mathbf{M}_b+\mathbf{M}_F+\mathbf{M}_L\right]\left(\dot{\mathbf{U}}+\dot{\mathbf{U}}_{base}\right)\\&-\frac{1}{2}\mathbf{U}^T\left[\mathbf{K}_b+\mathbf{K}_F\right]\mathbf{U}+\Gamma\mathbf{B}^T\dot{Q}\mathbf{U}+\frac{C_P}{4}R_L^2\dot{Q}^2\end{aligned} \tag{2.79}$$

where $\Gamma=bc_{11}^E d_{31}\left(h+t_p/2\right)R_L$ and $C_P=bL\in_{33}^S/t_p$ is the internal capacitance of a single piezoelectric layer.

Accordingly, the resulting Lagrange's undamped electromechanical equations of the *CPEHDM* system are

$$\mathbf{M}_{uu}\ddot{\mathbf{U}}+\mathbf{K}_{uu}\mathbf{U}-\Gamma\mathbf{B}\dot{Q}=-\mathbf{M}_{uu}\ddot{\mathbf{U}}_{base} \tag{2.80}$$

$$\Gamma\mathbf{B}^T\dot{\mathbf{U}}+\frac{C_P}{2}R_L^2\ddot{Q}=-R_L\dot{Q} \tag{2.81}$$

where $\mathbf{M}_{uu} = \mathbf{M}_b + \mathbf{M}_F + \mathbf{M}_L$ is the total global mass matrix and $\mathbf{K}_{uu} = \mathbf{K}_b + \mathbf{K}_F$ is the total global stiffness matrix.

Now, the relative vibration response of the undamped composite piezoelectric beam can be found using the following linear transformation

$$\mathbf{U} = \mathbf{\Phi}_u \boldsymbol{\eta} \tag{2.82}$$

where $\mathbf{\Phi}_u$ is the mass normalized modal matrix and $\boldsymbol{\eta}$ is the global nodal vector of modal mechanical response.

The rth natural frequency ω_r and the corresponding eigenvector $\mathbf{\Delta}_r$ of the *CPEHDM* system are obtained under short-circuit conditions using the following standard algebraic eigenvalue problem

$$\mathbf{K}_{uu}\mathbf{\Delta}_r = \omega_r^2 \mathbf{M}_{uu}\mathbf{\Delta}_r \tag{2.83}$$

2.4.5. Damped Equations of Motion

Two types of mechanical damping are used in the analysis of the *CPEHDM* system. The first is referred to as the viscous air damping whereas the second is known as the strain rate damping due to structural viscoelasticity. In fact, the viscous air damping acts on the absolute velocity whereas the strain rate damping acts on the relative velocity of the composite piezoelectric beam [10].

Accordingly, Equation (2.80) can be written for the damped composite piezoelectric beam as

$$\mathbf{M}_{uu}\ddot{\mathbf{U}} + \left(\mathbf{D}_a + \mathbf{D}_s\right)\dot{\mathbf{U}} + \mathbf{K}_{uu}\mathbf{U} - \Gamma\mathbf{B}\dot{Q} = -\mathbf{M}_{uu}\ddot{\mathbf{U}}_{base} - \mathbf{D}_a\dot{\mathbf{U}}_{base} \tag{2.84}$$

where $\mathbf{D}_a$ is the global damping matrix due to viscous air damping and $\mathbf{D}_s$ is the global damping matrix due to structural viscoelasticity. Therefore, the total global damping matrix of the composite piezoelectric beam is

$$\mathbf{D}_{uu} = \mathbf{D}_a + \mathbf{D}_s \tag{2.85}$$

The mechanical damping ratio ζ_r of the rth mode of vibration which includes the effect of both viscous air damping and strain rate damping is given by [10,11]

$$\zeta_r = \zeta_r^a + \zeta_r^s = \frac{c_a}{2m_t\hat{\omega}_r} + \frac{c_s I_t \hat{\omega}_r}{2E_t I_t} \tag{2.86}$$

where ζ_r^a is the viscous air damping component of the damping ratio, ζ_r^s is the strain rate damping component of the damping ratio, c_a is the viscous air damping coefficient, $c_s I_t$ is the equivalent damping term of the beam cross-section due to structural viscoelasticity, and $\hat{\omega}_r$ is the rth natural frequency of the composite piezoelectric beam in the absence of the dynamic magnifier and the end mass M .

Equation (2.86) indicates that the viscous air damping is assumed to be proportional to the mass per unit length whereas strain rate damping is assumed to be proportional to the flexural stiffness of the beam. This idealized modeling assumption allows the use of a standard modal analysis approach.

Equations (2.81) and (2.84) can also be written as follows

$$\mathbf{M}_{uu}\ddot{\mathbf{U}} + \mathbf{D}_{uu}\dot{\mathbf{U}} + \mathbf{K}_{uu}\mathbf{U} - \Gamma\mathbf{B}\dot{Q} = -\mathbf{M}_{uu}\ddot{\mathbf{U}}_{base} - \mathbf{D}_a\dot{\mathbf{U}}_{base} \tag{2.87}$$

$$\Gamma\mathbf{B}^T\dot{\mathbf{U}} + \frac{C_P}{2}R_L^2\ddot{Q} + R_L\dot{Q} = 0 \tag{2.88}$$

Substituting Equation (2.82) into Equations (2.87) and (2.88), and premultiplying Equation (2.87) by $\mathbf{\Phi}_u^T$, we get

$$\bar{\mathbf{M}}_{uu}\ddot{\boldsymbol{\eta}}+\bar{\mathbf{D}}_{uu}\dot{\boldsymbol{\eta}}+\bar{\mathbf{K}}_{uu}\boldsymbol{\eta}-\boldsymbol{\Psi}\dot{Q}=\bar{\mathbf{F}} \tag{2.89}$$

$$\boldsymbol{\Psi}^T\dot{\boldsymbol{\eta}}+\frac{C_P}{2}R_L^2\ddot{Q}+R_L\dot{Q}=0 \tag{2.90}$$

where $\bar{\mathbf{M}}_{uu}=\boldsymbol{\Phi}_u^T\mathbf{M}_{uu}\boldsymbol{\Phi}_u$ is the total global mass normalized mass matrix, $\bar{\mathbf{D}}_{uu}=\boldsymbol{\Phi}_u^T\mathbf{D}_{uu}\boldsymbol{\Phi}_u$ is the total global mass normalized damping matrix, $\bar{\mathbf{K}}_{uu}=\boldsymbol{\Phi}_u^T\mathbf{K}_{uu}\boldsymbol{\Phi}_u$ is the total global mass normalized stiffness matrix, and $\boldsymbol{\Psi}=\Gamma\bar{\mathbf{B}}$ is the electromechanical coupling vector with $\bar{\mathbf{B}}=\boldsymbol{\Phi}_u^T\mathbf{B}$.

The modal mechanical forcing vector $\bar{\mathbf{F}}$ for a harmonic translating base can be written as follows

$$\bar{\mathbf{F}}=-\boldsymbol{\Phi}_u^T\mathbf{M}_{uu}\ddot{\mathbf{U}}_{base}-\boldsymbol{\Phi}_u^T\mathbf{D}_a\dot{\mathbf{U}}_{base} \tag{2.91}$$

For harmonic base excitations at a frequency ω such that

$$\mathbf{U}_{base}=\boldsymbol{\Delta}_{base}e^{j\omega t} \tag{2.92}$$

Then, the corresponding solutions can be assumed to be

$$\boldsymbol{\eta}=\boldsymbol{\Pi}e^{j\omega t},\quad Q=Q_0e^{j\omega t} \tag{2.93}$$

Substituting Equations (2.92) and (2.93) into Equations (2.89) and (2.90), gives

$$\left(\bar{\mathbf{K}}_{uu}-\omega^2\bar{\mathbf{M}}_{uu}+j\omega\bar{\mathbf{D}}_{uu}\right)\boldsymbol{\Pi}-j\omega\boldsymbol{\Psi}Q_0=\bar{\mathbf{F}}_0 \tag{2.94}$$

$$j\omega\boldsymbol{\Psi}^T\boldsymbol{\Pi}+\left(j\omega R_L-\omega^2\frac{C_P}{2}R_L^2\right)Q_0=0 \tag{2.95}$$

where $\bar{\mathbf{F}}_0$ denotes the nodal amplitude of the modal mechanical forcing vector. It is given by

$$\bar{\mathbf{F}}_0=\omega^2\boldsymbol{\Phi}_u^T\mathbf{M}_{uu}\boldsymbol{\Delta}_{base}-j\omega\boldsymbol{\Phi}_u^T\mathbf{D}_a\boldsymbol{\Delta}_{base} \tag{2.96}$$

Equations (2.94) and (2.95) can be solved for the steady-state electric charge and the global nodal vector of modal mechanical response as follows

$$Q(t) = \frac{j\mathbf{\Psi}^T \overline{\mathbf{Z}}_u^{-1} \overline{\mathbf{F}}_0}{\omega \frac{C_P}{2} R_L^2 - jR_L + \omega \mathbf{\Psi}^T \overline{\mathbf{Z}}_u^{-1} \mathbf{\Psi}} e^{j\omega t} \tag{2.97}$$

$$\boldsymbol{\eta}(t) = \overline{\mathbf{Z}}_u^{-1} \left(\overline{\mathbf{F}}_0 + j\omega \mathbf{\Psi} Q_0 \right) e^{j\omega t} \tag{2.98}$$

Using Equation (2.82), the steady-state global nodal deflection vector of the composite piezoelectric beam is given by

$$\mathbf{U}(t) = \mathbf{\Phi}_u \overline{\mathbf{Z}}_u^{-1} \left(\overline{\mathbf{F}}_0 + j\omega \mathbf{\Psi} Q_0 \right) e^{j\omega t} \tag{2.99}$$

where $\overline{\mathbf{Z}}_u = \overline{\mathbf{K}}_{uu} - \omega^2 \overline{\mathbf{M}}_{uu} + j\omega \overline{\mathbf{D}}_{uu}$ is the total global mass normalized impedance matrix.

Equations (2.97) and (2.99) will be used to predict the performance of the *CPEHDM* system as function of its design and load parameters.

2.5. Performance of the cantilevered piezoelectric energy harvester

In this section, numerical examples are presented to illustrate the performance characteristics of the *CPEHDM* in comparison with the conventional piezoelectric energy harvester (*CPEH*). The different geometric and material parameters of the system are listed in Table 2.1 [40].

2.5.1. Performance of the CPEH

Figure 2.5 shows the effect of the load resistance on the peak amplitude of the electric power output of the *CPEH*. The displayed characteristics are obtained for base excitations at the short-circuit and open-circuit resonant frequencies of the first

vibration mode. The base excitation considered, in all this study, is a sinusoidal excitation that has an acceleration of $1g$ which is maintained constant over the entire frequency range.

The figure shows also comparisons between the predictions using both, the analytical and finite element models. The displayed results indicate close agreement between the two models.

Note that the short-circuit (f_1^{sc}) and open-circuit (f_1^{oc}) resonant frequencies occur at $f_1^{sc} = 70.135\,Hz$ and $f_1^{oc} = 73.925\,Hz$, respectively. The corresponding maximum electric powers of the energy harvester are both equal to $P_{\max}^{sc} = P_{\max}^{oc} = 5.5\,mW$ and are attained at load resistances of $R_L^{sc} = 8,700\,\Omega$ and $R_L^{oc} = 69,000\,\Omega$, respectively. Because of the similarity of the performance under short-circuit and open-circuit conditions, the remaining part of the results will concentrate only on the short-circuit conditions.

Table 2.1: Geometric and material properties of the energy harvester [40]

Overall Properties		Value
m_t / L	Total mass of the composite beam per unit length	96 *g/m*
M	End mass	1.5 *g*
b	Beam width	20 *mm*
L	Beam length	50 *mm*
ζ_1	Damping ratio for the first mode of vibration	0.02
ζ_2	Damping ratio for the second mode of vibration	0.026
Beam Properties		**Value**
s_{11}^b	Compliance of the beam	5 x 10^{-11} m^2/N
t_b	Beam thickness	0.2 *mm*
Piezoelectric Properties		**Value**
s_{11}^E	Compliance of the piezoelectric material	1.64 x 10^{-11} m^2/N
d_{31}	Piezoelectric strain coefficient	-320 x 10^{-12} *C/N*
ε_{33}^T	Permittivity at constant stress	3.98 x 10^{-8} *F/m*
t_p	Thickness of each piezoelectric patch	0.2 *mm*
Magnifier Properties		**Value**
M_f	Magnifier mass	M, $5M$, $10M$, $15M$
k_f	Magnifier stiffness	$k_f = M_f \omega_1^2$ *

* ω_1 is the fundamental natural frequency of the beam when $M_f = 0$ and $k_f \to \infty$.

The effect of the excitation frequency on the peak amplitude of the electric power output of the *CPEH* is shown in Figure 2.6 at the optimal resistive load, $R_L^{sc} = 8,700\,\Omega$, corresponding to the short-circuit condition.

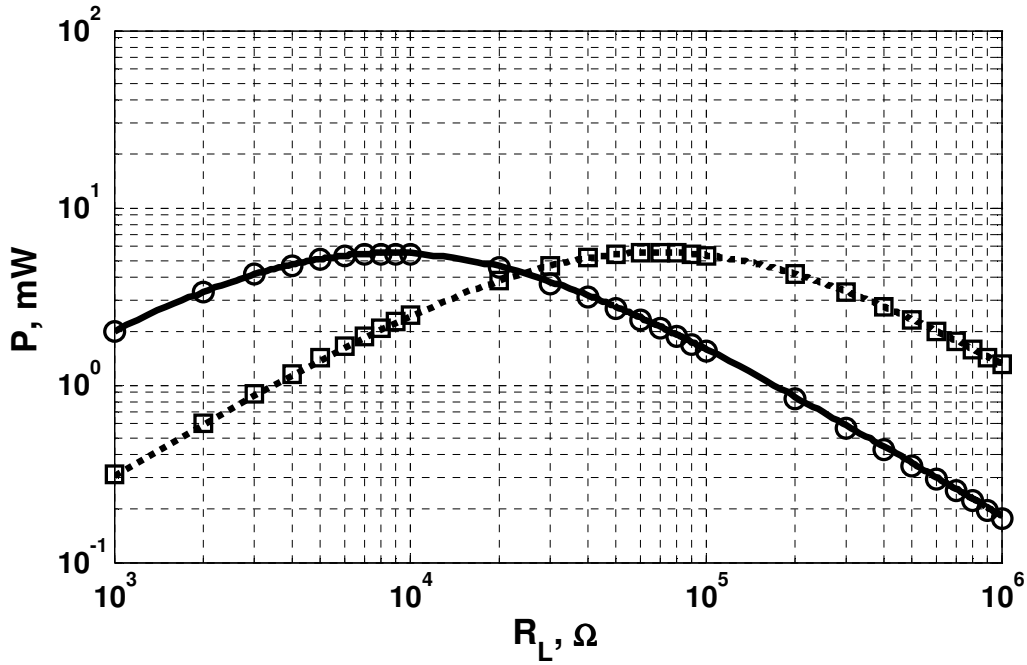

Figure 2.5: Effect of the load resistance on the peak amplitude of the electric power output of the *CPEH* for base excitations at the short-circuit (——— distributed parameter, ○ finite element) and open-circuit (▪▪▪▪▪▪▪▪▪ distributed parameter, □ finite element) resonant frequencies of the first vibration mode

The figure also shows comparisons between the predictions using the distributed parameter and finite element models which also shows excellent agreement as expected.

2.5.2. Performance of the CPEHDM

Figure 2.7(a) shows the effect of the load resistance on the peak amplitude of the electric power output of the *CPEHDM* as compared with the corresponding characteristics of the *CPEH*. The displayed curves are obtained for base excitations at the short-circuit resonant frequency of the first vibration mode when $k_f = M_f \omega_1^2$ and $M_f = M$. For the first vibration mode, it is found that $f_1^{sc} = 29.160\,Hz$ and $f_1^{oc} = 29.300\,Hz$ with peak powers of $P_{\max}^{sc} = P_{\max}^{oc} = 10.2\,mW$ occurring at

$R_L^{sc} = 54,000\,\Omega$ and $R_L^{oc} = 57,000\,\Omega$, respectively. Accordingly, the use of the *CPEHDM* has resulted in about doubling the peak harvested power of the *CPEH*.

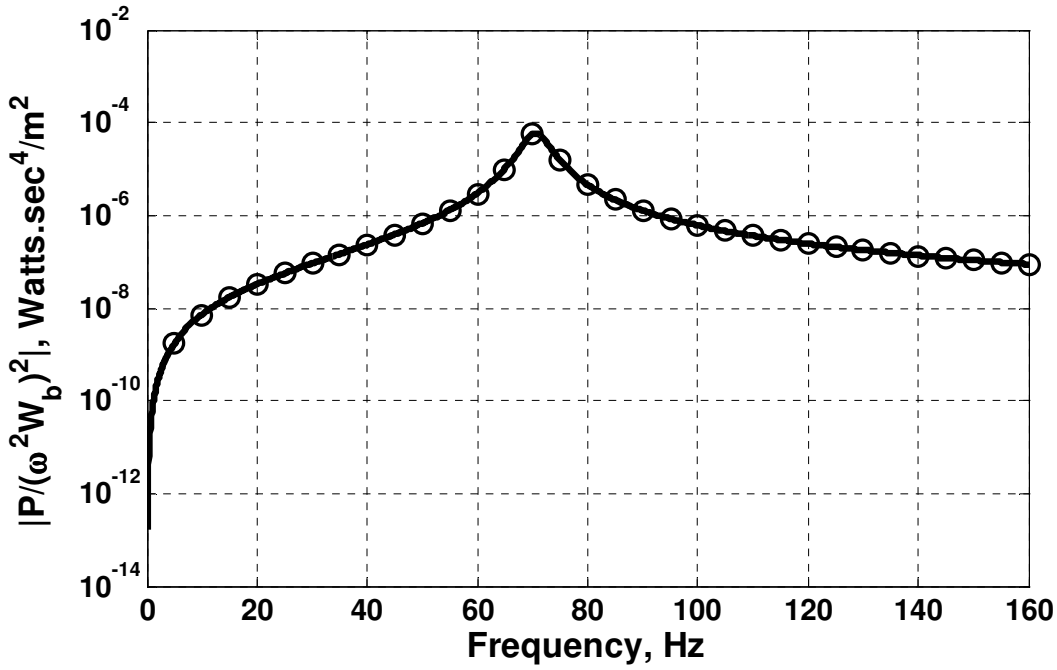

Figure 2.6: Effect of the excitation frequency on the peak amplitude of the electric power output of the *CPEH* for the short-circuit resonant condition (——— distributed parameter, ○ finite element)

The corresponding frequency response of the peak amplitude of the electric power output of the *CPEHDM* in comparison with that of the *CPEH* is shown in Figure 2.7(b) for the optimal resistive load corresponding to the short-circuit condition. The figure indicates also that the *CPEHDM* has an additional mode of vibration appearing at a frequency of $113\,Hz$ in the considered frequency band. However, the electric power harvested at this second mode is about $34.77\,\mu W$, *i.e.* about three orders of magnitude lower than that of the first vibration mode. Note also that the frequency band between the first and second modes is about $84\,Hz$.

Increasing the mass of the dynamic magnifier with respect to the end mass to 5, *i.e.* $M_f = 5M$, yields the characteristics shown in Figure 2.8 for the effect of load resistance and excitation frequency on the output power of the *CPEHDM* in comparison with that of the *CPEH* at the short-circuit condition. For the first vibration mode, it is found that $f_1^{sc} = 46.485\,Hz$ and $f_1^{oc} = 47.035\,Hz$ with peak powers of $P_{\max}^{sc} = P_{\max}^{oc} = 18.2\,mW$ occurring at $R_L^{sc} = 30,000\,\Omega$ and $R_L^{oc} = 40,000\,\Omega$, respectively. Accordingly, the use of the *CPEHDM* has resulted in magnifying the peak harvested power of the *CPEH* by about 330%.

In Figure 2.8(b), the second mode of vibration of the *CPEHDM* appears now at $97.7\,Hz$ resulting in a frequency band between the first and second modes of about $52.2\,Hz$ which is narrower than that observed for the case when $M_f = M$. Moreover, the electric power harvested at this second mode has increased considerably to $718.88\,\mu W$ as compared to the case when $M_f = M$. Now, it is about 3.9% of the magnitude of the first mode.

Figure 2.9 and Figure 2.10 display the corresponding characteristics of the *CPEHDM* in comparison with those of the *CPEH* when $M_f = 10M$ and $M_f = 15M$, respectively. When $M_f = 10M$, it is found that $f_1^{sc} = 52.610\,Hz$ and $f_1^{oc} = 53.385\,Hz$ with peak powers of $P_{\max}^{sc} = P_{\max}^{oc} = 25.35\,mW$ occurring at $R_L^{sc} = 24,000\,\Omega$ and $R_L^{oc} = 37,000\,\Omega$, respectively. This indicates that the use of the *CPEHDM* has resulted in magnifying the peak harvested power of the *CPEH* by 460%. Increasing M_f to become equal to $15M$ makes $f_1^{sc} = 55.590\,Hz$ and

$f_1^{oc} = 56.485\,Hz$ with peak powers of $P_{\max}^{sc} = P_{\max}^{oc} = 32.05\,mW$ OCcurring at $R_L^{sc} = 22,000\,\Omega$ and $R_L^{oc} = 36,000\,\Omega$, respectively. In this case, the magnification resulting from the use of the *CPEHDM* is 583%.

It is important to note that the magnified power of the *CPEHDM* becomes higher than that of the *CPEH* over a broader frequency range particularly as the M_f / M ratio increases. For example, when $M_f / M = 10$, the electric power harvested at the second mode is about $2.22\,mW$. It also increases to $4.06\,mW$ when $M_f / M = 15$, *i.e.* comparable to the case of the *CPEH*. This suggests clearly that the *CPEHDM* can be an effective means for harvesting the vibration energy over a broader frequency range than that of the *CPEH*.

Note that the effective bandwidth of the piezoelectric energy harvester is about $36.29\,Hz$ when $M_f / M = 10$ and becomes $30\,Hz$ when M_f / M increases to 15.

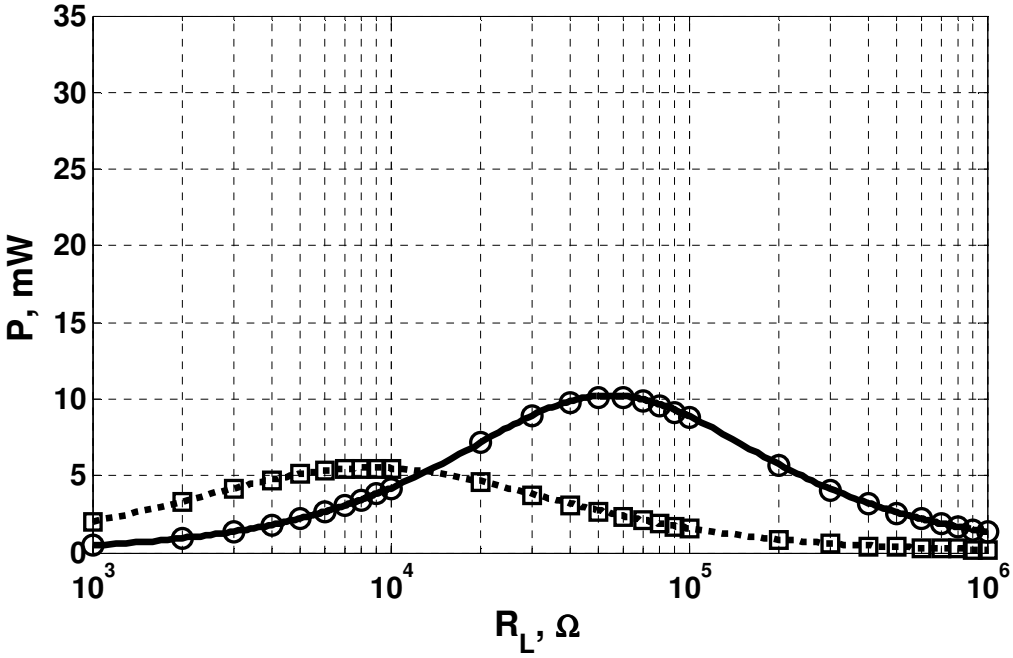

(a)

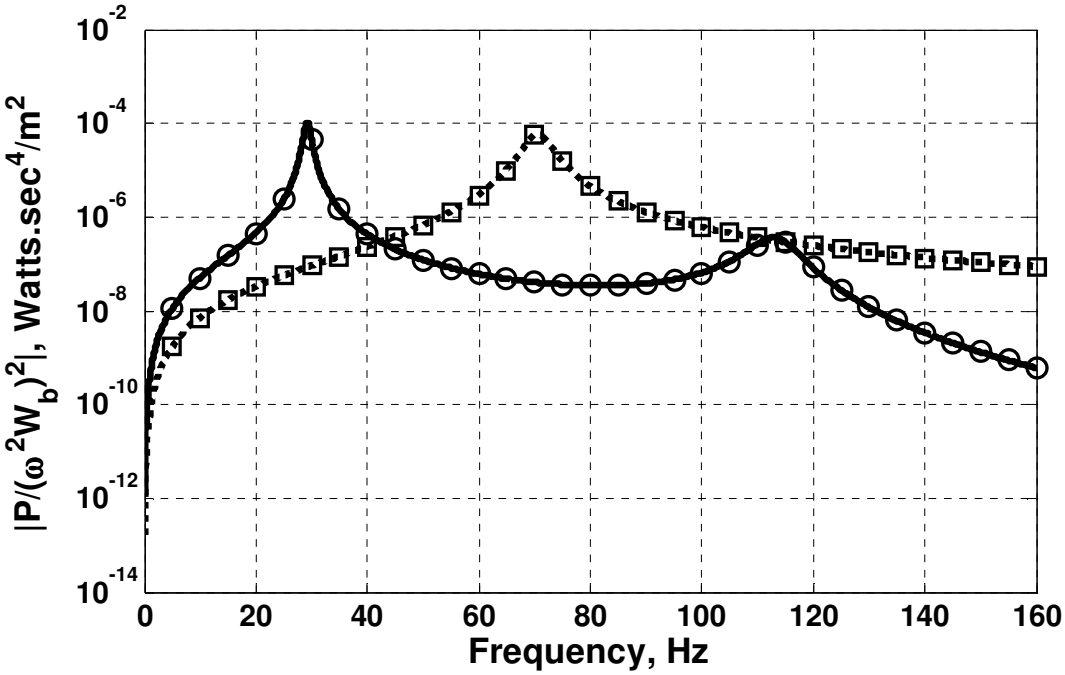

(b)

Figure 2.7: Effect of the load resistance (a) and excitation frequency (b) on the peak amplitude of the electric power output for the *CPEHDM* (——— distributed parameter, ○ finite element) with M_f=*M* and the *CPEH* (▪▪▪▪▪▪▪▪▪ distributed parameter, □ finite element) at the short-circuit condition of the first vibration mode

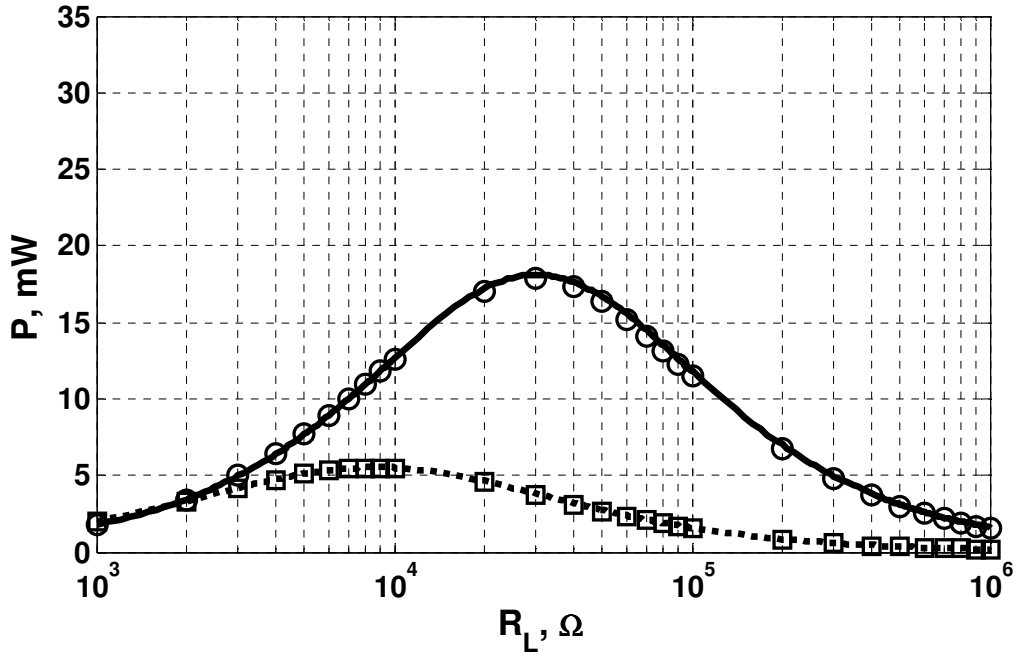

(a)

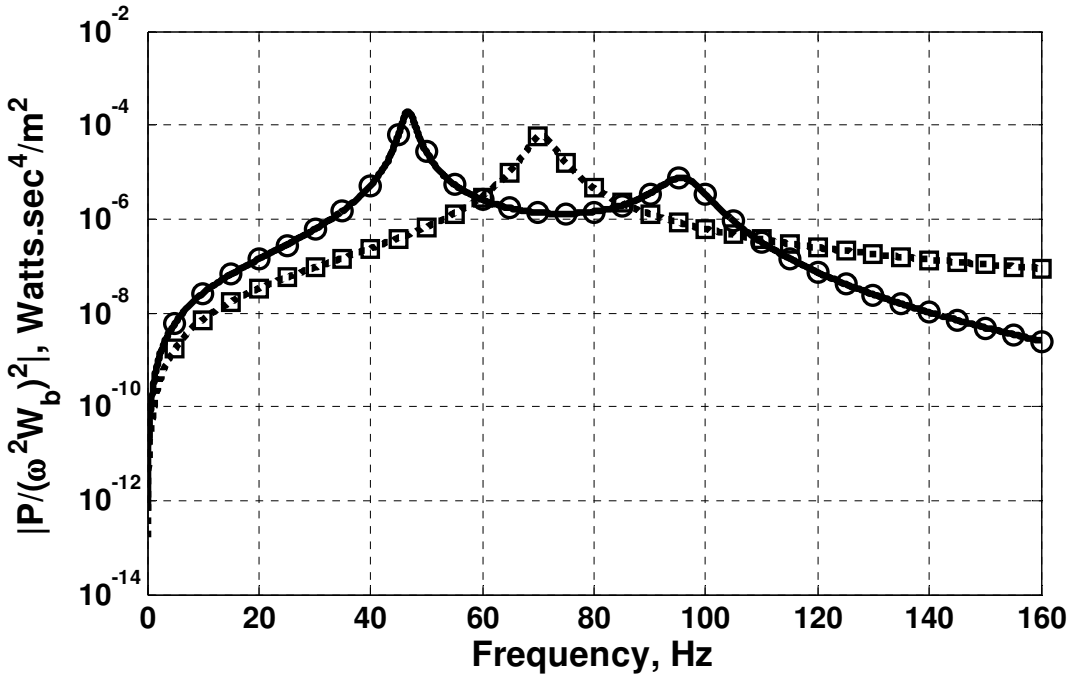

(b)

Figure 2.8: Effect of the load resistance (a) and excitation frequency (b) on the peak amplitude of the electric power output for the *CPEHDM* (——— distributed parameter, ○ finite element) with M_f=5M and the *CPEH* (▪▪▪▪▪▪▪▪▪ distributed parameter, □ finite element) at the short-circuit condition of the first vibration mode

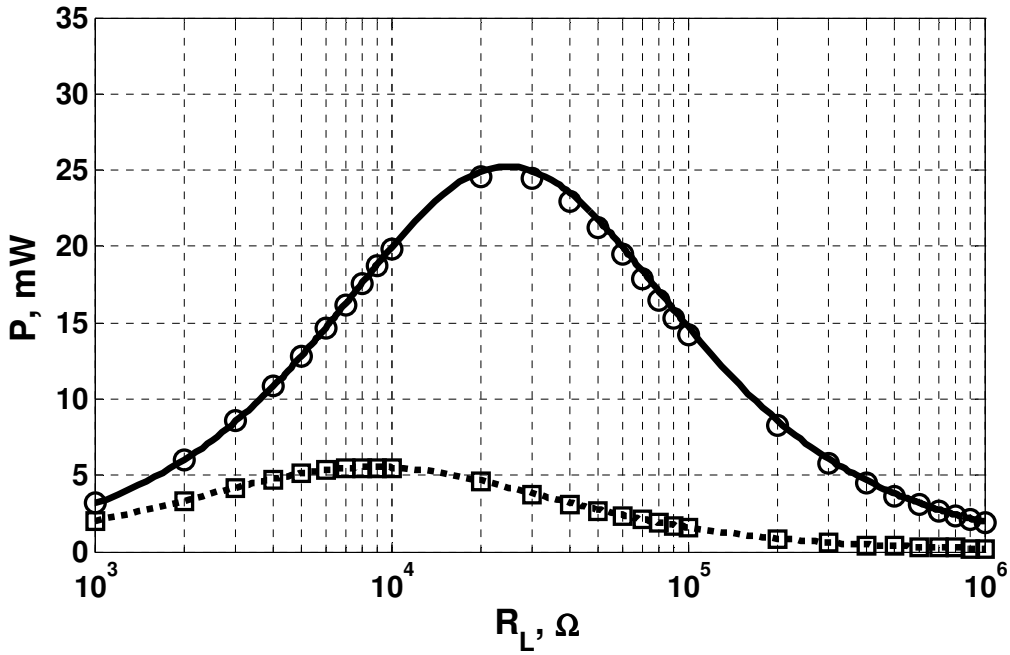

(a)

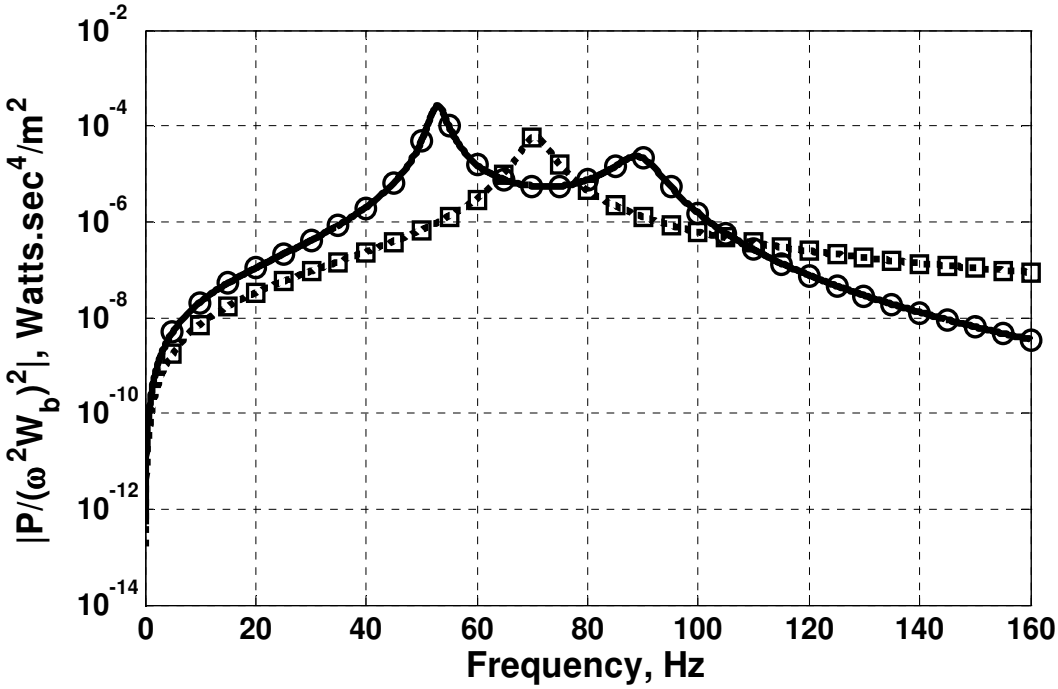

(b)

Figure 2.9: Effect of the load resistance (a) and excitation frequency (b) on the peak amplitude of the electric power output for the *CPEHDM* (▬▬▬ distributed parameter, ○ finite element) with M_f=10M and the *CPEH* (▪▪▪▪▪▪▪▪▪ distributed parameter, □ finite element) at the short-circuit condition of the first vibration mode

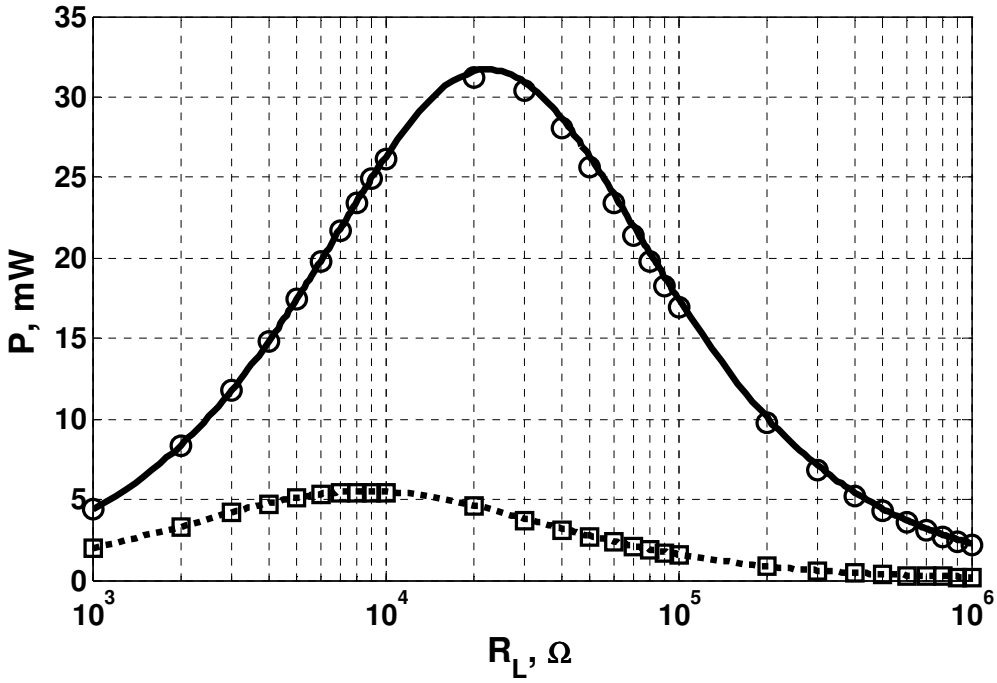

(a)

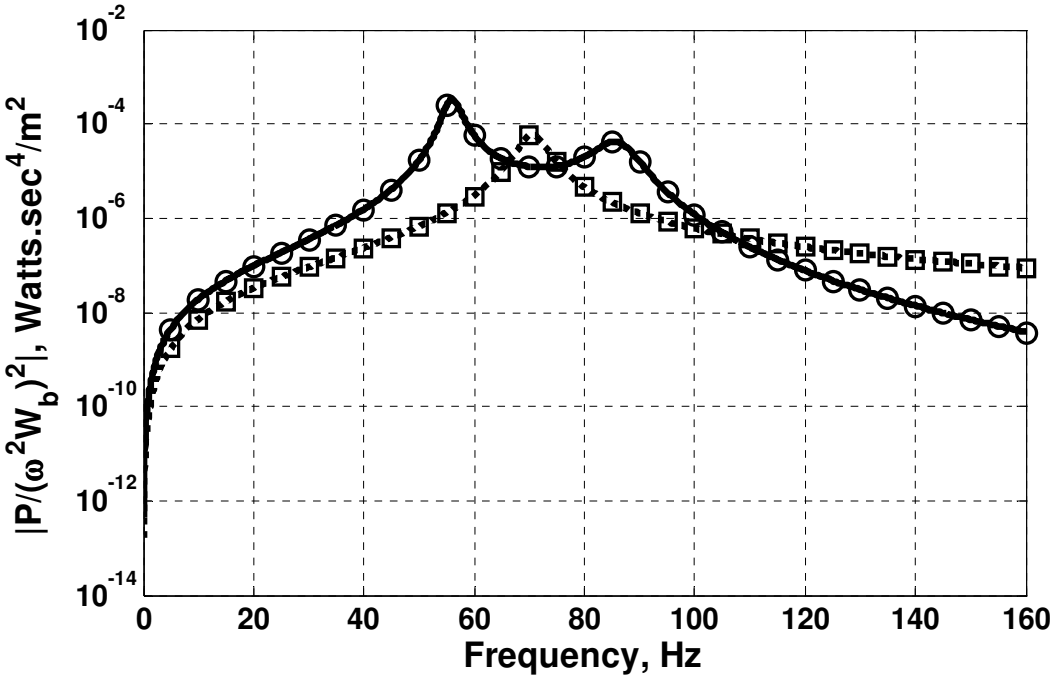

(b)

Figure 2.10: Effect of the load resistance (a) and excitation frequency (b) on the peak amplitude of the electric power output for the *CPEHDM* (▬▬▬ distributed parameter, ○ finite element) with M_f=15M and the *CPEH* (▪▪▪▪▪▪▪▪▪ distributed parameter, □ finite element) at the short-circuit condition of the first vibration mode

2.6. Conclusions

This chapter has presented a class of cantilevered piezoelectric energy harvesters which is augmented with a dynamic magnifier (*CPEHDM*) to dynamically amplify the harnessed electric power output. The theory governing the operation of this class of energy harvesters has been introduced using distributed parameter and finite element methods. Numerical examples are presented to illustrate the merits of the *CPEHDM* in comparison with the conventional piezoelectric energy harvesters (*CPEH*). It was shown that with proper selection of the design parameters of the *CPEH*DM, the harvested electric power can be amplified by a factor of 5 (*i.e.,* 500 percent) as compared to the *CPEH* and the effective bandwidth of the energy harvester can be widened to cover side bands that are about $\pm 21\%$ of the resonant frequency of the *CPEH*. The predictions of the distributed parameter model are compared with those obtained using the finite element approach and excellent agreement of the two models is observed for all the considered examples. The obtained results demonstrate the feasibility of the *CPEHDM* as a simple and effective means for enhancing the magnitude and spectral characteristics of the *CPEH*.

Chapter 3

3. Experimental Implementation of a Piezoelectric Energy Harvester with a Dynamic Magnifier

3.1. Introduction

The enhancement of the electric power output from piezoelectric vibration energy harvesters by using the concept of dynamic magnifiers has been proposed in Chapter 2. There, it was shown that the analytical results agree very well with the numerical ones and that with proper selection of the design parameters of the *CPEHDM*, the harvested electric power can be amplified significantly and the effective bandwidth of the energy harvester can be greatly widened. In this chapter, experimental investigations are performed to validate these results where a preferred implementation of the *CPEHDM* system can be done by using the setup shown in Figure 3.1. In this case, the dynamic magnifier takes the form of a cantilever beam to enable the adjustment of the stiffness by changing the beam length. The magnifier beam is anchored from its left end to an electromechanical shaker whereas the right end is attached to a piezoelectric energy harvester. At the left anchoring point, an accelerometer is mounted to monitor the input base acceleration whereas the right anchoring point is attached to the magnifier mass. The bimorph energy harvester used in this experiment has its two piezoelectric patches connected in parallel to the electric resistive load.

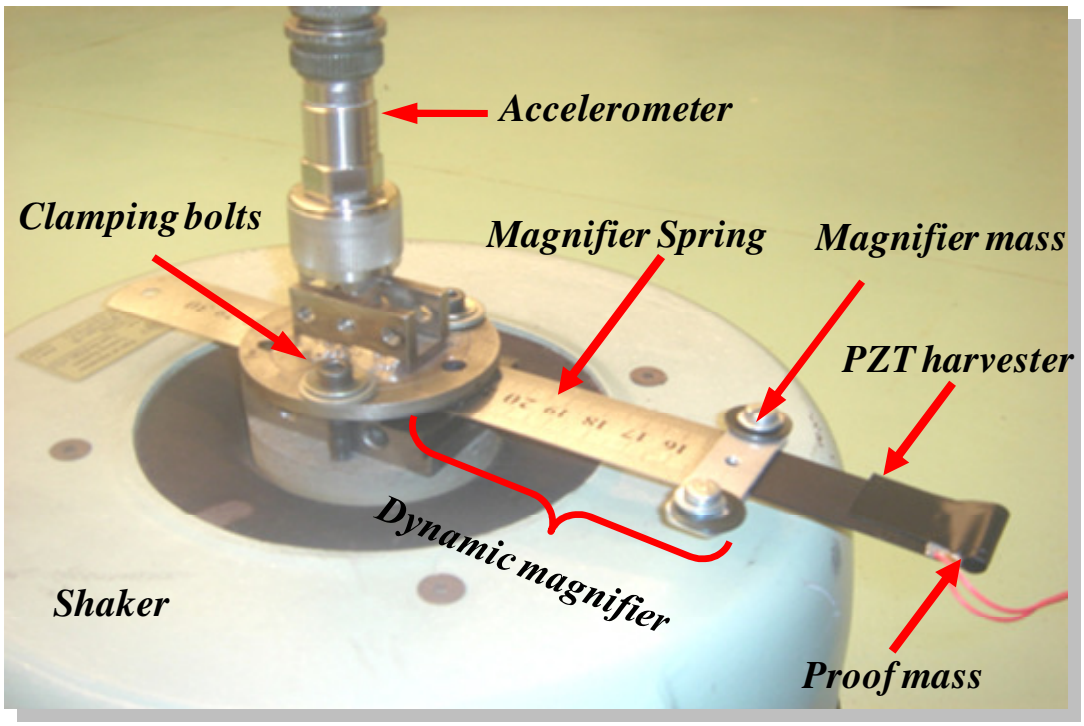

Figure 3.1: A photograph showing the experimental setup of the *CPEHDM* system

3.2. Finite Element Modeling

The details of the finite element modeling of piezoelectric energy harvesters augmented with dynamic magnifiers were documented in Chapter 2. However, since the experimental setup used here differs slightly from Figure 2.2, it is therefore worthwhile to briefly indicate where these differences occur. In doing so, the kinetic, potential, and electric energies associated with the new model can be analyzed in the following discussion.

The different components of the kinetic energy of the new *CPEHDM* system are given by

$$T_{1e} = \frac{1}{2}\int_0^{L_e} m_f \dot{w}_e^2 dx, \quad T_{2e} = \frac{1}{2}\int_0^{L_e} m_t \dot{w}_e^2 dx, \quad T_0 = \frac{1}{2} M_f \dot{w}_0^2, \quad T_L = \frac{1}{2} M \dot{w}_L^2 \tag{3.1}$$

where T_{1e} is the kinetic energy of the eth element of the magnifier beam, T_{2e} is the kinetic energy of the eth element of the energy harvester, T_0 is the kinetic energy of the magnifier mass M_f, and T_L is the kinetic energy of the end mass M. Also, m_f is the mass per unit length of the magnifier beam, and $m_t = m_b + 2m_p$ with m_b and m_p denoting the mass per unit length of the energy harvester substructure and a single piezoelectric patch, respectively.

The different components of the potential energy of the new *CPEHDM* system are given by

$$U_{1e} = \frac{1}{2}\int_0^{L_e} E_f I_f w_{e_x,xx}^2 dx, \quad U_{2e} = \frac{1}{2}\int_0^{L_e} E_b I_b w_{e_x,xx}^2 dx + \frac{1}{2}\int_{\Omega_P} T_1 S_1 d\Omega_P \tag{3.2}$$

where U_{1e} is the potential energy of the eth element of the magnifier beam, U_{2e} is the potential energy of the eth element of the energy harvester, $E_f I_f$ is the flexural rigidity of the magnifier beam, $E_b I_b$ is the flexural rigidity of the energy harvester substructure, T_1 is the stress in the piezoelectric layers, S_1 is the strain in the piezoelectric layers, and Ω_P is the volume of the piezoelectric layers of element *e*.

The expression of electric energy of the new *CPEHDM* system is given by

$$W_e = \sum_{e=1}^{N}\left(\frac{1}{2}\int_{\Omega_P} E_3 D_3 d\Omega_P\right) \tag{3.3}$$

where E_3 is the electric field and D_3 is the electric displacement.

Following a procedure similar to the one used in the finite element model of Chapter 2, the discretized equations of motion for this system can be written as

$$\bar{\mathbf{M}}_{uu}\ddot{\boldsymbol{\eta}} + \bar{\mathbf{D}}_{uu}\dot{\boldsymbol{\eta}} + \bar{\mathbf{K}}_{uu}\boldsymbol{\eta} - \boldsymbol{\Psi}\dot{Q} = \bar{\mathbf{F}} \tag{3.4}$$

$$\mathbf{\Psi}^T \dot{\boldsymbol{\eta}} + \frac{C_P}{2} R_L^2 \ddot{Q} + R_L \dot{Q} = 0 \tag{3.5}$$

where $\bar{\mathbf{M}}_{uu} = \mathbf{\Phi}_u^T \mathbf{M}_{uu} \mathbf{\Phi}_u$ is the total global mass normalized mass matrix, $\bar{\mathbf{D}}_{uu} = \mathbf{\Phi}_u^T \mathbf{D}_{uu} \mathbf{\Phi}_u$ is the total global mass normalized damping matrix, $\bar{\mathbf{K}}_{uu} = \mathbf{\Phi}_u^T \mathbf{K}_{uu} \mathbf{\Phi}_u$ is the total global mass normalized stiffness matrix, and $\mathbf{\Psi} = \Gamma \bar{\mathbf{B}}$ is the electromechanical coupling vector with $\bar{\mathbf{B}} = \mathbf{\Phi}_u^T \mathbf{B}$.

The steady-state electric charge and the global nodal vector of modal mechanical response can therefore be written as

$$Q(t) = \frac{j \mathbf{\Psi}^T \bar{\mathbf{Z}}_u^{-1} \bar{\mathbf{F}}_0}{\omega \frac{C_P}{2} R_L^2 - j R_L + \omega \mathbf{\Psi}^T \bar{\mathbf{Z}}_u^{-1} \mathbf{\Psi}} e^{j\omega t} \tag{3.6}$$

$$\boldsymbol{\eta}(t) = \bar{\mathbf{Z}}_u^{-1} \left(\bar{\mathbf{F}}_0 + j\omega \mathbf{\Psi} Q_0 \right) e^{j\omega t} \tag{3.7}$$

where $\bar{\mathbf{Z}}_u = \bar{\mathbf{K}}_{uu} - \omega^2 \bar{\mathbf{M}}_{uu} + j\omega \bar{\mathbf{D}}_{uu}$ is the total global mass normalized impedance matrix.

3.3. Experimental and Numerical Results

Three arrangements were tested to experimentally validate the proposed finite element model. These arrangements include a cantilevered piezoelectric bimorph, a cantilevered piezoelectric bimorph with end mass, and a cantilevered piezoelectric bimorph with end mass mounted on a dynamic magnifier as shown in Figure 3.2.

For all test arrangements, the piezoelectric energy harvester geometric and material properties are as listed in Table 2.1. However, the test arrangement shown in Figure 3.2(c) is augmented with a dynamic magnifier in the form of a cantilever beam to enable the adjustment of the stiffness by changing the beam length. The properties

of the magnifier beam are such that its mass density is $\rho_f = 7800\,kg/m^3$, its Young's modulus is $c_{11}^f = 200\,GPa$, and its thickness is $h_f = 25\,mm$. The magnifier beam length L is changed for a parametric study of the harvester performance. The two piezoelectric patches are connected in parallel to an electric load resistance and the voltage induced by the vibratory motion is measured as a consequence.

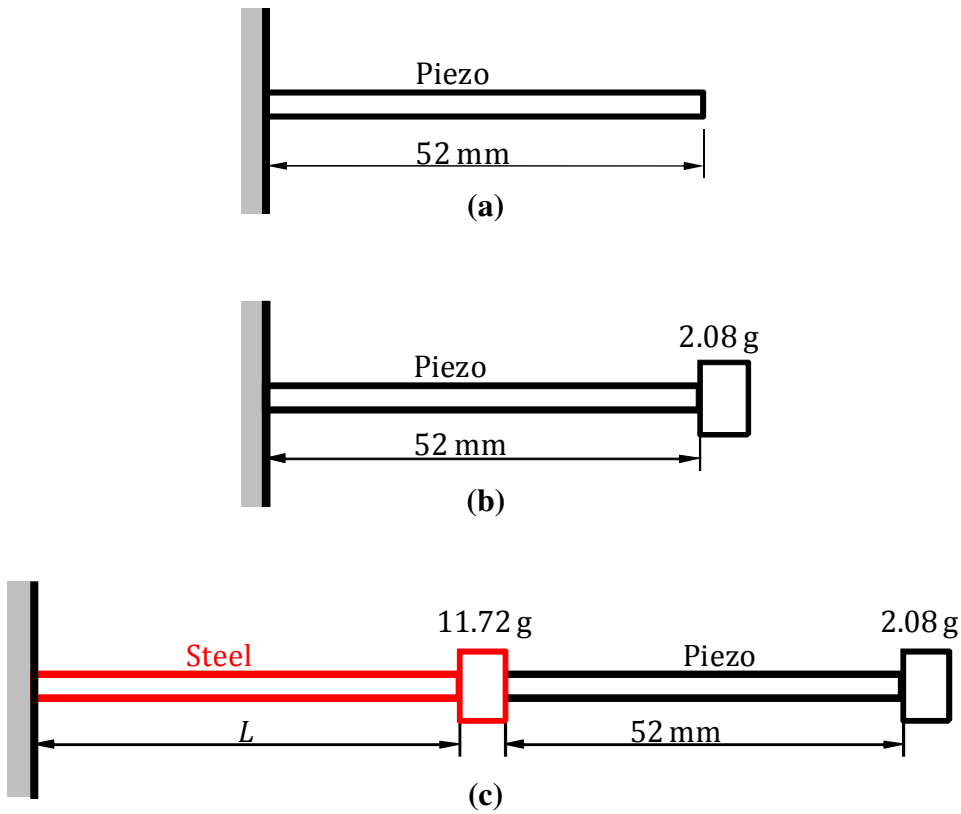

Figure 3.2: Test arrangements of the *CPEH* and *CPEHDM* systems

Figure 3.3 shows the experimental vs. numerical output voltage of the test arrangement shown in Figure 3.2(a) for different electric load resistances. It can be seen from the plots that the proposed numerical model very well captures the experimental behavior of the energy harvester.

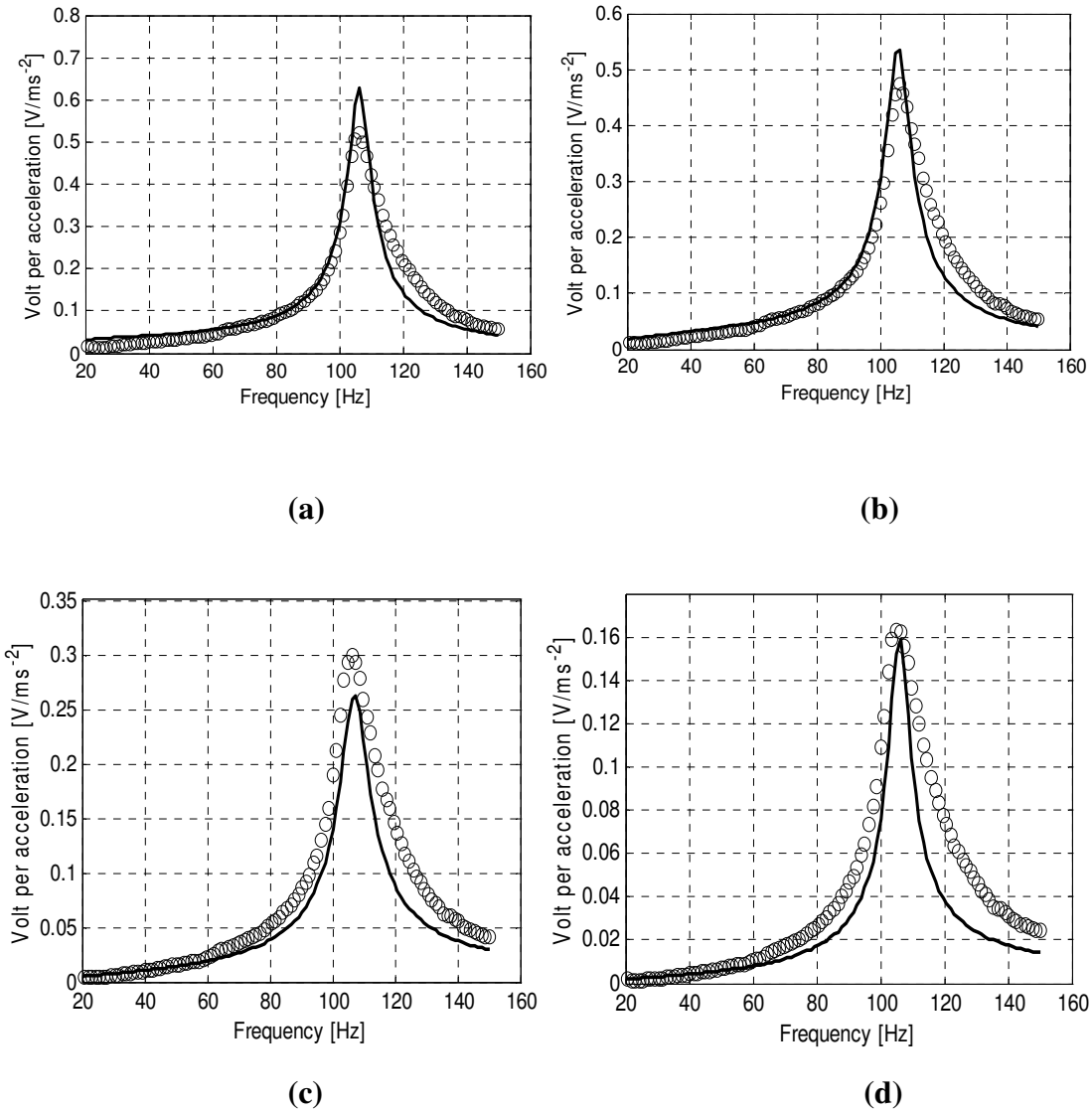

Figure 3.3: Experimental ○ vs. numerical ——— output voltage of the test arrangement shown in Figure 3.2(a) for: (a) R_L=*100 kohm*, (b) R_L=*40 kohm*, (c) R_L=*10 kohm*, and (d) R_L=*4 kohm*

Figure 3.4 shows the experimental and numerical output voltage of the test arrangement shown in Figure 3.2(b) for different electric load resistances. The end mass used here has a value of $M = 2.08\,g$. The obtained plots again show that the proposed numerical model results agree with the experimental performance characteristics of the energy harvester.

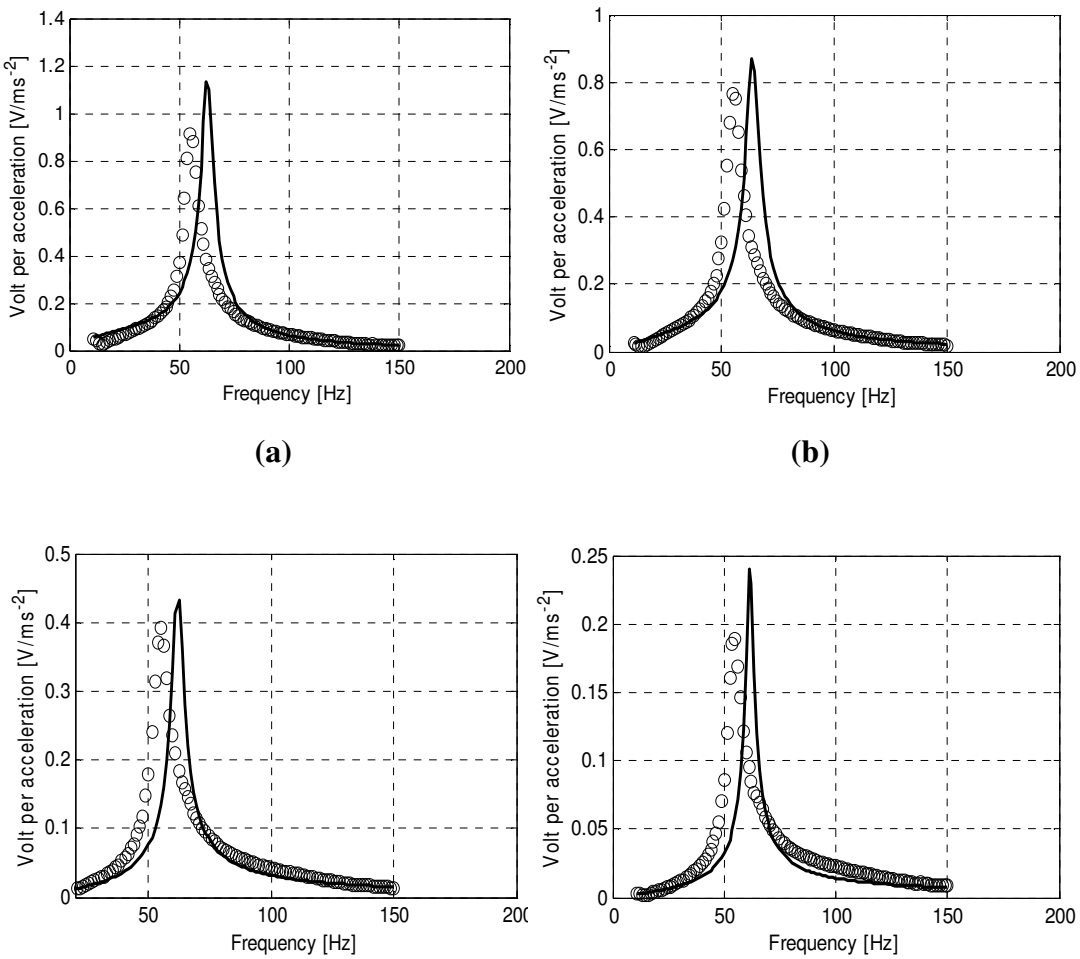

Figure 3.4: Experimental ○ vs. numerical ——— output voltage of the test arrangement shown in Figure 3.2(b) for: (a) R_L=100 *kohm*, (b) R_L=40 *kohm*, (c) R_L=10 *kohm*, and (d) R_L=4 *kohm*

Figure 3.5 and Figure 3.6 show the experimental vs. numerical output voltage of the test arrangement shown in Figure 3.2(c) when $L = 40\,mm$ and $L = 60\,mm$, respectively, for different electric load resistances. The magnifier mass used here has a value of $M_f = 11.72\,g$. It can be seen that when the energy harvester is provided

with a dynamic magnifier, the corresponding voltage/ms^{-2} can be improved significantly.

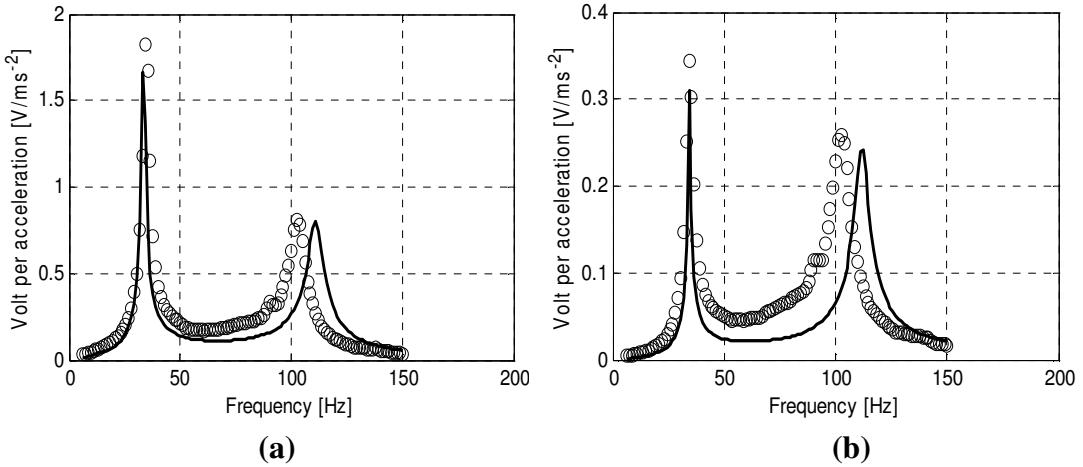

Figure 3.5: Experimental ○ vs. numerical ——— output voltage of the test arrangement shown in Figure 3.2(c) for: (a) R_L=*40 kohm*, and (b) R_L=*4 kohm*, when *L=40 mm*

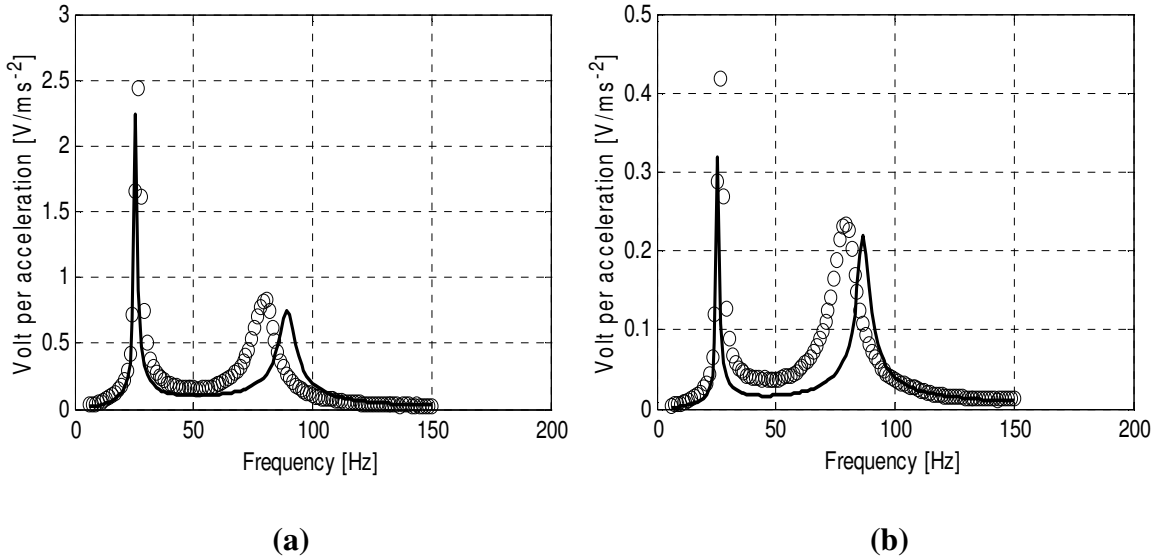

Figure 3.6: Experimental ○ vs. numerical ——— output voltage of the test arrangement shown in Figure 3.2(c) for: (a) R_L=*40 kohm*, and (b) R_L=*4 kohm*, when *L=60 mm*

More precise comparison analysis can be done by looking at the peak voltage produced by each of the test arrangements shown in Figure 3.2 for a specified value of the electric load resistance of the first vibration mode. For example, when $R_L = 40\,kohm$ and $L = 40\,mm$, the peak voltages produced from the different test arrangements of Figure 3.2 (from top to bottom) are 0.476 V/ms^{-2}, 0.766 V/ms^{-2}, and 1.829 V/ms^{-2}, respectively. When $R_L = 4\,kohm$ and $L = 40\,mm$, the peak voltages produced from the different test arrangements of Figure 3.2 (from top to bottom) are 0.163 V/ms^{-2}, 0.189 V/ms^{-2}, and 0.345 V/ms^{-2}, respectively.

3.4. Conclusions

This chapter has presented an experimental demonstration of the feasibility of the concept of cantilevered piezoelectric energy harvesters with dynamic magnifier (*CPEHDM*). The performance characteristics are validated against the predictions of a finite element model developed in Chapter 2. The obtained results illustrate the metrics of the *CPEHDM* in comparison with the conventional piezoelectric energy harvester (*CPEH*). Also, it is shown that the *CPEHDM* is a simple and effective means for enhancing the magnitude and spectral characteristics of the *CPEH*.

Chapter 4

4. Finite Element Modeling of Piezoelectric Vibration Energy Harvesting from Coupled Structural-Acoustic Systems

4.1. Introduction

This chapter deals with the finite element modeling of piezoelectric vibration energy harvesting from coupled structural-acoustic systems. The modeling is based on a generic variational formulation which utilizes as its unknown variables, the mechanical displacement, electric voltage, and fluid pressure. This formulation is used to analyze a two-dimensional energy harvesting system which is composed of a rigid acoustic cavity coupled, at one end, with a flexible bimorph piezoelectric energy harvester attached on a vibrating base structure. The other end of the cavity is subjected to a persistent harmonic pressure input excitation.

The previously proposed and validated idea of attaching a dynamic magnifier is used again to enhance the electric power harvested from the coupled structural-acoustic system. The presented model is then extended and applied to a more complex structural-acoustic system consisting of a plate-harvester coupled to a three-dimensional acoustic cavity.

In all this study, the cavity under consideration is assumed to be rigid, filled with a homogeneous, inviscid, and compressible fluid. Also, the piezoelectric energy harvester utilizes piezoelectric patches which are connected in series to a resistive electric load. The developed model is used to predict the coupled mechanical response, electric power, and fluid pressure output for excitations around the modal

frequencies. Numerical examples are presented to illustrate the behavior of the energy harvester at short-circuit (*SC*) and open-circuit (*OC*) resonant conditions. Conditions for extracting the maximum electric power output of the energy harvester are also presented.

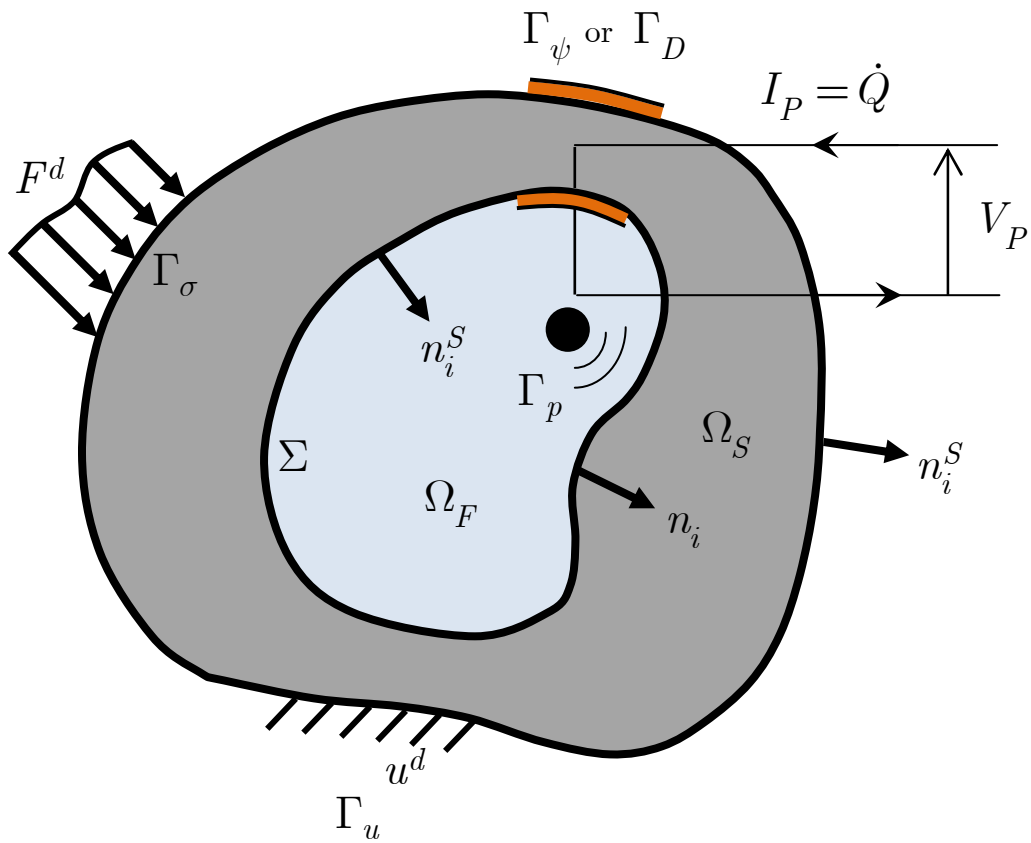

Figure 4.1: A general interior-fluid/piezoelectric-structure coupled problem

4.2. Theoretical Formulation

In this formulation, the domains occupying the piezoelectric-structure and the interior-fluid are denoted as Ω_S and Ω_F, respectively, and the interface between them by Σ. Figure 4.1 shows a typical coupled system of general geometry.

The mechanical boundary conditions constitute of the part Γ_u of the piezoelectric-structure exterior boundary that is subjected to a prescribed mechanical displacement u_i^d whereas the remaining part Γ_σ is that which corresponds to a prescribed force density F_i^d.

The electric boundary conditions constitute of the part Γ_ψ of the piezoelectric-structure exterior boundary that is subjected to a prescribed electric potential ψ^d whereas the remaining part Γ_D is that which corresponds to a prescribed electric charge density Q^d.

The fluid boundary conditions constitute of the part Γ_p of the interior-fluid exterior boundary that is subjected to a prescribed fluid pressure p^d whereas the remaining part Σ is that which defines the fluid-structure interface.

The local equations of the coupled problem are given by [37]

$$\sigma_{ij,j} = \rho_S \frac{\partial^2 u_i}{\partial t^2} \qquad \text{in } \Omega_S, \tag{4.1}$$

$$D_{i,i} = 0 \qquad \text{in } \Omega_S, \tag{4.2}$$

$$p_{,ii} = \frac{1}{c_F^2}\frac{\partial^2 p}{\partial t^2} \qquad \text{in } \Omega_F \tag{4.3}$$

Equations (4.1)-(4.3) are the well-known elastodynamic, electrostatic, and Helmholtz equations, respectively (subscript "i" can take x, y or z directions whereas "$,i$" denotes partial differentiation). These equations are supplemented by the following mechanical, electric, and fluid boundary conditions

$$\sigma_{ij} n_j^S = F_i^d \qquad \text{on } \Gamma_\sigma, \tag{4.4}$$

$$u_i = u_i^d \qquad \text{on } \Gamma_u, \tag{4.5}$$

$$\sigma_{ij} n_j^S = p n_i \qquad \text{on } \Sigma, \tag{4.6}$$

$$D_i n_i^S = -Q^d \qquad \text{on } \Gamma_D, \tag{4.7}$$

$$\psi = \psi^d \qquad \text{on } \Gamma_\psi, \tag{4.8}$$

$$p = p^d \qquad \text{on } \Gamma_p, \tag{4.9}$$

$$p_{,i} n_i = -\rho_F \frac{\partial^2 u_i}{\partial t^2} n_i \qquad \text{on } \Sigma \tag{4.10}$$

where σ_{ij} denote the stress tensor components, D_i denote the electric displacement vector components, p is the interior-fluid pressure, ρ_S is the structure mass density, ρ_F is the fluid mass density, and c_F is the speed of sound in the fluid. In addition, n_i^S is the unit normal external to Ω_S whereas n_i is the unit normal external to Ω_F. Moreover, in order to set a well-posed coupled problem, Equations (4.1)-(4.10) must be supplemented by appropriate initial conditions.

The constitutive equations of a piezoelectric-structure can be expressed as

$$\sigma_{ij} = c_{ijkl} \varepsilon_{kl} - e_{kij} E_k, \tag{4.11}$$

$$D_i = e_{ikl} \varepsilon_{kl} + \in_{ik} E_k \tag{4.12}$$

where ε_{kl} denote the strain tensor components, and E_k denote the electric field vector components. In addition, c_{ijkl}, e_{kij}, and $\in_{ik}$ denote, respectively, the elastic, piezoelectric, and dielectric material constants.

The strain tensor and the electric field are related to the mechanical displacement and electric potential, respectively, by the following gradient relations

$$\varepsilon_{kl} = \frac{1}{2}\left(u_{k,l} + u_{l,k}\right), \tag{4.13}$$

$$E_k = -\psi_{,k} \tag{4.14}$$

It can be seen from Equations (4.1)-(4.10) that the unknown variables of the coupled problem are chosen as the mechanical displacement u_i, electric potential ψ, and fluid pressure p.

Multiplying Equation (4.1) by δu_i, Equation (4.2) by $\delta\psi$, Equation (4.3) by δp, then applying Green's formula, and utilizing the boundary conditions (Equations (4.4)-(4.10)) and constitutive equations (Equations (4.11)-(4.12)), leads to the following generic representation of the variational equations

$$\int_{\Omega_S} c_{ijkl}\varepsilon_{kl}\delta\varepsilon_{ij}dv - \int_{\Omega_S} e_{kij}E_k\delta\varepsilon_{ij}dv + \rho_S\int_{\Omega_S}\frac{\partial^2 u_i}{\partial t^2}\delta u_i dv - \int_{\Sigma} pn_i\delta u_i ds = \int_{\Gamma_\sigma} F_i^d\delta u_i ds, \tag{4.15}$$

$$\int_{\Omega_S} e_{ikl}\varepsilon_{kl}\delta E_i dv + \int_{\Omega_S} \in_{ik} E_k\delta E_i dv = \int_{\Gamma_D} Q^d\delta\psi ds, \tag{4.16}$$

$$\frac{1}{\rho_F}\int_{\Omega_F} p_{,i}\delta p_{,i}dv + \frac{1}{\rho_F c_F^2}\int_{\Omega_F}\frac{\partial^2 p}{\partial t^2}\delta p dv + \int_{\Sigma}\frac{\partial^2 u_i}{\partial t^2}n_i\delta p ds = 0 \tag{4.17}$$

4.3. A Two-Dimensional Energy Harvesting System

The generalized variational equations (Equations (4.15)-(4.17)) are utilized to analyze a two-dimensional square cavity that is completely filled with air as shown in Figure 4.2(a). The cavity is assumed to be rigid at its boundaries described by Σ_R, but flexible at its boundary described by Σ. Moreover, a persistent harmonic pressure input excitation is applied at the end of the cavity described by Γ_p.

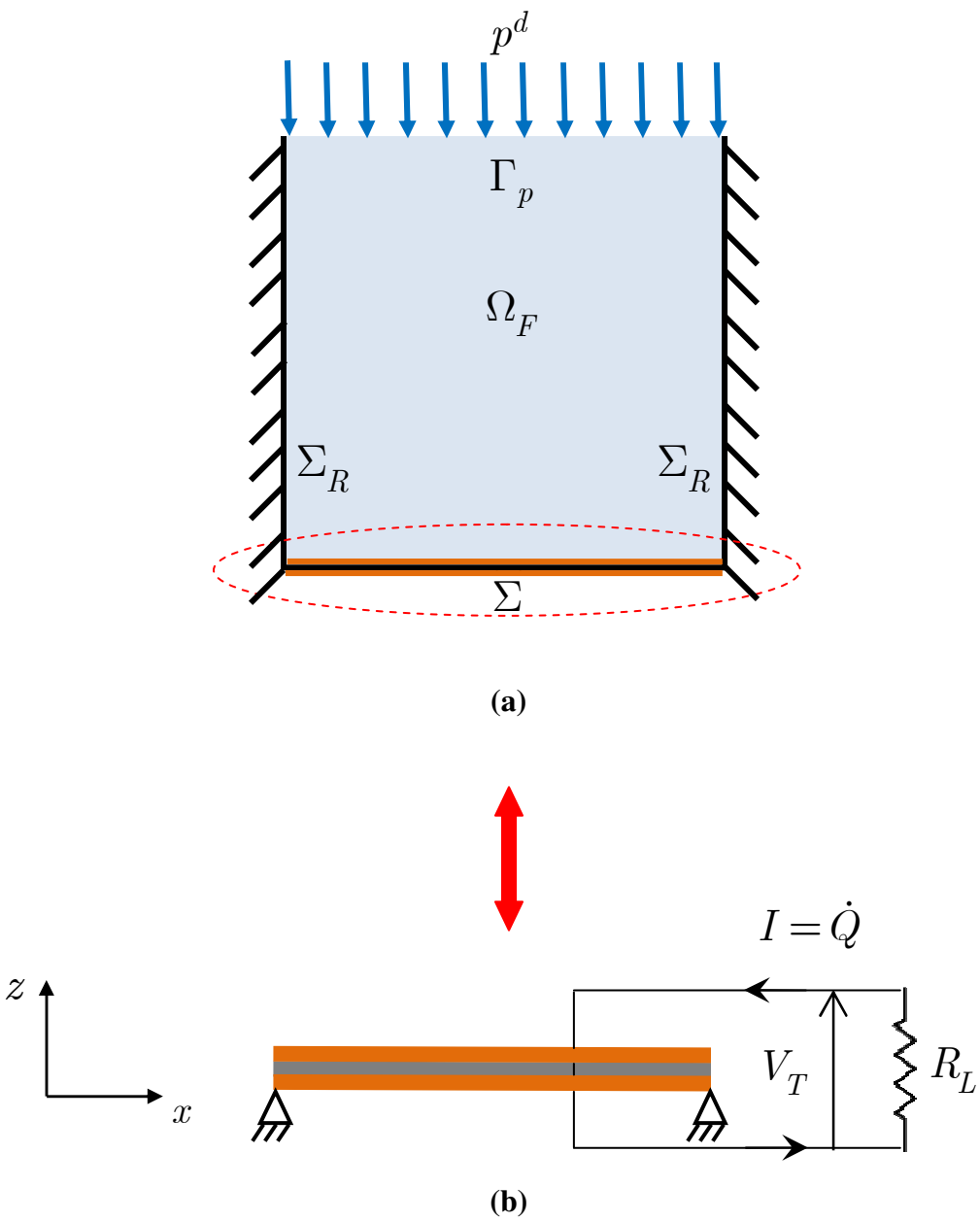

Figure 4.2: The two-dimensional coupled system: (a) square cavity filled with air, (b) bimorph energy harvester with series connection of piezoelectric patches

The continually vibrating flexible end of the cavity is made of a bimorph piezoelectric energy harvester attached to an isotropic base structure. For simplicity, the slender composite structure is assumed to be in a state of plane-stress and is modeled using the Euler-Bernoulli beam assumptions.

The two piezoelectric patches are fully covered with continuous electrodes of negligible thickness at their top and bottom surfaces, polarized in their transverse directions opposite to each other, and connected in series to a resistive electric load R_L which together with their internal capacitance form an electric circuit that is suitable for energy harvesting purposes [10]. The electric potential in the piezoelectric patches is assumed to be varying linearly in the z-direction (across their thickness) but considered uniform along the x and y coordinates. The fluid pressure inside the cavity is assumed to be varying spatially along the x and z coordinates but considered uniform in the y-direction (along the width of the composite beam).

Based on the above assumptions, the reduced piezoelectric-structure constitutive equations can be simplified in matrix-form as

$$\begin{Bmatrix} \sigma_1 \\ D_3 \end{Bmatrix} = \begin{bmatrix} \bar{c}_{11}^E & -\bar{e}_{31} \\ \bar{e}_{31} & \bar{\epsilon}_{33}^{\varepsilon} \end{bmatrix} \begin{Bmatrix} \varepsilon_1 \\ E_3 \end{Bmatrix} \tag{4.18}$$

where the one-dimensional (1-D) plane-stress constants in Equation (4.18) can be obtained in terms of the three-dimensional (3-D) constants as [14]

$$\bar{c}_{11}^E = c_{11}^E - \frac{\left(c_{13}^E\right)^2}{c_{33}^E}, \quad \bar{e}_{31} = e_{31} - \frac{c_{13}^E}{c_{33}^E} e_{33}, \quad \text{and} \quad \bar{\epsilon}_{33}^{\varepsilon} = \epsilon_{33}^{\varepsilon} + \frac{e_{33}^2}{c_{33}^E} \tag{4.19}$$

Moreover, the longitudinal strain ε_1 and the transverse electric field E_3 are related to the transverse mechanical displacement u_3 and the electric potential ψ by

$$\varepsilon_1 = z \frac{\partial^2 u_3}{\partial x^2}, \tag{4.20}$$

$$E_3 = -\frac{\partial \psi}{\partial z} = -\frac{V_P}{h_P} \tag{4.21}$$

where V_P ($P = 1, 2$) denotes the voltage between the upper and lower electrodes of the Pth piezoelectric patch with thickness h_P.

4.4. Finite Element Discretization

The structure domain is discretized using one-dimensional two-node finite elements. Each node has two degrees of freedom which are the transverse mechanical displacement and its derivative (rotation). On the other hand, the fluid domain is discretized using quadrilateral four-node finite elements where the nodal pressure is the only degree of freedom. Hence, the structure element transverse mechanical displacement and the fluid element pressure can be expressed, respectively, in terms of their nodal values as

$$u_3^e = N_{1S} w_1 + N_{2S} \theta_1 + N_{3S} w_2 + N_{4S} \theta_2 = \mathbf{N}_S \mathbf{U}^e, \tag{4.22}$$

$$p^e = N_{1F} p_1 + N_{2F} p_2 + N_{3F} p_3 + N_{4F} p_4 = \mathbf{N}_F \mathbf{P}^e \tag{4.23}$$

where w_m and θ_m ($m = 1, 2$) denote the nodal transverse mechanical displacements and their corresponding rotations whereas p_n ($n = 1, 2, 3, 4$) denote the nodal pressure values. The shape functions N_r ($r = 1, 2, 3, 4$) and their corresponding matrices $\mathbf{N}$ are supplemented with additional subscripts ("S" or "F") to differentiate between structure and fluid domains. Equations (4.20)-(4.23) can be substituted into the variational equations (Equations (4.15)-(4.17)), and the electric potential ψ is replaced by the electric voltage V_P to obtain the mass, stiffness, and coupling matrices of the coupled energy harvesting system [37].

Introducing the global vectors $\mathbf{U}$, $\mathbf{V}$, and $\mathbf{P}$ of mechanical, electric, and fluid degrees of freedom, respectively, the following discretized variational equations of the coupled problem can be written in matrix-form

$$\begin{bmatrix} \mathbf{M}_{uu} & \mathbf{0} & \mathbf{0} \\ \mathbf{0} & \mathbf{0} & \mathbf{0} \\ \mathbf{C}_{up}^{T} & \mathbf{0} & \mathbf{M}_{pp} \end{bmatrix} \begin{Bmatrix} \ddot{\mathbf{U}} \\ \ddot{\mathbf{V}} \\ \ddot{\mathbf{P}} \end{Bmatrix} + \begin{bmatrix} \mathbf{K}_{uu} & \mathbf{C}_{uV} & -\mathbf{C}_{up} \\ \mathbf{C}_{uV}^{T} & -\mathbf{K}_{VV} & \mathbf{0} \\ \mathbf{0} & \mathbf{0} & \mathbf{K}_{pp} \end{bmatrix} \begin{Bmatrix} \mathbf{U} \\ \mathbf{V} \\ \mathbf{P} \end{Bmatrix} = \begin{Bmatrix} \mathbf{F} \\ -\mathbf{Q} \\ \mathbf{0} \end{Bmatrix} \tag{4.24}$$

where $\mathbf{M}_{uu}$ and $\mathbf{K}_{uu}$ are the mechanical mass and stiffness matrices, $\mathbf{M}_{pp}$ and $\mathbf{K}_{pp}$ are the fluid mass and stiffness matrices, $\mathbf{C}_{uV}$ is the electromechanical coupling matrix, $\mathbf{K}_{VV}$ is the electric stiffness matrix, and $\mathbf{C}_{up}$ is the fluid-structure coupling matrix. Moreover, $\mathbf{F}$ and $\mathbf{Q}$ denote the applied mechanical load and charge vectors, respectively.

In addition to the above matrix equation (Equation (4.24)), the electric circuit (see Figure 4.2) imposes one additional relation which results from the application of Kirchhoff's voltage law. This relation can be simply written as

$$V_T = -R_L \dot{Q} \tag{4.25}$$

where $V_T = V_1 + V_2$ is the voltage across the resistive electric load R_L.

Combining Equations (4.24)-(4.25), and noting that the piezoelectric patches are connected in series (i.e. $Q_1 = Q_2 = Q$), a more convenient form for energy harvesting applications can be obtained for the coupled problem as [13]

$$\begin{bmatrix} \hat{\mathbf{M}}_{uu} & \mathbf{0} & \mathbf{0} \\ \mathbf{0} & 0 & \mathbf{0} \\ \hat{\mathbf{C}}_{up}^{T} & \mathbf{0} & \hat{\mathbf{M}}_{pp} \end{bmatrix} \begin{Bmatrix} \ddot{\mathbf{U}} \\ \ddot{Q} \\ \ddot{\mathbf{P}} \end{Bmatrix} + \begin{bmatrix} \hat{\mathbf{D}}_{uu} & \mathbf{0} & \mathbf{0} \\ \mathbf{0} & R_L & \mathbf{0} \\ \mathbf{0} & \mathbf{0} & \hat{\mathbf{D}}_{pp} \end{bmatrix} \begin{Bmatrix} \dot{\mathbf{U}} \\ \dot{Q} \\ \dot{\mathbf{P}} \end{Bmatrix}$$
$$+ \begin{bmatrix} \hat{\mathbf{K}}_{uu} & \hat{\mathbf{C}}_{uV} & -\hat{\mathbf{C}}_{up} \\ \hat{\mathbf{C}}_{uV}^{T} & 2/C_P & \mathbf{0} \\ \mathbf{0} & \mathbf{0} & \hat{\mathbf{K}}_{pp} \end{bmatrix} \begin{Bmatrix} \mathbf{U} \\ Q \\ \mathbf{P} \end{Bmatrix} = \begin{Bmatrix} \mathbf{F} \\ 0 \\ \mathbf{0} \end{Bmatrix} \tag{4.26}$$

where

$$\hat{\mathbf{M}}_{uu} = \mathbf{M}_{uu}, \qquad \hat{\mathbf{M}}_{pp} = \mathbf{M}_{pp}, \tag{4.27}$$

$$\hat{\mathbf{K}}_{uu} = \mathbf{K}_{uu} + \frac{\sum_{j=1}^{2} \mathbf{C}_j \mathbf{C}_j^T}{C_P}, \qquad \hat{\mathbf{K}}_{pp} = \mathbf{K}_{pp}, \tag{4.28}$$

$$\hat{\mathbf{C}}_{up} = \mathbf{C}_{up}, \qquad \hat{\mathbf{C}}_{uV} = \frac{\sum_{j=1}^{2} \mathbf{C}_j}{C_P} \tag{4.29}$$

It should be noted that $\mathbf{C}_1$ and $\mathbf{C}_2$ in Equations (4.28)-(4.29) are the submatrices which constitute the electromechanical coupling matrix $\mathbf{C}_{uV}$. Moreover, the matrices $\hat{\mathbf{D}}_{uu}$ and $\hat{\mathbf{D}}_{pp}$ have been added in Equation (4.26) in order to account for structure and fluid damping which are essential components for the accuracy of subsequent energy harvesting results.

The internal capacitance C_P ($P = 1, 2$) of each piezoelectric patch is

$$C_P = \frac{\bar{\epsilon}_{33}^{\varepsilon}\, bL_P}{h_P} \tag{4.30}$$

where b and L_P are the width and length of the Pth piezoelectric patch, respectively.

Since the cavity end described by Γ_p is subjected to persistent harmonic pressure excitations, the vector of nodal pressures can be decomposed into the subvectors: $\mathbf{P}^d$ of prescribed pressure values, and $\mathbf{P}$ of unknown pressure values [35]. Hence, Equation (4.26) can be rearranged to get

$$\mathbf{M}_c\ddot{\mathbf{X}}_{\mathrm{T}} + \mathbf{D}_c\dot{\mathbf{X}}_{\mathrm{T}} + \mathbf{K}_c\mathbf{X}_{\mathrm{T}} = \mathbf{F}_{\mathrm{T}} \tag{4.31}$$

where

$$\mathbf{X}_{\mathrm{T}} = \begin{Bmatrix} \mathbf{U} \\ Q \\ \mathbf{P} \\ \mathbf{P}^d \end{Bmatrix}, \qquad \mathbf{F}_{\mathrm{T}} = \begin{Bmatrix} \mathbf{F} \\ 0 \\ \mathbf{0} \\ \mathbf{0} \end{Bmatrix}, \qquad \mathbf{M}_c = \begin{bmatrix} \hat{\mathbf{M}}_{uu} & \mathbf{0} & \mathbf{0} & \mathbf{0} \\ \mathbf{0} & 0 & \mathbf{0} & \mathbf{0} \\ \hat{\mathbf{C}}_{up}^T & \mathbf{0} & \hat{\mathbf{M}}_{pp} & \hat{\mathbf{M}}_{p\bar{p}} \\ \hat{\mathbf{C}}_{u\bar{p}}^T & \mathbf{0} & \hat{\mathbf{M}}_{\bar{p}p} & \hat{\mathbf{M}}_{\bar{p}\bar{p}} \end{bmatrix},$$

$$\mathbf{D}_c = \begin{bmatrix} \hat{\mathbf{D}}_{uu} & \mathbf{0} & \mathbf{0} & \mathbf{0} \\ \mathbf{0} & R_L & \mathbf{0} & \mathbf{0} \\ \mathbf{0} & \mathbf{0} & \hat{\mathbf{D}}_{pp} & \mathbf{0} \\ \mathbf{0} & \mathbf{0} & \mathbf{0} & \mathbf{0} \end{bmatrix}, \qquad \mathbf{K}_c = \begin{bmatrix} \hat{\mathbf{K}}_{uu} & \hat{\mathbf{C}}_{uV} & -\hat{\mathbf{C}}_{up} & -\hat{\mathbf{C}}_{u\bar{p}} \\ \hat{\mathbf{C}}_{uV}^T & 2/C_P & \mathbf{0} & \mathbf{0} \\ \mathbf{0} & \mathbf{0} & \hat{\mathbf{K}}_{pp} & \hat{\mathbf{K}}_{p\bar{p}} \\ \mathbf{0} & \mathbf{0} & \hat{\mathbf{K}}_{\bar{p}p} & \hat{\mathbf{K}}_{\bar{p}\bar{p}} \end{bmatrix} \tag{4.32}$$

Eliminating the last row and moving the vector of prescribed pressure values $\mathbf{P}^d$ to the right hand side of Equation (4.31) yields

$$\begin{bmatrix} \hat{\mathbf{M}}_{uu} & \mathbf{0} & \mathbf{0} \\ \mathbf{0} & 0 & \mathbf{0} \\ \hat{\mathbf{C}}_{up}^T & \mathbf{0} & \hat{\mathbf{M}}_{pp} \end{bmatrix} \begin{Bmatrix} \ddot{\mathbf{U}} \\ \ddot{Q} \\ \ddot{\mathbf{P}} \end{Bmatrix} + \begin{bmatrix} \hat{\mathbf{D}}_{uu} & \mathbf{0} & \mathbf{0} \\ \mathbf{0} & R_L & \mathbf{0} \\ \mathbf{0} & \mathbf{0} & \hat{\mathbf{D}}_{pp} \end{bmatrix} \begin{Bmatrix} \dot{\mathbf{U}} \\ \dot{Q} \\ \dot{\mathbf{P}} \end{Bmatrix}$$
$$+ \begin{bmatrix} \hat{\mathbf{K}}_{uu} & \hat{\mathbf{C}}_{uV} & -\hat{\mathbf{C}}_{up} \\ \hat{\mathbf{C}}_{uV}^T & 2/C_P & \mathbf{0} \\ \mathbf{0} & \mathbf{0} & \hat{\mathbf{K}}_{pp} \end{bmatrix} \begin{Bmatrix} \mathbf{U} \\ Q \\ \mathbf{P} \end{Bmatrix} = \begin{Bmatrix} \mathbf{F}_u \\ 0 \\ \mathbf{F}_p \end{Bmatrix} \tag{4.33}$$

where $\mathbf{F}_u$ and $\mathbf{F}_p$ are given by

$$\mathbf{F}_u = \mathbf{F} + \hat{\mathbf{C}}_{u\bar{p}}\mathbf{P}^d, \tag{4.34}$$

$$\mathbf{F}_p = -\hat{\mathbf{M}}_{p\bar{p}}\ddot{\mathbf{P}}^d - \hat{\mathbf{K}}_{p\bar{p}}\mathbf{P}^d \tag{4.35}$$

Introducing the transformations $\mathbf{U} = \mathbf{\Phi}_u \mathbf{h}_u$ and $\mathbf{P} = \mathbf{\Phi}_p \mathbf{h}_p$ into Equations (4.33)-(4.35), and premultiplying the first and third rows of Equation (4.33) by $\mathbf{\Phi}_u^T$ and $\mathbf{\Phi}_p^T$, respectively, yields

$$\begin{bmatrix} \bar{\mathbf{M}}_{uu} & \mathbf{0} & \mathbf{0} \\ \mathbf{0} & 0 & \mathbf{0} \\ \bar{\mathbf{C}}_{up}^T & \mathbf{0} & \bar{\mathbf{M}}_{pp} \end{bmatrix} \begin{Bmatrix} \ddot{\mathbf{h}}_u \\ \ddot{Q} \\ \ddot{\mathbf{h}}_p \end{Bmatrix} + \begin{bmatrix} \bar{\mathbf{D}}_{uu} & \mathbf{0} & \mathbf{0} \\ \mathbf{0} & R_L & \mathbf{0} \\ \mathbf{0} & \mathbf{0} & \bar{\mathbf{D}}_{pp} \end{bmatrix} \begin{Bmatrix} \dot{\mathbf{h}}_u \\ \dot{Q} \\ \dot{\mathbf{h}}_p \end{Bmatrix}$$
$$+ \begin{bmatrix} \bar{\mathbf{K}}_{uu} & \bar{\mathbf{C}}_{uV} & -\bar{\mathbf{C}}_{up} \\ \bar{\mathbf{C}}_{uV}^T & 2/C_P & \mathbf{0} \\ \mathbf{0} & \mathbf{0} & \bar{\mathbf{K}}_{pp} \end{bmatrix} \begin{Bmatrix} \mathbf{h}_u \\ Q \\ \mathbf{h}_p \end{Bmatrix} = \begin{Bmatrix} \bar{\mathbf{F}}_u \\ 0 \\ \bar{\mathbf{F}}_p \end{Bmatrix} \tag{4.36}$$

where $\mathbf{\Phi}_u$ and $\mathbf{\Phi}_p$ are the mass normalized modal matrices associated with the structure (in *SC* conditions) and fluid (with open cavity), respectively, $\mathbf{h}_u$ and $\mathbf{h}_p$ are their corresponding vectors of modal coordinates.

The different mass normalized vectors and matrices given in Equation (4.36) can be expressed in terms of those in Equation (4.33) as

$$\bar{\mathbf{M}}_{uu} = \mathbf{\Phi}_u^T \hat{\mathbf{M}}_{uu} \mathbf{\Phi}_u, \qquad \bar{\mathbf{M}}_{uu} = \mathbf{\Phi}_p^T \hat{\mathbf{M}}_{pp} \mathbf{\Phi}_p, \tag{4.37}$$

$$\bar{\mathbf{K}}_{uu} = \mathbf{\Phi}_u^T \hat{\mathbf{K}}_{uu} \mathbf{\Phi}_u, \qquad \bar{\mathbf{K}}_{pp} = \mathbf{\Phi}_p^T \hat{\mathbf{K}}_{pp} \mathbf{\Phi}_p, \tag{4.38}$$

$$\bar{\mathbf{C}}_{uV} = \mathbf{\Phi}_u^T \hat{\mathbf{C}}_{uV}, \qquad \bar{\mathbf{C}}_{up} = \mathbf{\Phi}_u^T \hat{\mathbf{C}}_{up} \mathbf{\Phi}_p, \tag{4.39}$$

$$\bar{\mathbf{F}}_u = \mathbf{\Phi}_u^T \mathbf{F}_u, \qquad \bar{\mathbf{F}}_p = \mathbf{\Phi}_p^T \mathbf{F}_p \tag{4.40}$$

For a harmonic input pressure excitation at a frequency ω such that $\mathbf{P}^d = \mathbf{P}_0^d e^{j\omega t}$, $\bar{\mathbf{F}}_u = \bar{\mathbf{F}}_{0u} e^{j\omega t}$, and $\bar{\mathbf{F}}_p = \bar{\mathbf{F}}_{0p} e^{j\omega t}$, the output solution is assumed also in harmonic form as

$$\mathbf{h}_u = \mathbf{H}_{0u} e^{j\omega t}, \quad \mathbf{h}_p = \mathbf{H}_{0p} e^{j\omega t}, \quad Q = Q_0 e^{j\omega t} \tag{4.41}$$

Defining the structure and fluid impedance matrices, respectively, as $\bar{\mathbf{Z}}_u = \bar{\mathbf{K}}_{uu} + j\omega\bar{\mathbf{D}}_{uu} - \omega^2\bar{\mathbf{M}}_{uu}$ and $\bar{\mathbf{Z}}_p = \bar{\mathbf{K}}_{pp} + j\omega\bar{\mathbf{D}}_{pp} - \omega^2\bar{\mathbf{M}}_{pp}$, substituting Equation (4.41) into Equation (4.36), and carrying out some manipulations, we arrive at the following relations for the output modal amplitudes

$$Q_0 = \frac{\bar{\mathbf{C}}_{uV}^T \mathbf{\Theta}^{-1}\left(\bar{\mathbf{F}}_{0u} + \bar{\mathbf{C}}_{up}\bar{\mathbf{Z}}_p^{-1}\bar{\mathbf{F}}_{0p}\right)}{\bar{\mathbf{C}}_{uV}^T \mathbf{\Theta}^{-1}\bar{\mathbf{C}}_{uV} - j\omega R_L - 2/C_P}, \tag{4.42}$$

$$\mathbf{H}_{0u} = \mathbf{\Theta}^{-1}\left(\bar{\mathbf{F}}_{0u} + \bar{\mathbf{C}}_{up}\bar{\mathbf{Z}}_p^{-1}\bar{\mathbf{F}}_{0p} - \bar{\mathbf{C}}_{uV} Q_0\right), \tag{4.43}$$

$$\mathbf{H}_{0p} = \bar{\mathbf{Z}}_p^{-1}\left(\bar{\mathbf{F}}_{0p} + \omega^2\bar{\mathbf{C}}_{up}^T\mathbf{H}_{0u}\right) \tag{4.44}$$

where the matrix $\mathbf{\Theta}$ is given by

$$\mathbf{\Theta} = \left(\bar{\mathbf{Z}}_u - \omega^2\bar{\mathbf{C}}_{up}\bar{\mathbf{Z}}_p^{-1}\bar{\mathbf{C}}_{up}^T\right) \tag{4.45}$$

4.5. Structure and Fluid Damping

The proposed model must take into account the different damping mechanisms that can affect the accuracy of subsequent desirable results from the coupled energy harvesting system. In fact, each of the piezoelectric-structure and the interior-fluid contribute its own damping to the total system where each coupled-mode is associated with a specific damping factor. Here, the piezoelectric-structure and the interior-fluid can be analyzed independently because of the mass normalization procedure used in Equation (4.36) to simplify the analysis.

For the structure, two types of mechanical damping are considered. The first is referred to as the viscous air damping whereas the second is known as the strain rate damping due to structural viscoelasticity [10]. The mechanical damping ratio ζ_r of

the rth structure mode of vibration which includes the effect of both viscous air damping and strain rate damping is given by

$$\zeta_r = \zeta_r^a + \zeta_r^s = \frac{c_a}{2m\omega_r} + \frac{c_s I_t \omega_r}{2E_t I_t} \tag{4.46}$$

where ζ_r^a is the viscous air damping component of the damping ratio, ζ_r^s is the strain rate damping component of the damping ratio, c_a is the viscous air damping coefficient, $c_s I_t$ is the equivalent damping term of the cross section due to structural viscoelasticity, and ω_r is the rth natural frequency of the composite beam under *SC* conditions. Experimental modal analysis under *SC* conditions is required to determine any two modal damping ratios so as to calculate c_a and $c_s I_t$ using Equation (4.46). Once these proportionality constants are known, Equation (4.46) can be used again to find the rest of the modal damping ratios.

For the fluid, a proportional damping is used where the fluid damping matrix is composed of a weighted sum of the fluid mass and stiffness matrices expressed as

$$\bar{\mathbf{D}}_{pp} = \alpha \bar{\mathbf{M}}_{pp} + \beta \bar{\mathbf{K}}_{pp} \tag{4.47}$$

where α and β are the constants of proportionality. Again, experimental modal analysis is needed to determine these constants for a square rigid cavity which is open from one of its four sides.

4.6. Numerical Results

This section presents some numerical results of the proposed finite element model. Table 4.1 lists the geometric, structure, fluid, and electromechanical

parameters of the coupled problem. Note that the piezoelectric material used here is PZT-5A.

Table 4.1: Geometric, structure, fluid, and electromechanical properties of the coupled system

Geometric Properties	Value
Length of substructure L_S and each piezoelectric patch L_P	200 mm
Width of substructure b_S and each piezoelectric patch b_P	30 mm
Thickness of substructure h_S	0.4 mm
Thickness of each piezoelectric patch h_P	0.8 mm
Size of square cavity $L_X \times L_Y$	200 $mm \times 200$ mm
Structure Properties	**Value**
Young's Modulus of substructure c_{11}^S	100 GPa
Young's Modulus of each piezoelectric patch c_{11}^E	120.3 GPa
Young's Modulus of each piezoelectric patch c_{13}^E	75.1 GPa
Young's Modulus of each piezoelectric patch c_{33}^E	110.9 GPa
Mass density of substructure ρ_S	7165 kg/m^3
Mass density of each piezoelectric patch ρ_P	7800 kg/m^3
Fluid and Electromechanical Properties	**Value**
Mass density of air ρ_F	1.2 kg/m^3
Piezoelectric constant e_{31}	-5.2 C/m^2
Piezoelectric constant e_{33}	15.9 C/m^2
Permittivity $\in_{33}^{\varepsilon}$ *	$1800 \times \in_0$ pF/m
Speed of sound for air c_F	340 m/s

* Permittivity of free space $\in_0 = 8.854\ pF/m$

Table 4.2 lists the first six natural frequencies of the composite beam alone when the piezoelectric patches are in *SC* and *OC* electric boundary conditions. Figure 4.3 shows the corresponding mode shapes of the composite beam alone.

Table 4.2: First six natural frequencies (*Hz*) of the composite beam alone

MODE	SHORT-CIRCUIT	OPEN-CIRCUIT
1	68.33	72.83
2	273.31	273.31
3	614.97	619.68
4	1093.36	1093.36
5	1708.63	1713.38
6	2461.10	2461.10

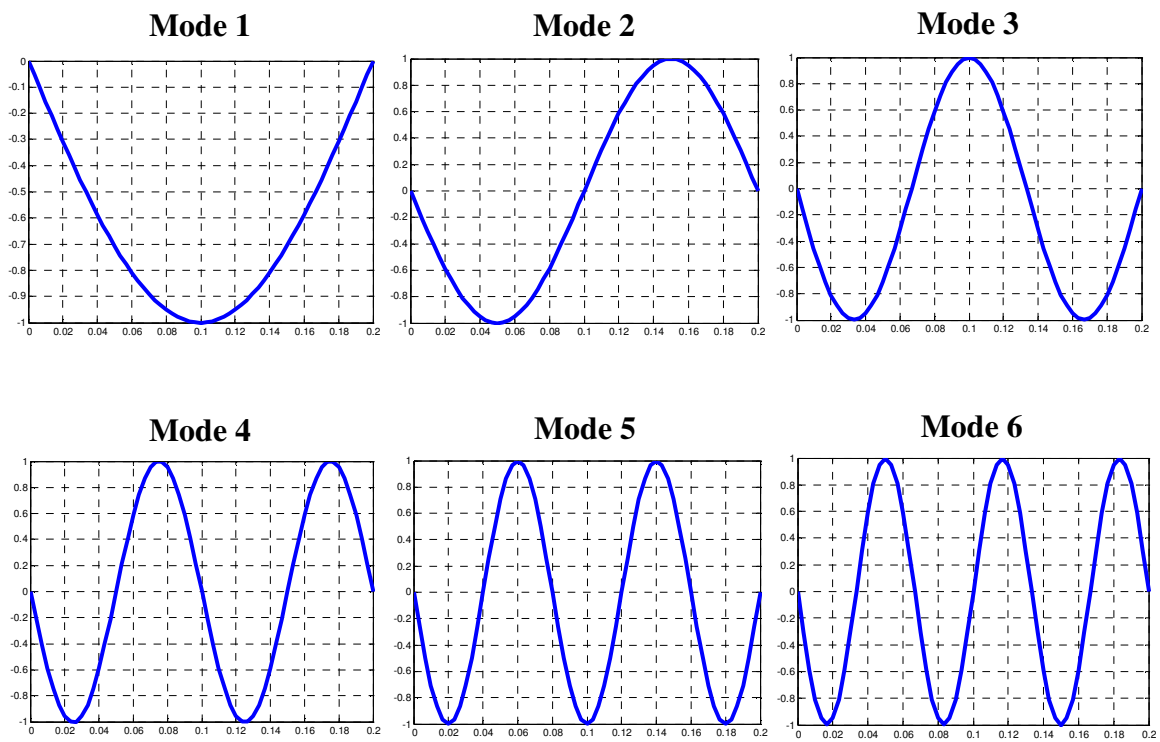

Figure 4.3: First six mode shapes of the composite beam alone

Table 4.3 lists the first six natural frequencies of the cavity alone for all-rigid and one-side open fluid boundary conditions. Figure 4.4 and Figure 4.5 show the corresponding mode shapes of the cavity alone.

Table 4.3: First six natural frequencies (*Hz*) of the cavity alone

MODE	ALL-RIGID	ONE-SIDE OPEN
1	850.87	425.11
2	850.87	951.16
3	1203.32	1277.95
4	1706.70	1535.30
5	1706.70	1759.14
6	1907.31	2132.37

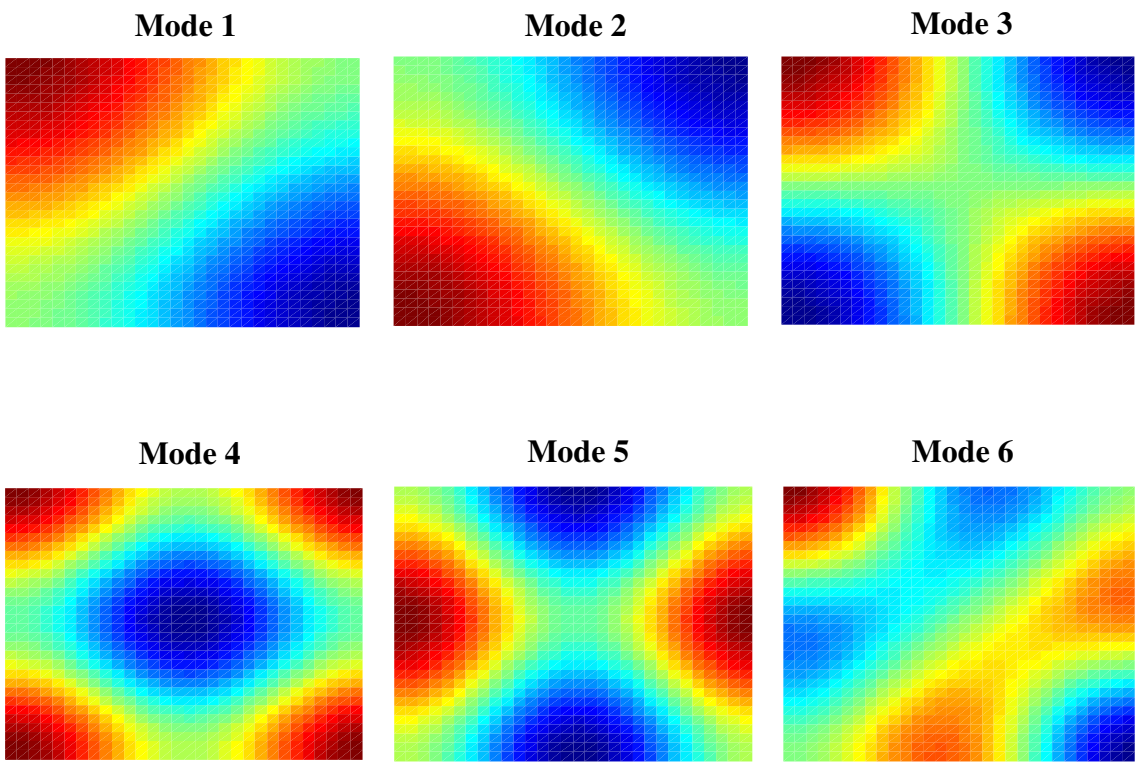

Figure 4.4: First six mode shapes of the rigid cavity alone

Table 4.4 and Table 4.5 list the first six natural frequencies of the coupled system with rigid cavity and open cavity fluid boundary conditions when the piezoelectric patches are subjected to *SC* and *OC* electric boundary conditions, respectively. Figure 4.6 and Figure 4.7 show the corresponding mode shapes of the coupled system.

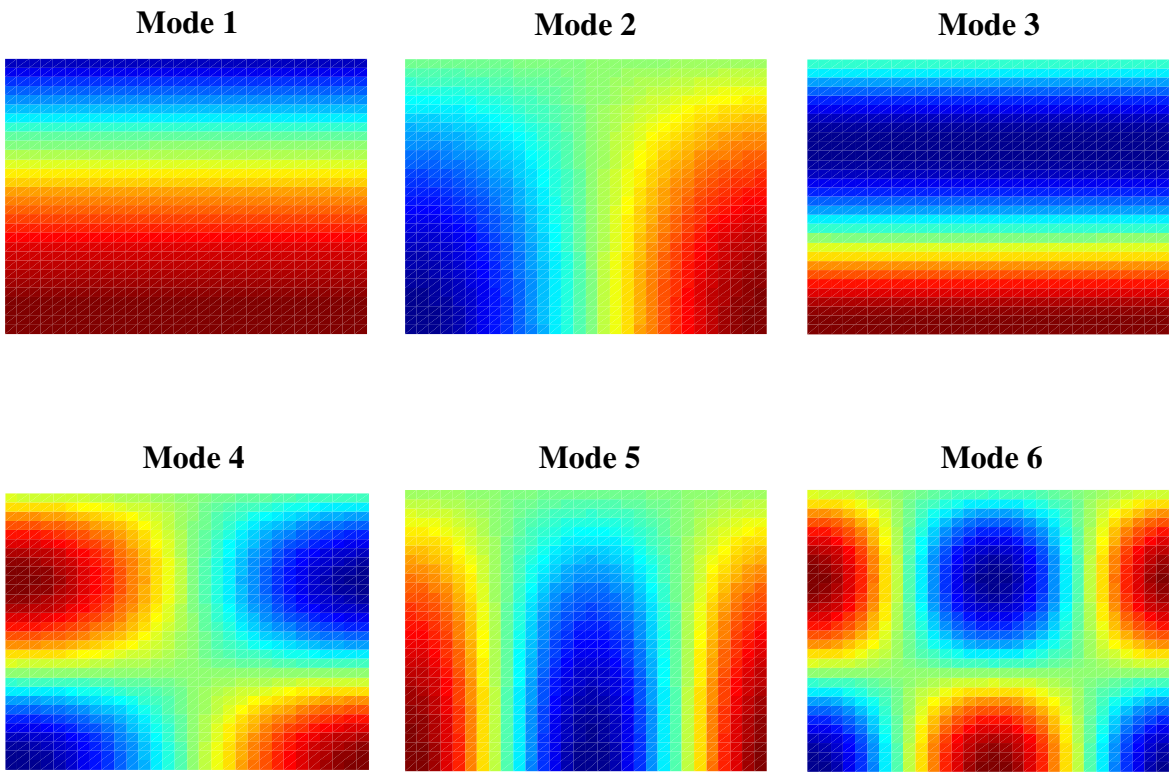

Figure 4.5: First six mode shapes of the one-side open cavity alone

Table 4.4: First six natural frequencies (*Hz*) of the coupled system for all-rigid fluid boundary condition

MODE	SHORT-CIRCUIT	OPEN-CIRCUIT
1	74.65	78.74
2	272.73	272.73
3	614.22	618.92
4	851.29	851.29
5	852.21	852.21
6	1092.10	1092.10

Table 4.5: First six natural frequencies (*Hz*) of the coupled system for one-side open fluid boundary condition

MODE	SHORT-CIRCUIT	OPEN-CIRCUIT
1	67.87	72.35
2	272.74	272.74
3	427.11	427.11
4	614.60	619.31
5	951.65	951.65
6	1092.92	1092.92

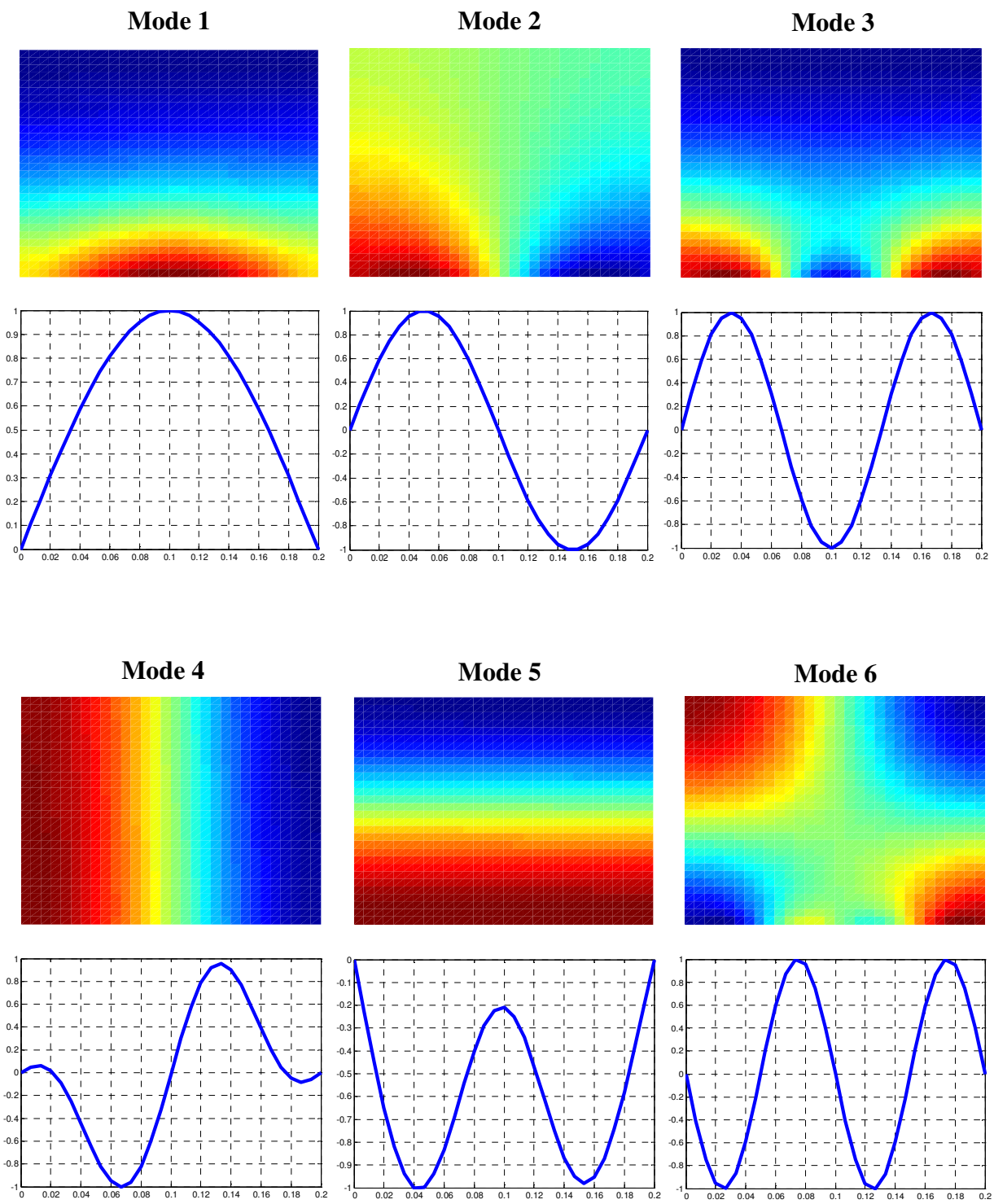

Figure 4.6: First six mode shapes of the coupled system with rigid cavity at the short-circuit condition

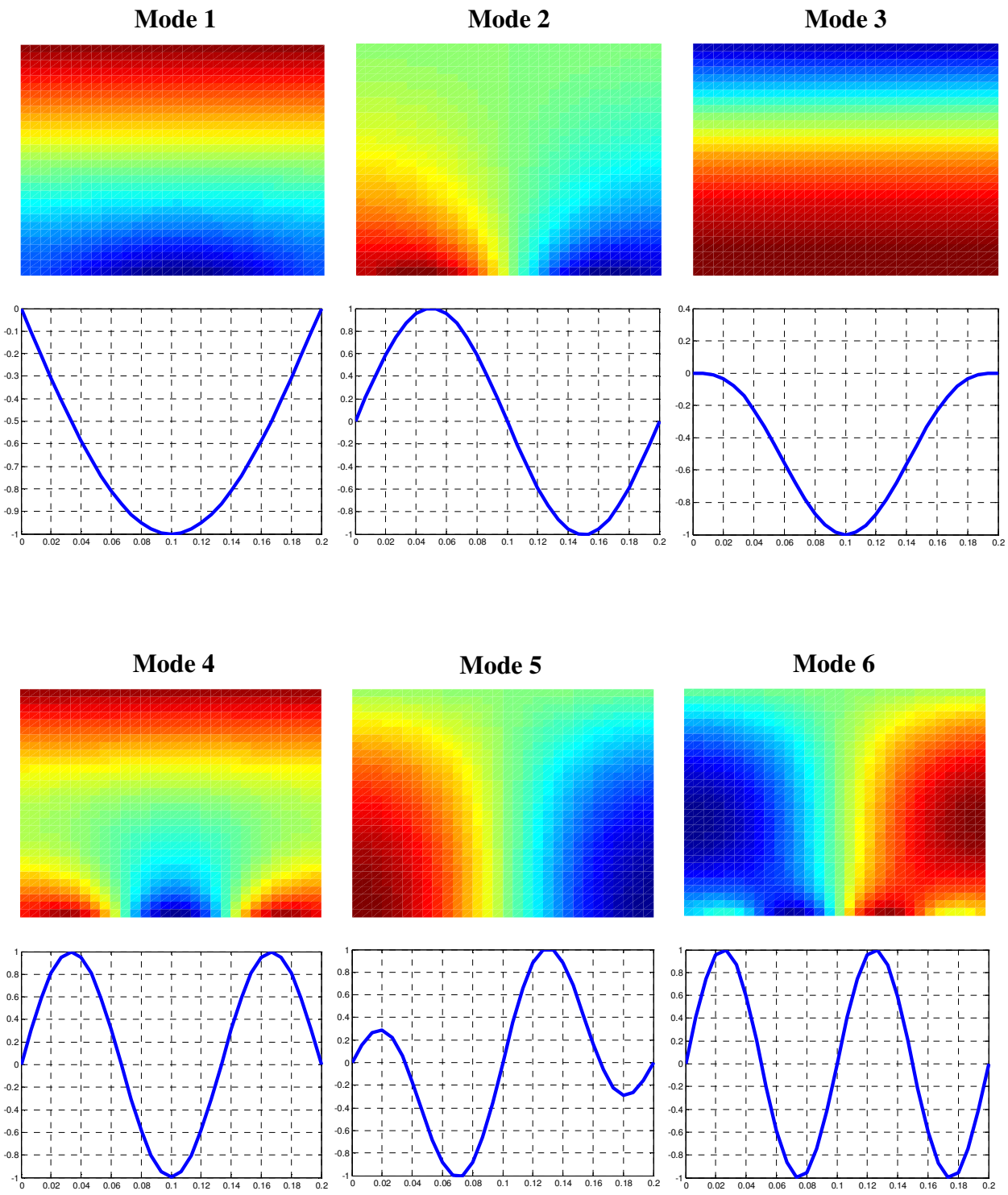

Figure 4.7: First six mode shapes of the coupled system with open cavity at the short-circuit condition

Figure 4.8, Figure 4.9, and Figure 4.10 show, respectively, the electric voltage, current, and power *FRF*s of the piezoelectric energy harvester for different resistive loads when $p^d = 1Pa$. It can be seen from the electric voltage *FRF* that the amplitude of the voltage increases with increasing the load resistance and that the behavior is monotonic. On the other hand, the electric current *FRF* shows that the amplitude of the current decreases with increasing the load resistance but the behavior is still monotonic. Since the electric power *FRF* is the product of the electric voltage and current *FRF*s, the behavior is not monotonic. Figure 4.11 shows the variation of the electric power amplitude with load resistance for excitations at the short-circuit and open-circuit resonant frequencies of the first coupled vibration mode.

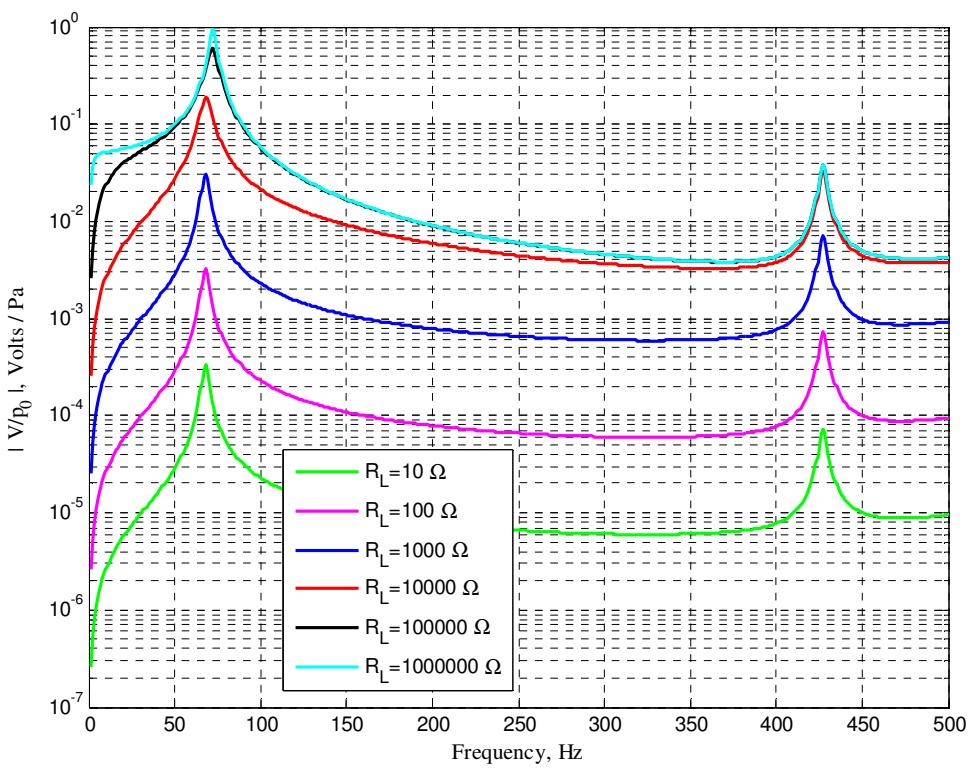

Figure 4.8: Voltage FRF of the piezoelectric energy harvester for different resistive loads

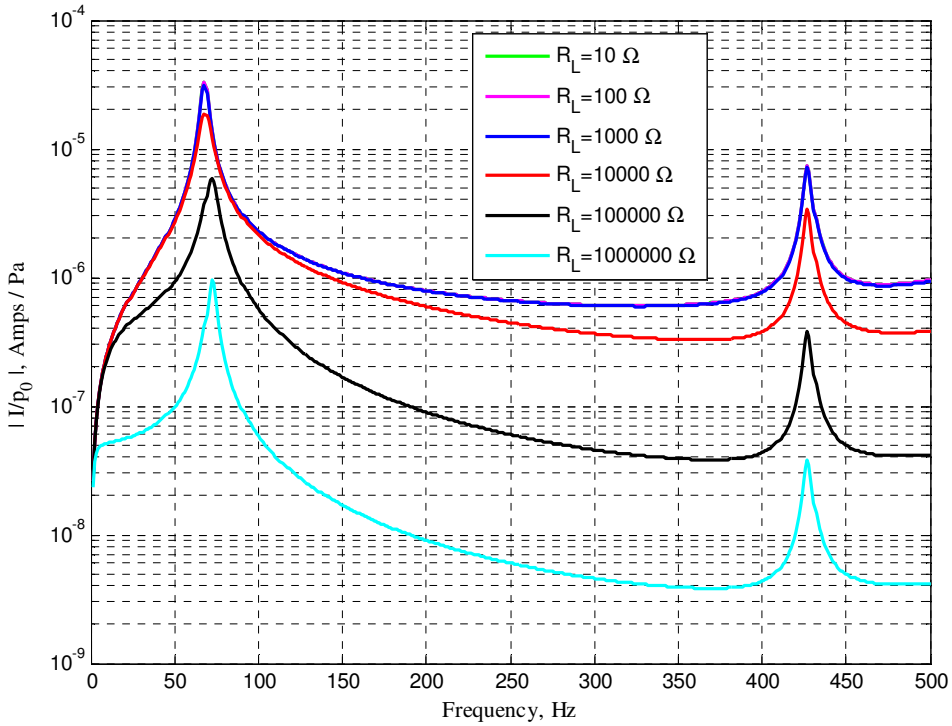

Figure 4.9: Current FRF of the piezoelectric energy harvester for different resistive loads

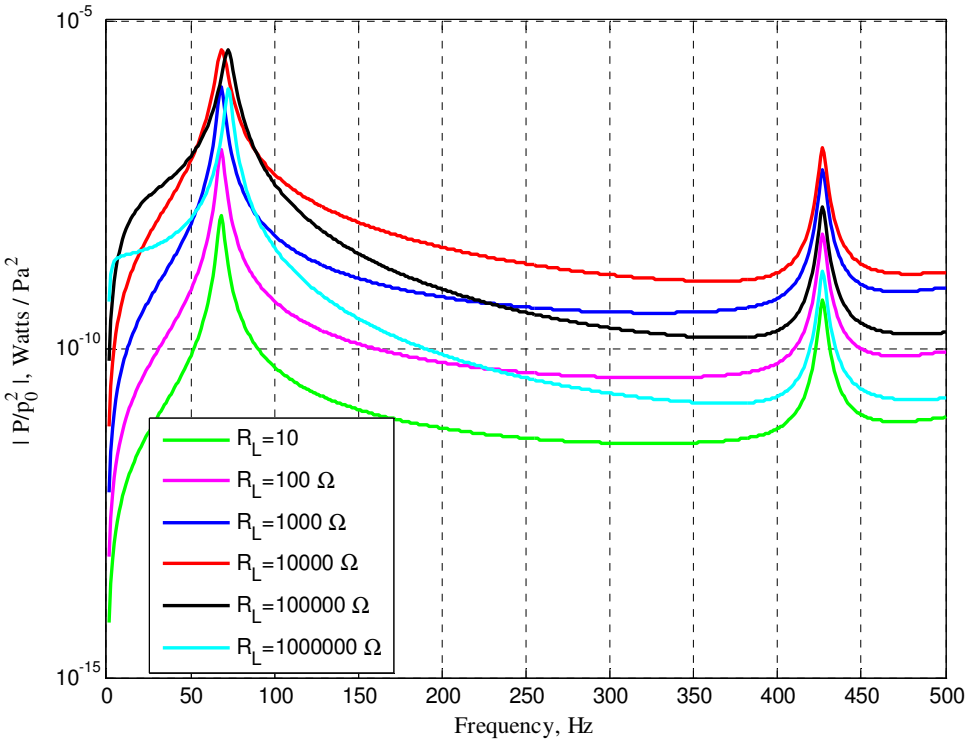

Figure 4.10: Power FRF of the piezoelectric energy harvester for different resistive loads

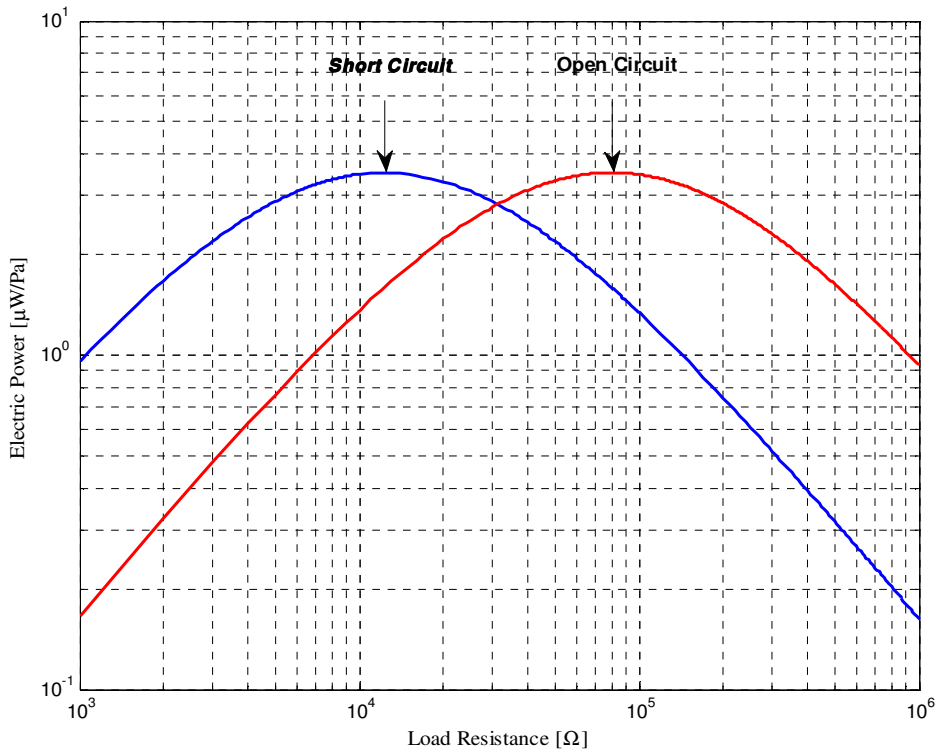

Figure 4.11: Variation of electric power with load resistance at the *SC* and *OC* resonant conditions of the first coupled vibration mode

From Figure 4.11, it is found that the optimal resistances at the short-circuit and open-circuit resonant conditions are $R_L^{SC} = 12\,k\Omega$ and $R_L^{OC} = 80\,k\Omega$, respectively. The corresponding output electric power for both cases is about $3.52\,\mu W / Pa$.

4.7. A Two-Dimensional Energy Harvester with a Dynamic Magnifier

The idea of attaching a dynamic magnifier to a structural system for enhancing the electric power output of piezoelectric energy harvesters was proposed and validated in Chapter 2. Here, we extend this idea for the modeling of structural-acoustic coupled systems. A modified version of Figure 4.2 where the coupled system is augmented with a dynamic magnifier is shown in Figure 4.12.

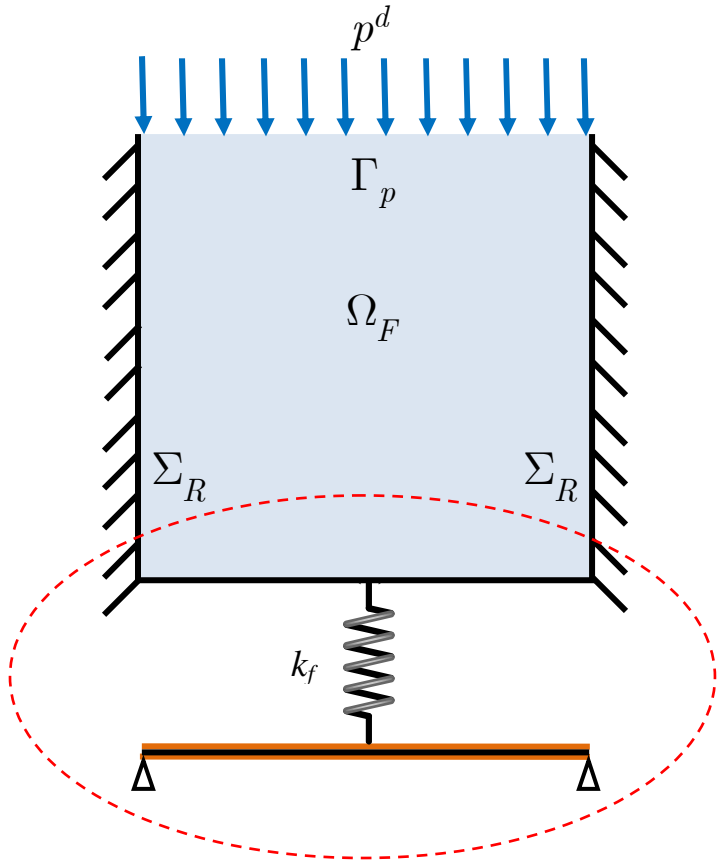

(a)

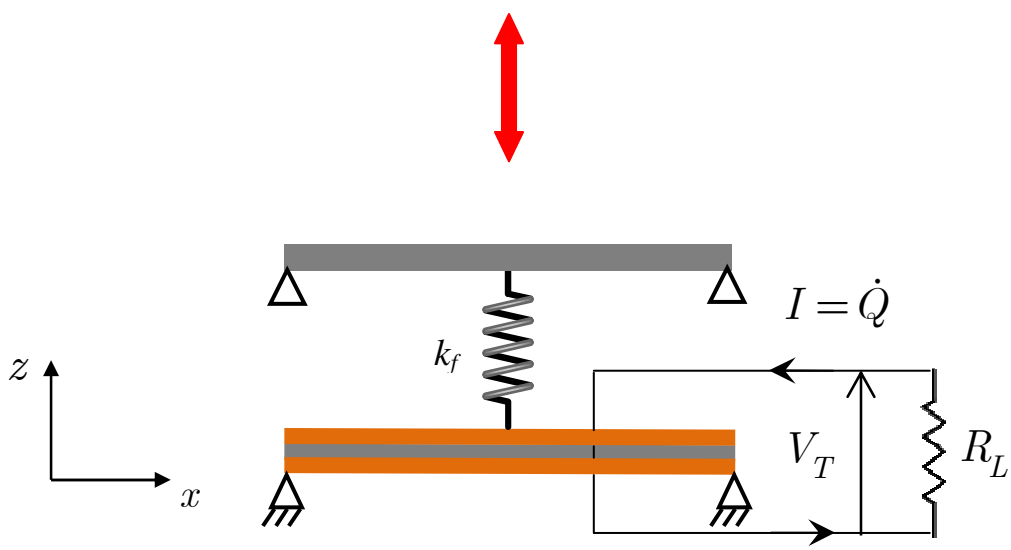

(b)

Figure 4.12: The two-dimensional coupled system with a dynamic magnifier: (a) square cavity filled with air, (b) bimorph energy harvester with series connection of piezoelectric patches and attached to a dynamic magnifier

In Figure 4.12, a dynamic magnifier consisting of a simply-supported beam and a discrete spring is attached to a bimorph piezoelectric energy harvester. The discrete spring connecting the two vibrating structures is located in the midpoint between them. For simplicity, the Euler-Bernoulli beam assumptions are used to model the dynamic magnifier as well as the piezoelectric energy harvester. The variational equations of the combined system are identical to Equations (4.15)-(4.17).

In order to formulate a finite element model for the combined system which takes into account the effect of the attached dynamic magnifier, we introduce the global vectors $\mathbf{U}^h$, $\mathbf{U}^f$, $\mathbf{V}$, and $\mathbf{P}$ of mechanical, electric, and fluid degrees of freedom (the superscript h in $\mathbf{U}^h$ denotes harvester, whereas the superscript f in $\mathbf{U}^f$ denotes magnifier). The following discretized variational equations of the combined system can be written in matrix-form

$$\begin{bmatrix} \mathbf{M}_{uu}^h & \mathbf{0} & \mathbf{0} & \mathbf{0} \\ \mathbf{0} & \mathbf{M}_{uu}^f & \mathbf{0} & \mathbf{0} \\ \mathbf{0} & \mathbf{0} & \mathbf{0} & \mathbf{0} \\ \mathbf{0} & \mathbf{C}_{up}^T & \mathbf{0} & \mathbf{M}_{pp} \end{bmatrix} \begin{Bmatrix} \ddot{\mathbf{U}}^h \\ \ddot{\mathbf{U}}^f \\ \ddot{\mathbf{V}} \\ \ddot{\mathbf{P}} \end{Bmatrix} + \begin{bmatrix} \mathbf{K}_{uu}^h & \mathbf{K}_s & \mathbf{C}_{uV} & \mathbf{0} \\ \mathbf{K}_s^T & \mathbf{K}_{uu}^f & \mathbf{0} & -\mathbf{C}_{up} \\ \mathbf{C}_{uV}^T & \mathbf{0} & -\mathbf{K}_{VV} & \mathbf{0} \\ \mathbf{0} & \mathbf{0} & \mathbf{0} & \mathbf{K}_{pp} \end{bmatrix} \begin{Bmatrix} \mathbf{U}^h \\ \mathbf{U}^f \\ \mathbf{V} \\ \mathbf{P} \end{Bmatrix} = \begin{Bmatrix} \mathbf{F}^h \\ \mathbf{F}^b \\ -\mathbf{Q} \\ \mathbf{0} \end{Bmatrix} \quad (4.48)$$

where $\mathbf{M}_{uu}^h$ and $\mathbf{K}_{uu}^h$ are the mechanical mass and stiffness matrices of the harvester, $\mathbf{M}_{uu}^f$ and $\mathbf{K}_{uu}^f$ are the mechanical mass and stiffness matrices of the magnifier, $\mathbf{M}_{pp}$ and $\mathbf{K}_{pp}$ are the fluid mass and stiffness matrices, $\mathbf{K}_s$ is the mechanical discrete spring matrix, $\mathbf{C}_{uV}$ is the electromechanical coupling matrix, $\mathbf{K}_{VV}$ is the electric stiffness matrix, and $\mathbf{C}_{up}$ is the fluid-structure coupling matrix. Moreover, $\mathbf{F}^h$, $\mathbf{F}^f$ and $\mathbf{Q}$ denote the applied mechanical load and charge vectors.

Knowing that the two piezoelectric patches are connected in series (*i.e.* $Q_1 = Q_2 = Q$), a more convenient form for energy harvesting applications can be obtained for the combined system as [13]

$$\begin{bmatrix} \hat{\mathbf{M}}_{uu}^{h} & \mathbf{0} & \mathbf{0} & \mathbf{0} \\ \mathbf{0} & \hat{\mathbf{M}}_{uu}^{f} & \mathbf{0} & \mathbf{0} \\ \mathbf{0} & \mathbf{0} & 0 & \mathbf{0} \\ \mathbf{0} & \hat{\mathbf{C}}_{up}^{T} & \mathbf{0} & \hat{\mathbf{M}}_{pp} \end{bmatrix} \begin{Bmatrix} \ddot{\mathbf{U}}^{h} \\ \ddot{\mathbf{U}}^{f} \\ \ddot{Q} \\ \ddot{\mathbf{P}} \end{Bmatrix} + \begin{bmatrix} \hat{\mathbf{D}}_{uu}^{h} & \mathbf{0} & \mathbf{0} & \mathbf{0} \\ \mathbf{0} & \hat{\mathbf{D}}_{uu}^{f} & \mathbf{0} & \mathbf{0} \\ \mathbf{0} & \mathbf{0} & R_L & \mathbf{0} \\ \mathbf{0} & \mathbf{0} & \mathbf{0} & \hat{\mathbf{D}}_{pp} \end{bmatrix} \begin{Bmatrix} \dot{\mathbf{U}}^{h} \\ \dot{\mathbf{U}}^{f} \\ \dot{Q} \\ \dot{\mathbf{P}} \end{Bmatrix}$$
$$+ \begin{bmatrix} \hat{\mathbf{K}}_{uu}^{h} & \hat{\mathbf{K}}_{s} & \hat{\mathbf{C}}_{uV} & \mathbf{0} \\ \hat{\mathbf{K}}_{s}^{T} & \hat{\mathbf{K}}_{uu}^{f} & \mathbf{0} & -\hat{\mathbf{C}}_{up} \\ \hat{\mathbf{C}}_{uV}^{T} & \mathbf{0} & 2/C_P & \mathbf{0} \\ \mathbf{0} & \mathbf{0} & \mathbf{0} & \hat{\mathbf{K}}_{pp} \end{bmatrix} \begin{Bmatrix} \mathbf{U}^{h} \\ \mathbf{U}^{f} \\ Q \\ \mathbf{P} \end{Bmatrix} = \begin{Bmatrix} \mathbf{F}^{h} \\ \mathbf{F}^{f} \\ 0 \\ \mathbf{0} \end{Bmatrix} \tag{4.49}$$

where

$$\hat{\mathbf{M}}_{uu}^{h} = \mathbf{M}_{uu}^{h}, \qquad \hat{\mathbf{M}}_{uu}^{f} = \mathbf{M}_{uu}^{f}, \qquad \hat{\mathbf{M}}_{pp} = \mathbf{M}_{pp}, \tag{4.50}$$

$$\hat{\mathbf{K}}_{uu}^{h} = \mathbf{K}_{uu}^{h} + \frac{\sum_{j=1}^{2} \mathbf{C}_j \mathbf{C}_j^T}{C_P}, \qquad \hat{\mathbf{K}}_{uu}^{f} = \mathbf{K}_{uu}^{f}, \qquad \hat{\mathbf{K}}_{pp} = \mathbf{K}_{pp}, \qquad \hat{\mathbf{K}}_{s} = \mathbf{K}_{s}, \tag{4.51}$$

$$\hat{\mathbf{C}}_{up} = \mathbf{C}_{up}, \qquad \hat{\mathbf{C}}_{uV} = \frac{\sum_{j=1}^{2} \mathbf{C}_j}{C_P} \tag{4.52}$$

Since the cavity end described by Γ_p is subjected to persistent harmonic pressure excitations, the vector of nodal pressures can be decomposed into the subvectors: $\mathbf{P}^d$ of prescribed pressure values, and $\mathbf{P}$ of unknown pressure values [35]. Hence, Equation (4.49) can be rearranged to get

$$\mathbf{M}_c \ddot{\mathbf{X}}_{\mathrm{T}} + \mathbf{D}_c \dot{\mathbf{X}}_{\mathrm{T}} + \mathbf{K}_c \mathbf{X}_{\mathrm{T}} = \mathbf{F}_{\mathrm{T}} \tag{4.53}$$

where

$$\mathbf{X}_{\mathrm{T}} = \begin{Bmatrix} \mathbf{U}^h \\ \mathbf{U}^f \\ Q \\ \mathbf{P} \\ \mathbf{P}^d \end{Bmatrix}, \qquad \mathbf{F}_{\mathrm{T}} = \begin{Bmatrix} \mathbf{F}^h \\ \mathbf{F}^f \\ 0 \\ \mathbf{0} \\ \mathbf{0} \end{Bmatrix}, \qquad \mathbf{M}_c = \begin{bmatrix} \hat{\mathbf{M}}^h_{uu} & \mathbf{0} & \mathbf{0} & \mathbf{0} & \mathbf{0} \\ \mathbf{0} & \hat{\mathbf{M}}^f_{uu} & \mathbf{0} & \mathbf{0} & \mathbf{0} \\ \mathbf{0} & \mathbf{0} & 0 & \mathbf{0} & \mathbf{0} \\ \mathbf{0} & \hat{\mathbf{C}}^T_{up} & \mathbf{0} & \hat{\mathbf{M}}_{pp} & \hat{\mathbf{M}}_{p\bar{p}} \\ \mathbf{0} & \hat{\mathbf{C}}^T_{u\bar{p}} & \mathbf{0} & \hat{\mathbf{M}}_{\bar{p}p} & \hat{\mathbf{M}}_{\bar{p}\bar{p}} \end{bmatrix}$$

$$\mathbf{D}_c = \begin{bmatrix} \hat{\mathbf{D}}^h_{uu} & \mathbf{0} & \mathbf{0} & \mathbf{0} & \mathbf{0} \\ \mathbf{0} & \hat{\mathbf{D}}^f_{uu} & \mathbf{0} & \mathbf{0} & \mathbf{0} \\ \mathbf{0} & \mathbf{0} & R_L & \mathbf{0} & \mathbf{0} \\ \mathbf{0} & \mathbf{0} & \mathbf{0} & \hat{\mathbf{D}}_{pp} & \mathbf{0} \\ \mathbf{0} & \mathbf{0} & \mathbf{0} & \mathbf{0} & \mathbf{0} \end{bmatrix}, \qquad \mathbf{K}_c = \begin{bmatrix} \hat{\mathbf{K}}^h_{uu} & \hat{\mathbf{K}}_s & \hat{\mathbf{C}}_{uV} & \mathbf{0} & \mathbf{0} \\ \hat{\mathbf{K}}^T_s & \hat{\mathbf{K}}^f_{uu} & \mathbf{0} & -\hat{\mathbf{C}}_{up} & -\hat{\mathbf{C}}_{u\bar{p}} \\ \hat{\mathbf{C}}^T_{uV} & \mathbf{0} & 2/C_P & \mathbf{0} & \mathbf{0} \\ \mathbf{0} & \mathbf{0} & \mathbf{0} & \hat{\mathbf{K}}_{pp} & \hat{\mathbf{K}}_{p\bar{p}} \\ \mathbf{0} & \mathbf{0} & \mathbf{0} & \hat{\mathbf{K}}_{\bar{p}p} & \hat{\mathbf{K}}_{\bar{p}\bar{p}} \end{bmatrix} \tag{4.54}$$

Eliminating the last row and moving the vector of prescribed pressure values $\mathbf{P}^d$ to the right hand side of Equation (4.53) yields

$$\begin{bmatrix} \hat{\mathbf{M}}^h_{uu} & \mathbf{0} & \mathbf{0} & \mathbf{0} \\ \mathbf{0} & \hat{\mathbf{M}}^f_{uu} & \mathbf{0} & \mathbf{0} \\ \mathbf{0} & \mathbf{0} & 0 & \mathbf{0} \\ \mathbf{0} & \hat{\mathbf{C}}^T_{up} & \mathbf{0} & \hat{\mathbf{M}}_{pp} \end{bmatrix} \begin{Bmatrix} \ddot{\mathbf{U}}^h \\ \ddot{\mathbf{U}}^f \\ \ddot{Q} \\ \ddot{\mathbf{P}} \end{Bmatrix} + \begin{bmatrix} \hat{\mathbf{D}}^h_{uu} & \mathbf{0} & \mathbf{0} & \mathbf{0} \\ \mathbf{0} & \hat{\mathbf{D}}^f_{uu} & \mathbf{0} & \mathbf{0} \\ \mathbf{0} & \mathbf{0} & R_L & \mathbf{0} \\ \mathbf{0} & \mathbf{0} & \mathbf{0} & \hat{\mathbf{D}}_{pp} \end{bmatrix} \begin{Bmatrix} \dot{\mathbf{U}}^h \\ \dot{\mathbf{U}}^f \\ \dot{Q} \\ \dot{\mathbf{P}} \end{Bmatrix}$$
$$+ \begin{bmatrix} \hat{\mathbf{K}}^h_{uu} & \hat{\mathbf{K}}_s & \hat{\mathbf{C}}_{uV} & \mathbf{0} \\ \hat{\mathbf{K}}^T_s & \hat{\mathbf{K}}^f_{uu} & \mathbf{0} & -\hat{\mathbf{C}}_{up} \\ \hat{\mathbf{C}}^T_{uV} & \mathbf{0} & 2/C_P & \mathbf{0} \\ \mathbf{0} & \mathbf{0} & \mathbf{0} & \hat{\mathbf{K}}_{pp} \end{bmatrix} \begin{Bmatrix} \mathbf{U}^h \\ \mathbf{U}^f \\ Q \\ \mathbf{P} \end{Bmatrix} = \begin{Bmatrix} \mathbf{F}^h_u \\ \mathbf{F}^f_u \\ 0 \\ \mathbf{F}_p \end{Bmatrix} \tag{4.55}$$

where $\mathbf{F}^f_u$, $\mathbf{F}^h_u$, and $\mathbf{F}_p$ are given by

$$\mathbf{F}^h_u = \mathbf{F}^h, \tag{4.56}$$

$$\mathbf{F}^f_u = \mathbf{F}^f + \hat{\mathbf{C}}_{u\bar{p}}\mathbf{P}^d, \tag{4.57}$$

$$\mathbf{F}_p = -\hat{\mathbf{M}}_{p\bar{p}}\ddot{\mathbf{P}}^d - \hat{\mathbf{K}}_{p\bar{p}}\mathbf{P}^d \tag{4.58}$$

Introducing the transformations $\mathbf{U}^h = \mathbf{\Phi}_h \mathbf{h}_h$, $\mathbf{U}^f = \mathbf{\Phi}_f \mathbf{h}_f$, and $\mathbf{P} = \mathbf{\Phi}_p \mathbf{h}_p$ into Equations (4.55)-(4.58), and premultiplying the first, second, and fourth rows of Equation (4.55) by $\mathbf{\Phi}_h^T$, $\mathbf{\Phi}_f^T$, and $\mathbf{\Phi}_p^T$, respectively, yields

$$\begin{bmatrix} \bar{\mathbf{M}}_{uu}^h & \mathbf{0} & \mathbf{0} & \mathbf{0} \\ \mathbf{0} & \bar{\mathbf{M}}_{uu}^f & \mathbf{0} & \mathbf{0} \\ \mathbf{0} & \mathbf{0} & 0 & \mathbf{0} \\ \mathbf{0} & \bar{\mathbf{C}}_{up}^T & \mathbf{0} & \bar{\mathbf{M}}_{pp} \end{bmatrix} \begin{Bmatrix} \ddot{\mathbf{h}}_h \\ \ddot{\mathbf{h}}_f \\ \ddot{Q} \\ \ddot{\mathbf{P}} \end{Bmatrix} + \begin{bmatrix} \bar{\mathbf{D}}_{uu}^h & \mathbf{0} & \mathbf{0} & \mathbf{0} \\ \mathbf{0} & \bar{\mathbf{D}}_{uu}^f & \mathbf{0} & \mathbf{0} \\ \mathbf{0} & \mathbf{0} & R_L & \mathbf{0} \\ \mathbf{0} & \mathbf{0} & \mathbf{0} & \bar{\mathbf{D}}_{pp} \end{bmatrix} \begin{Bmatrix} \dot{\mathbf{h}}_h \\ \dot{\mathbf{h}}_f \\ \dot{Q} \\ \dot{\mathbf{P}} \end{Bmatrix}$$
$$+ \begin{bmatrix} \bar{\mathbf{K}}_{uu}^h & \bar{\mathbf{K}}_s & \bar{\mathbf{C}}_{uV} & \mathbf{0} \\ \bar{\mathbf{K}}_s^T & \bar{\mathbf{K}}_{uu}^f & \mathbf{0} & -\bar{\mathbf{C}}_{up} \\ \bar{\mathbf{C}}_{uV}^T & \mathbf{0} & 2/C_P & \mathbf{0} \\ \mathbf{0} & \mathbf{0} & \mathbf{0} & \bar{\mathbf{K}}_{pp} \end{bmatrix} \begin{Bmatrix} \mathbf{h}_h \\ \mathbf{h}_f \\ Q \\ \mathbf{P} \end{Bmatrix} = \begin{Bmatrix} \bar{\mathbf{F}}_u^h \\ \bar{\mathbf{F}}_u^f \\ 0 \\ \bar{\mathbf{F}}_p \end{Bmatrix} \tag{4.59}$$

where $\mathbf{\Phi}_h$, $\mathbf{\Phi}_f$, and $\mathbf{\Phi}_p$ are the mass normalized modal matrices associated with the harvester (in *SC* conditions), magnifier, and fluid (with open cavity), respectively, $\mathbf{h}_h$, $\mathbf{h}_f$ and $\mathbf{h}_p$ are their corresponding vectors of modal coordinates.

The different mass normalized vectors and matrices given in Equation (4.59) can be expressed in terms of those in Equation (4.55) as

$$\bar{\mathbf{M}}_{uu}^h = \mathbf{\Phi}_h^T \hat{\mathbf{M}}_{uu}^h \mathbf{\Phi}_h, \quad \bar{\mathbf{M}}_{uu}^f = \mathbf{\Phi}_f^T \hat{\mathbf{M}}_{uu}^f \mathbf{\Phi}_f, \quad \bar{\mathbf{M}}_{uu} = \mathbf{\Phi}_p^T \hat{\mathbf{M}}_{pp} \mathbf{\Phi}_p, \tag{4.60}$$

$$\bar{\mathbf{K}}_{uu}^h = \mathbf{\Phi}_h^T \hat{\mathbf{K}}_{uu}^h \mathbf{\Phi}_h, \quad \bar{\mathbf{K}}_{uu}^f = \mathbf{\Phi}_f^T \hat{\mathbf{K}}_{uu}^f \mathbf{\Phi}_f, \quad \bar{\mathbf{K}}_{pp} = \mathbf{\Phi}_p^T \hat{\mathbf{K}}_{pp} \mathbf{\Phi}_p, \quad \bar{\mathbf{K}}_s = \mathbf{\Phi}_h^T \hat{\mathbf{K}}_s \mathbf{\Phi}_f \tag{4.61}$$

$$\bar{\mathbf{C}}_{uV} = \mathbf{\Phi}_h^T \hat{\mathbf{C}}_{uV}, \quad \bar{\mathbf{C}}_{up} = \mathbf{\Phi}_f^T \hat{\mathbf{C}}_{up} \mathbf{\Phi}_p, \tag{4.62}$$

$$\bar{\mathbf{F}}_u^h = \mathbf{\Phi}_h^T \mathbf{F}_u^h, \quad \bar{\mathbf{F}}_u^f = \mathbf{\Phi}_f^T \mathbf{F}_u^f, \quad \bar{\mathbf{F}}_p = \mathbf{\Phi}_p^T \mathbf{F}_p \tag{4.63}$$

For a harmonic input pressure excitation at a frequency ω such that $\mathbf{P}^d = \mathbf{P}_0^d e^{j\omega t}$, $\bar{\mathbf{F}}_u^h = \bar{\mathbf{F}}_{0u}^h e^{j\omega t}$, $\bar{\mathbf{F}}_u^f = \bar{\mathbf{F}}_{0u}^f e^{j\omega t}$, and $\bar{\mathbf{F}}_p = \bar{\mathbf{F}}_{0p} e^{j\omega t}$, the output solution is assumed also in harmonic form as

$$\mathbf{h}_h = \mathbf{H}_{0h} e^{j\omega t}, \quad \mathbf{h}_f = \mathbf{H}_{0f} e^{j\omega t}, \quad \mathbf{h}_p = \mathbf{H}_{0p} e^{j\omega t}, \quad Q = Q_0 e^{j\omega t} \tag{4.64}$$

Defining the harvester impedance matrix as $\overline{\mathbf{Z}}_h = \overline{\mathbf{K}}_{uu}^h + j\omega\overline{\mathbf{D}}_{uu}^h - \omega^2\overline{\mathbf{M}}_{uu}^h$, the dynamic magnifier impedance matrix as $\overline{\mathbf{Z}}_f = \overline{\mathbf{K}}_{uu}^f + j\omega\overline{\mathbf{D}}_{uu}^f - \omega^2\overline{\mathbf{M}}_{uu}^f$, and the fluid impedance matrix as $\overline{\mathbf{Z}}_p = \overline{\mathbf{K}}_{pp} + j\omega\overline{\mathbf{D}}_{pp} - \omega^2\overline{\mathbf{M}}_{pp}$, substituting Equation (4.64) into Equation (4.59), and carrying out some manipulations, we arrive at the following relations for the output modal amplitudes

$$Q_0 = \frac{\overline{\mathbf{C}}_{uV}^T \mathbf{\Theta}_h^{-1}\left(\overline{\mathbf{F}}_{0u}^h - \overline{\mathbf{K}}_s \mathbf{\Theta}_f^{-1}\overline{\mathbf{F}}_{0u}^f - \overline{\mathbf{K}}_s \mathbf{\Theta}_f^{-1}\overline{\mathbf{C}}_{up}\overline{\mathbf{Z}}_p^{-1}\overline{\mathbf{F}}_{0p}\right)}{\overline{\mathbf{C}}_{uV}^T \mathbf{\Theta}_h^{-1}\overline{\mathbf{C}}_{uV} - j\omega R_L - 2/C_P}, \tag{4.65}$$

$$\mathbf{H}_{0h} = \mathbf{\Theta}_h^{-1}\left(\overline{\mathbf{F}}_{0u}^h - \overline{\mathbf{K}}_s \mathbf{\Theta}_f^{-1}\overline{\mathbf{F}}_{0u}^f - \overline{\mathbf{K}}_s \mathbf{\Theta}_f^{-1}\overline{\mathbf{C}}_{up}\overline{\mathbf{Z}}_p^{-1}\overline{\mathbf{F}}_{0p} - \overline{\mathbf{C}}_{uV} Q_0\right), \tag{4.66}$$

$$\mathbf{H}_{0f} = \mathbf{\Theta}_f^{-1}\left(\overline{\mathbf{F}}_{0u}^f + \overline{\mathbf{C}}_{up}\overline{\mathbf{Z}}_p^{-1}\overline{\mathbf{F}}_{0p} - \overline{\mathbf{K}}_s^T \mathbf{H}_{0h}\right), \tag{4.67}$$

$$\mathbf{H}_{0p} = \overline{\mathbf{Z}}_p^{-1}\left(\overline{\mathbf{F}}_{0p} + \omega^2\overline{\mathbf{C}}_{up}^T \mathbf{H}_{0f}\right) \tag{4.68}$$

where the matrices $\mathbf{\Theta}_h$ and $\mathbf{\Theta}_f$ are given by

$$\mathbf{\Theta}_h = \left(\overline{\mathbf{Z}}_h - \overline{\mathbf{K}}_s \mathbf{\Theta}_f^{-1}\overline{\mathbf{K}}_s^T\right), \tag{4.69}$$

$$\mathbf{\Theta}_f = \left(\overline{\mathbf{Z}}_f - \omega^2\overline{\mathbf{C}}_{up}\overline{\mathbf{Z}}_p^{-1}\overline{\mathbf{C}}_{up}^T\right) \tag{4.70}$$

In order to illustrate the performance of the combined system which includes the effect of the dynamic magnifier, we consider a numerical example where the properties shown in Table 4.1 are used again for comparison purposes. The dynamic magnifier beam has the same geometric and material parameters as those of the harvester substructure (see Table 4.1), except for its thickness which is chosen to be equal to $h_f = 0.8\,mm$. The dynamic magnifier discrete spring stiffness is $k_f = 2.5\,kPa$.

Figure 4.13 shows the electric power *FRF* of the piezoelectric energy harvester for different resistive loads when $p^d = 1\,Pa$.

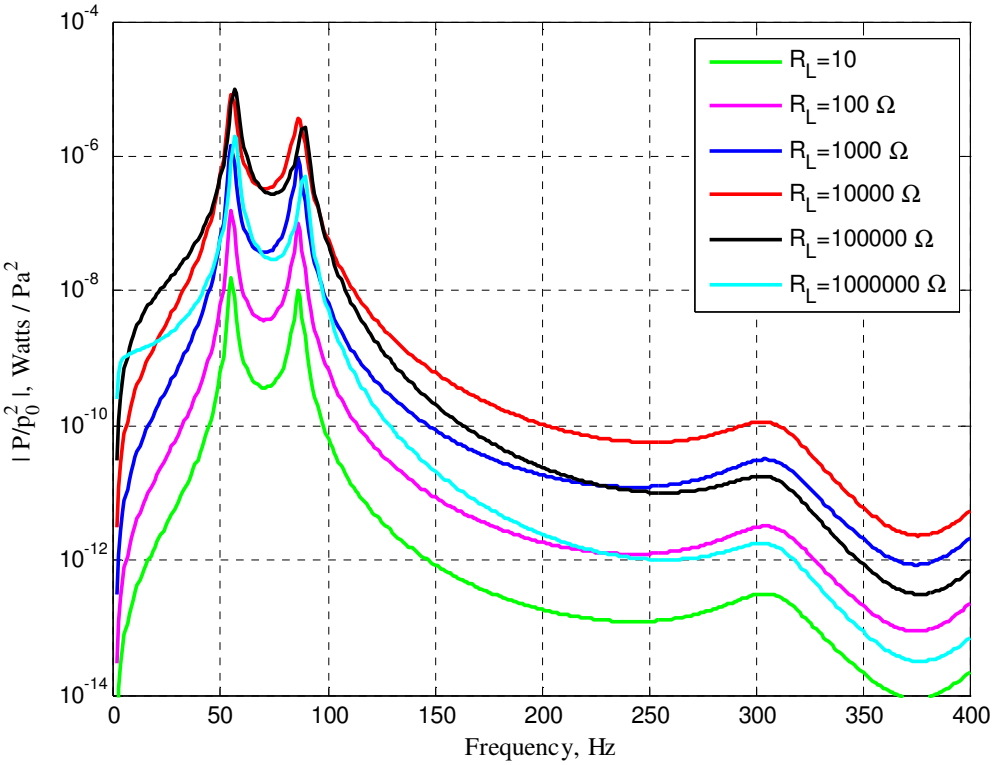

Figure 4.13: Power FRF of the piezoelectric energy harvester for different resistive loads

Figure 4.14 shows the variation of the electric power amplitude with load resistance for excitations at the short-circuit resonant frequencies of the first coupled vibration mode of the combined system (including the effect of the dynamic magnifier) as compared to that of the coupled system without attaching the dynamic magnifier. It is found that the peak electric power harvested from the combined system is $P_{\max}^{sc} = 10.3\,\mu W / Pa$ with $R_L^{sc} = 12\,k\Omega$, whereas the peak electric power harvested from the coupled system without attaching the dynamic magnifier is found to be equal to $P_{\max}^{sc} = 3.5\,\mu W / Pa$ with $R_L^{sc} = 31\,k\Omega$. Accordingly, the use of the

dynamic magnifier has resulted in magnifying the peak harvested power of the coupled system by about 300%.

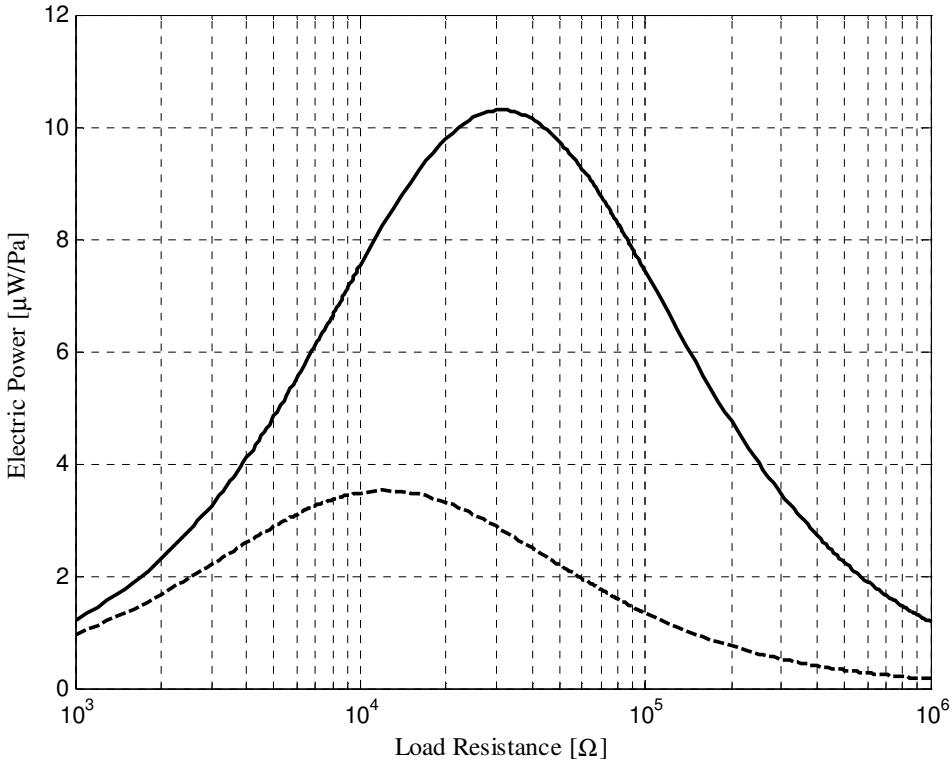

Figure 4.14: Variation of electric power with load resistance at the *SC* resonant conditions of the first coupled vibration mode (——— with magnifier, ▪▪▪▪▪▪▪▪▪ without magnifier)

4.8. A Three-Dimensional Energy Harvesting System

Thus far, the considered examples give a good insight into the behavior and performance characteristics of piezoelectric energy harvesting devices coupled to an acoustic cavity. Yet, these examples are only good for theoretical study since a two-dimensional structural-acoustic coupled system is not a practical problem. A more realistic case would be the three-dimensional extension of the structural-acoustic coupled system considered previously. Figure 4.15 shows a schematic drawing of

such systems where a three-dimensional rigid acoustic cavity is coupled with a bimorph piezoelectric energy harvester plate.

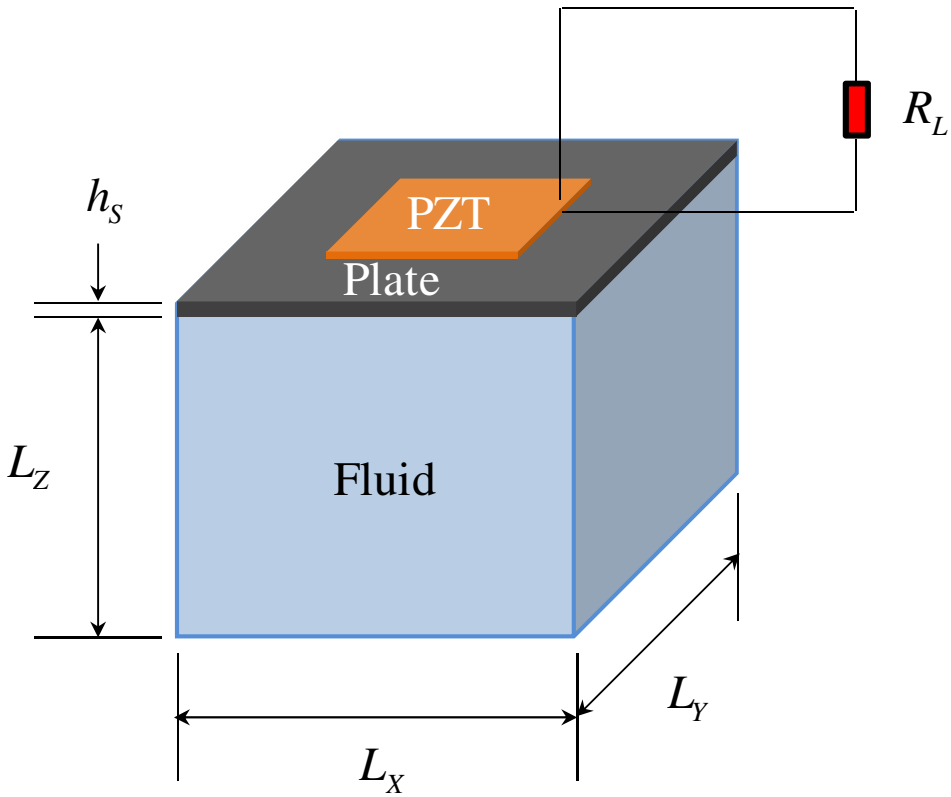

Figure 4.15: The three-dimensional structural-acoustic coupled energy harvesting system

Since the variational equations (Equations (4.15)-(4.17)) were derived for systems of general geometry, they can be used here again. The three-dimensional rigid acoustic cavity is completely filled with air and the cavity is assumed to be open from one side where a persistent harmonic pressure input excitation is applied. The continually vibrating flexible end of the cavity is made of a bimorph piezoelectric energy harvester plate. For simplicity, the thin composite structure is assumed to be in a state of plane-stress and is modeled using the Kirchhoff plate assumptions.

The two piezoelectric patches are fully covered with continuous electrodes of negligible thickness at their top and bottom surfaces, polarized in their transverse directions opposite to each other, and connected in series to a resistive electric load R_L which together with their internal capacitance form an electric circuit that is suitable for energy harvesting purposes [10]. The electric potential in the piezoelectric patches is assumed to be varying linearly in the z-direction (across their thickness) but considered uniform along the x and y coordinates. The fluid pressure inside the cavity is assumed to be varying spatially along the x, y, and z coordinates.

Based on the above assumptions, the reduced piezoelectric-structure constitutive equations can be simplified in matrix-form as

$$\begin{Bmatrix} \sigma_1 \\ \sigma_2 \\ \sigma_6 \\ D_3 \end{Bmatrix} = \begin{bmatrix} \bar{c}_{11}^E & \bar{c}_{12}^E & 0 & -\bar{e}_{31} \\ \bar{c}_{12}^E & \bar{c}_{22}^E & 0 & -\bar{e}_{32} \\ 0 & 0 & \bar{c}_{66}^E & 0 \\ \bar{e}_{31} & \bar{e}_{32} & 0 & \bar{\in}_{33}^{\varepsilon} \end{bmatrix} \begin{Bmatrix} \varepsilon_1 \\ \varepsilon_2 \\ \varepsilon_6 \\ E_3 \end{Bmatrix} \tag{4.71}$$

where the two-dimensional (2-D) plane-stress constants in Equation (4.71) can be obtained in terms of the three-dimensional (3-D) constants as [14]

$$\begin{aligned} &\bar{c}_{11}^E = c_{11}^E - \frac{\left(c_{13}^E\right)^2}{c_{33}^E}, \quad \bar{c}_{12}^E = c_{12}^E - \frac{c_{13}^E c_{23}^E}{c_{33}^E}, \quad \bar{c}_{22}^E = c_{22}^E - \frac{\left(c_{23}^E\right)^2}{c_{33}^E}, \quad \bar{c}_{66}^E = c_{66}^E, \\ &\bar{e}_{31} = e_{31} - \frac{c_{13}^E}{c_{33}^E} e_{33}, \quad \bar{e}_{32} = e_{32} - \frac{c_{23}^E}{c_{33}^E} e_{33} \quad \bar{\in}_{33}^{\varepsilon} = \in_{33}^{\varepsilon} + \frac{e_{33}^2}{c_{33}^E} \end{aligned} \tag{4.72}$$

Moreover, the in-plane strains (ε_1, ε_2, and ε_6) and the transverse electric field E_3 are related to the transverse mechanical displacement u_3 and the electric potential ψ by

$$\varepsilon_1 = z\frac{\partial^2 u_3}{\partial x^2}, \quad \varepsilon_2 = z\frac{\partial^2 u_3}{\partial y^2}, \quad \varepsilon_6 = 2z\frac{\partial^2 u_3}{\partial x \partial y}, \tag{4.73}$$

$$E_3 = -\frac{\partial \psi}{\partial z} = -\frac{V_P}{h_P} \tag{4.74}$$

where V_P ($P = 1, 2$) denotes the voltage between the upper and lower electrodes of the Pth piezoelectric patch with thickness h_P.

The structure domain is discretized using two-dimensional quadrilateral four-node finite elements. Each node has three degrees of freedom which are the transverse mechanical displacement and its derivatives (rotations). On the other hand, the fluid domain is discretized using three-dimensional hexagonal eight-node finite elements where the nodal pressure is the only degree of freedom. Hence, the structure element transverse mechanical displacement and the fluid element pressure can be expressed, respectively, in terms of their nodal values as

$$\begin{aligned} u_3^e &= N_{1S} w_1 + N_{2S}\theta_{1x} + N_{3S}\theta_{1y} + N_{4S} w_2 + N_{5S}\theta_{2x} + N_{6S}\theta_{2y} \\ &+ N_{7S} w_3 + N_{8S}\theta_{3x} + N_{9S}\theta_{3y} + N_{10S} w_4 + N_{11S}\theta_{4x} + N_{12S}\theta_{4y} = \mathbf{N}_S \mathbf{U}^e, \end{aligned} \tag{4.75}$$

$$\begin{aligned} p^e &= N_{1F} p_1 + N_{2F} p_2 + N_{3F} p_3 + N_{4F} p_4 \\ &+ N_{5F} p_5 + N_{6F} p_6 + N_{7F} p_7 + N_{8F} p_8 = \mathbf{N}_F \mathbf{P}^e \end{aligned} \tag{4.76}$$

where w_m, θ_{mx}, and θ_{my} ($m = 1, 2, 3$) denote the nodal transverse mechanical displacements and their corresponding rotations whereas p_n ($n = 1, 2, ..., 8$) denote the nodal pressure values.

Equations (4.42)-(4.44) can be used here again to compute the output modal amplitudes of the harmonically pressure-driven three-dimensional coupled energy harvesting system. In order to illustrate its performance, we consider a numerical

example where the geometric, structure, fluid, and electromechanical parameters of the coupled problem are listed in Table 4.8. Note that the piezoelectric material used here is PZT-5A.

Table 4.6 lists the first six natural frequencies of the composite plate alone when the piezoelectric patches are in *SC* and *OC* electric boundary conditions. Figure 4.16 shows the corresponding mode shapes of the composite plate alone.

Table 4.7 lists the first six natural frequencies of the cavity alone for all-rigid and one-side open fluid boundary conditions. Figure 4.17 and Figure 4.18 show the corresponding mode shapes of the cavity alone.

Table 4.6: First six natural frequencies (*Hz*) of the composite plate alone

MODE	SHORT-CIRCUIT	OPEN-CIRCUIT
1	152.21	153.93
2	278.71	278.71
3	349.90	349.90
4	460.57	460.57
5	483.82	484.11
6	649.16	649.16

Table 4.7: First six natural frequencies (*Hz*) of the cavity alone

MODE	ALL-RIGID	ONE-SIDE OPEN
1	284.14	212.84
2	341.40	355.02
3	427.74	402.31
4	444.18	492.54
5	513.51	611.40
6	547.28	646.75

Table 4.8: Geometric, structure, fluid, and electromechanical properties of the coupled system

Geometric Properties	Value
Size of plate substructure $L_X \times L_Y$	$0.6\ m \times 0.5\ m$
Size of each piezoelectric patch $L_{PX} \times L_{PY}$	$0.3\ m \times 0.2\ m$
Thickness of plate substructure h_S	$6.0\ mm$
Thickness of each piezoelectric patch h_P	$0.6\ mm$
Cavity size $L_X \times L_Y \times L_Z$	$0.6\ m \times 0.5\ m \times 0.4\ m$
Structure Properties	**Value**
Young's Modulus of plate substructure c_{11}^S	$144\ GPa$
Young's Modulus of each piezoelectric patch c_{11}^E	$120.3\ GPa$
Young's Modulus of each piezoelectric patch c_{22}^E	$120.3\ GPa$
Young's Modulus of each piezoelectric patch c_{33}^E	$110.9\ GPa$
Young's Modulus of each piezoelectric patch c_{12}^E	$75.2\ GPa$
Young's Modulus of each piezoelectric patch c_{23}^E	$75.1\ GPa$
Young's Modulus of each piezoelectric patch c_{13}^E	$75.1\ GPa$
Young's Modulus of each piezoelectric patch c_{66}^E	$22.7\ GPa$
Mass density of plate substructure ρ_S	$7700\ kg/m^3$
Mass density of each piezoelectric patch ρ_P	$7800\ kg/m^3$
Poisson's ratio of plate substructure	0.35
Fluid and Electromechanical Properties	**Value**
Mass density of air ρ_F	$1.0\ kg/m^3$
Piezoelectric constant e_{31}	$-5.2\ C/m^2$
Piezoelectric constant e_{32}	$-5.2\ C/m^2$
Piezoelectric constant e_{33}	$15.9\ C/m^2$
Permittivity $\in_{33}^{\varepsilon}$ *	$1800 \times \in_0\ pF/m$
Speed of sound for air c_F	$340\ m/s$

* Permittivity of free space $\in_0 = 8.854\ pF/m$

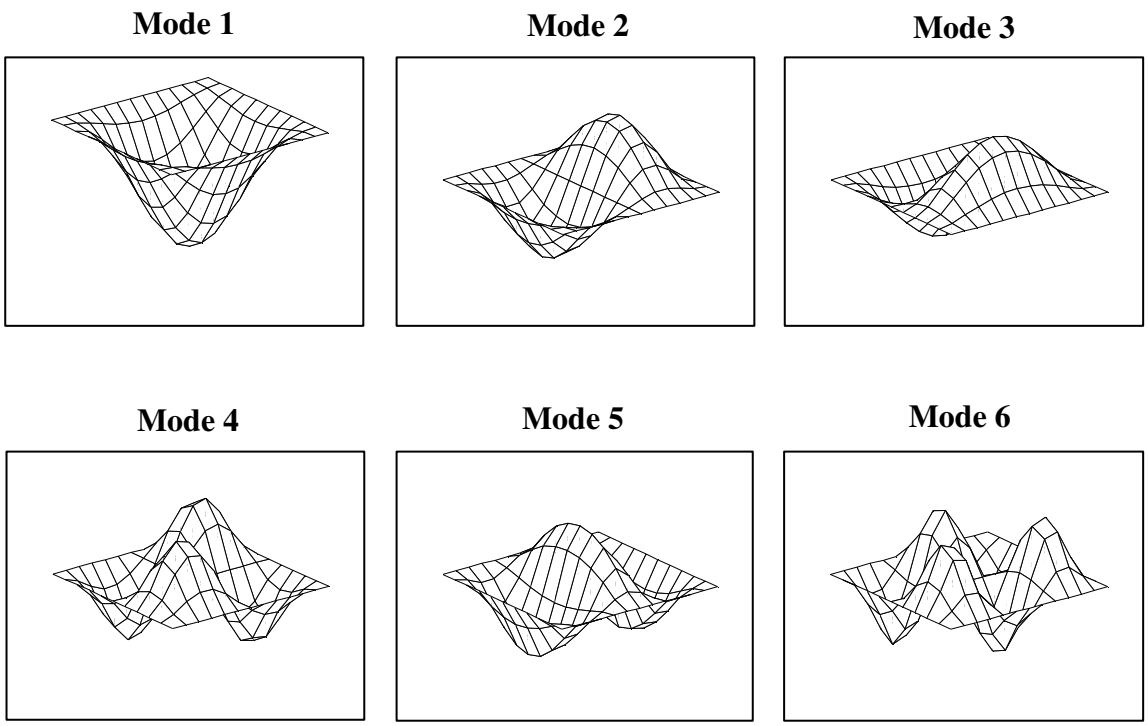

Figure 4.16: First six mode shapes of the composite plate alone

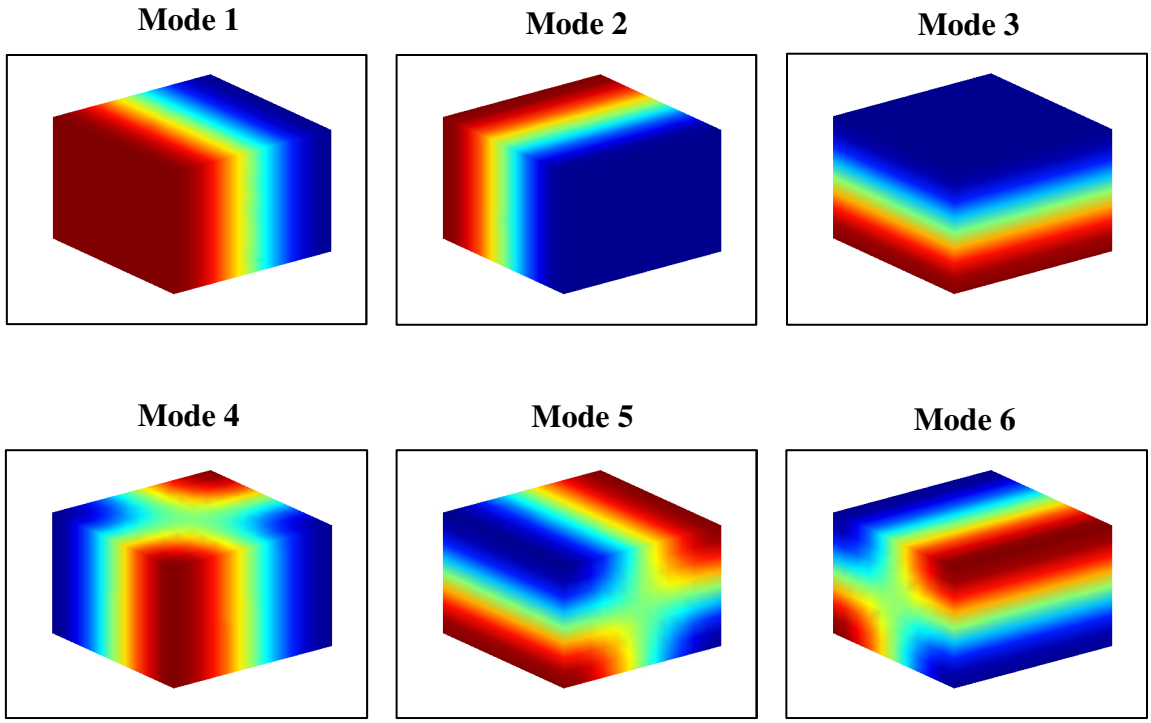

Figure 4.17: First six mode shapes of the rigid cavity alone

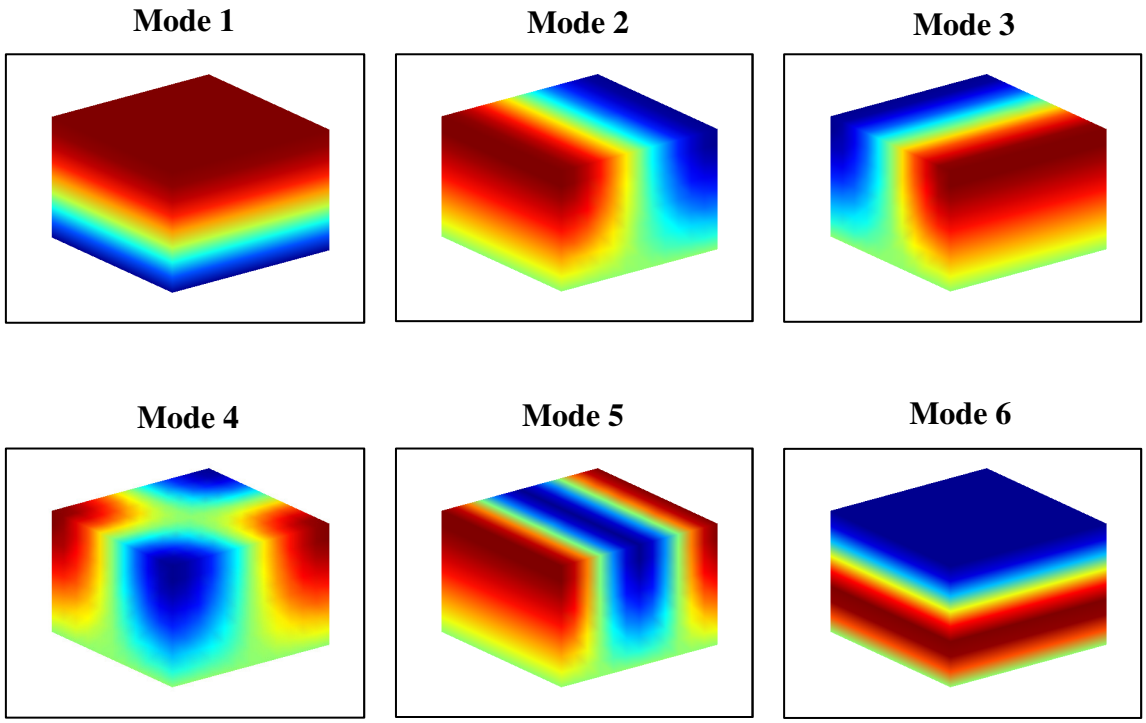

Figure 4.18: First six mode shapes of the one-side open cavity alone

Table 4.9 and Table 4.10 list the first six natural frequencies of the coupled system with rigid cavity and open cavity fluid boundary conditions when the piezoelectric patches are subjected to *SC* and *OC* electric boundary conditions, respectively. Figure 4.19 and Figure 4.20 show the corresponding mode shapes of the coupled system.

Table 4.9: First six natural frequencies (*Hz*) of the coupled system for all-rigid fluid boundary condition

MODE	SHORT-CIRCUIT	OPEN-CIRCUIT
1	152.27	153.99
2	276.56	276.56
3	286.08	286.08
4	339.86	339.86
5	351.15	351.15
6	427.76	427.76

Table 4.10: First six natural frequencies (*Hz*) of the coupled system for one-side open fluid boundary condition

MODE	SHORT-CIRCUIT	OPEN-CIRCUIT
1	151.62	153.33
2	213.47	213.49
3	278.18	278.18
4	349.13	349.13
5	355.42	355.42
6	402.89	402.89

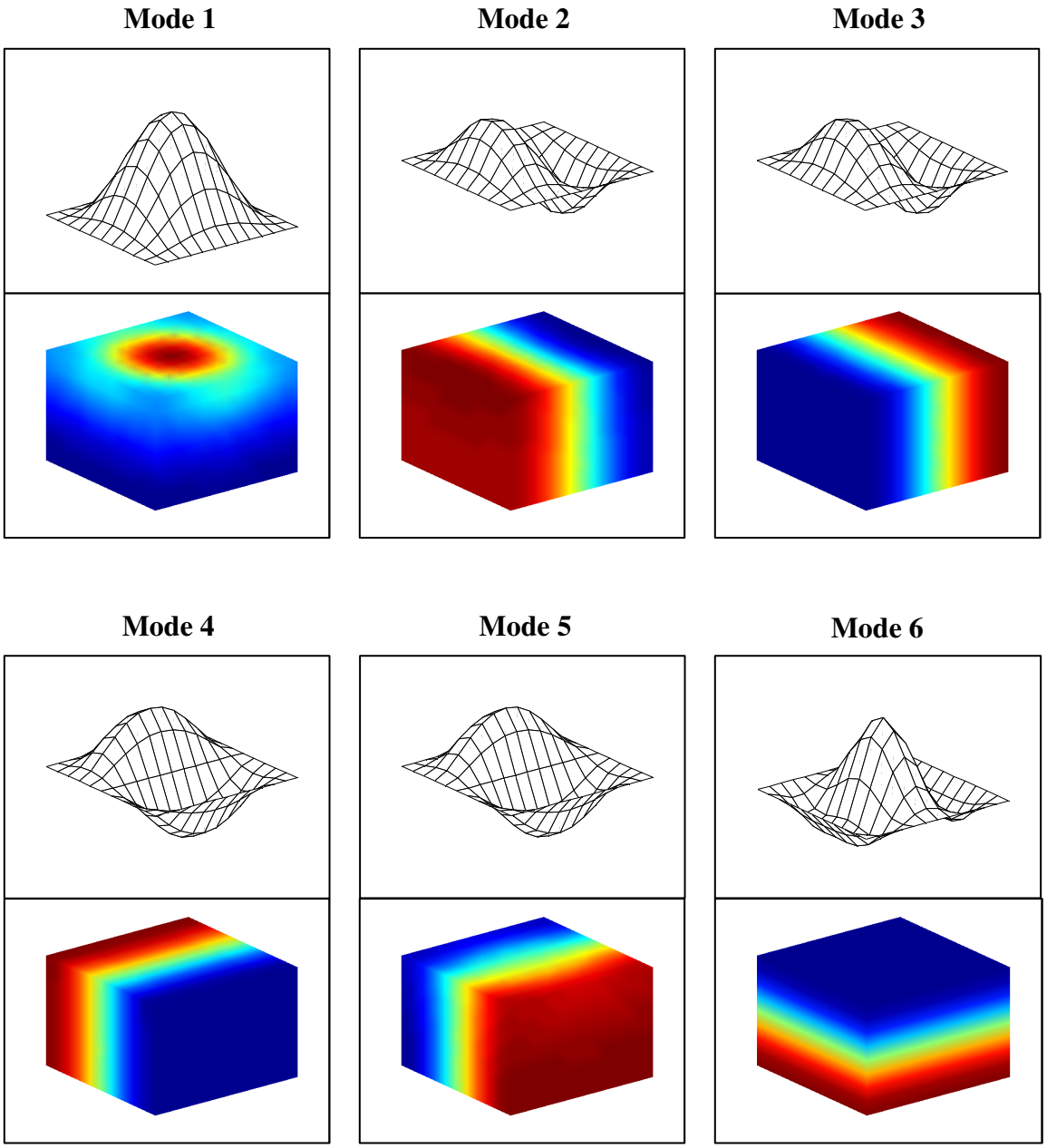

Figure 4.19: First six mode shapes of the coupled system with rigid cavity at the short-circuit condition

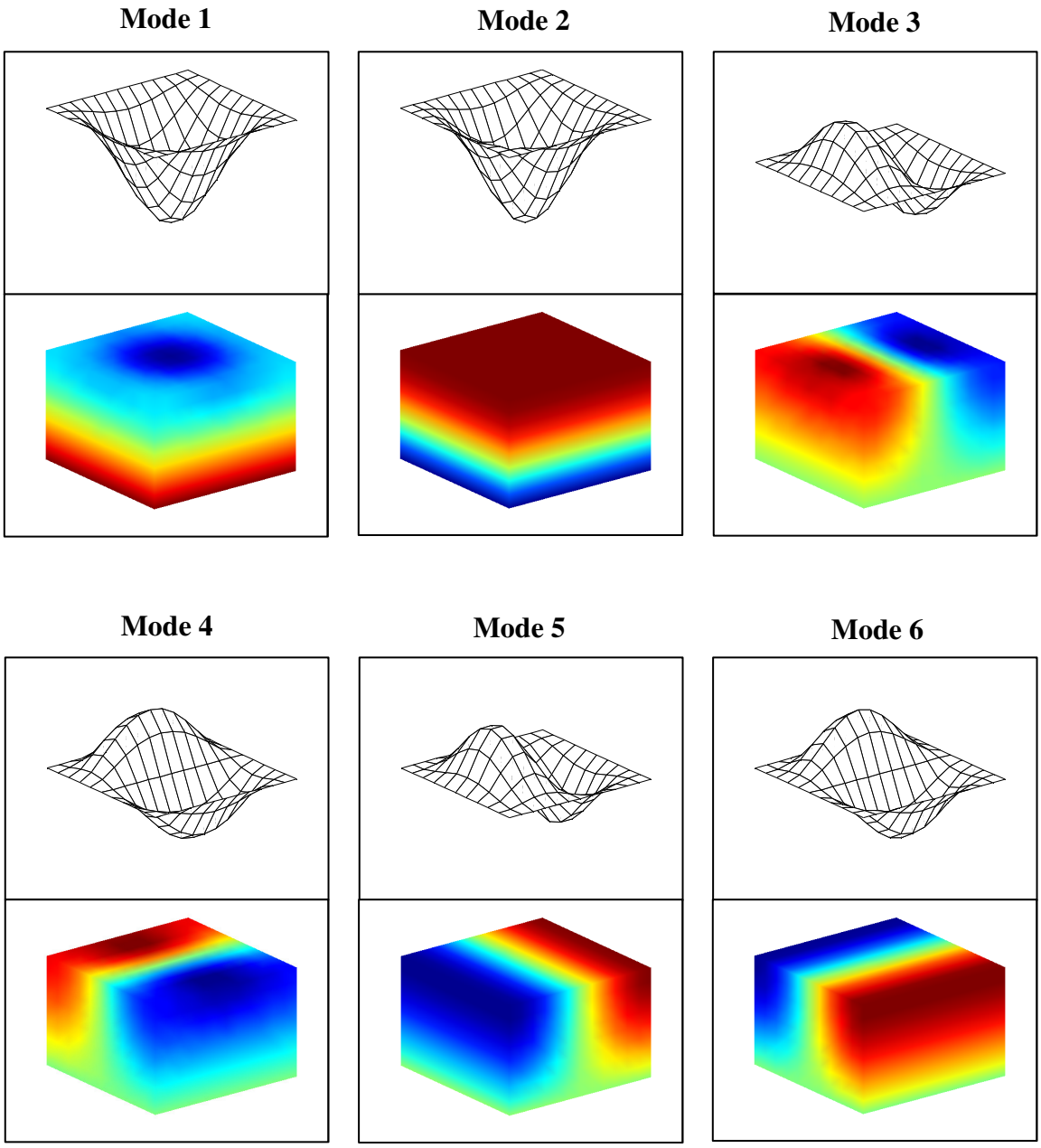

Figure 4.20: First six mode shapes of the coupled system with open cavity at the short-circuit condition

Figure 4.8, Figure 4.9, and Figure 4.10 show, respectively, the electric voltage, current, and power *FRF*s of the piezoelectric energy harvester plate (showing only the first coupled resonant frequency) for different resistive loads when

$p^d = 1Pa$. It can be seen from these electric behaviors that they go in parallel with those obtained earlier for the two-dimensional energy harvesting problem.

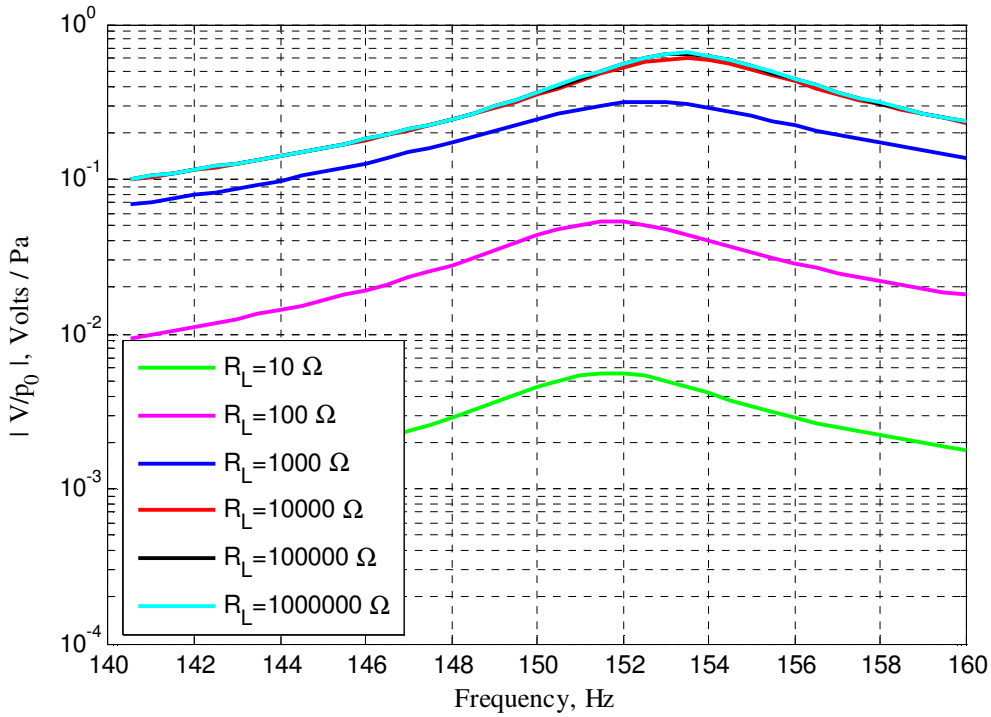

Figure 4.21: Voltage *FRF* of the piezoelectric energy harvester plate for different resistive loads

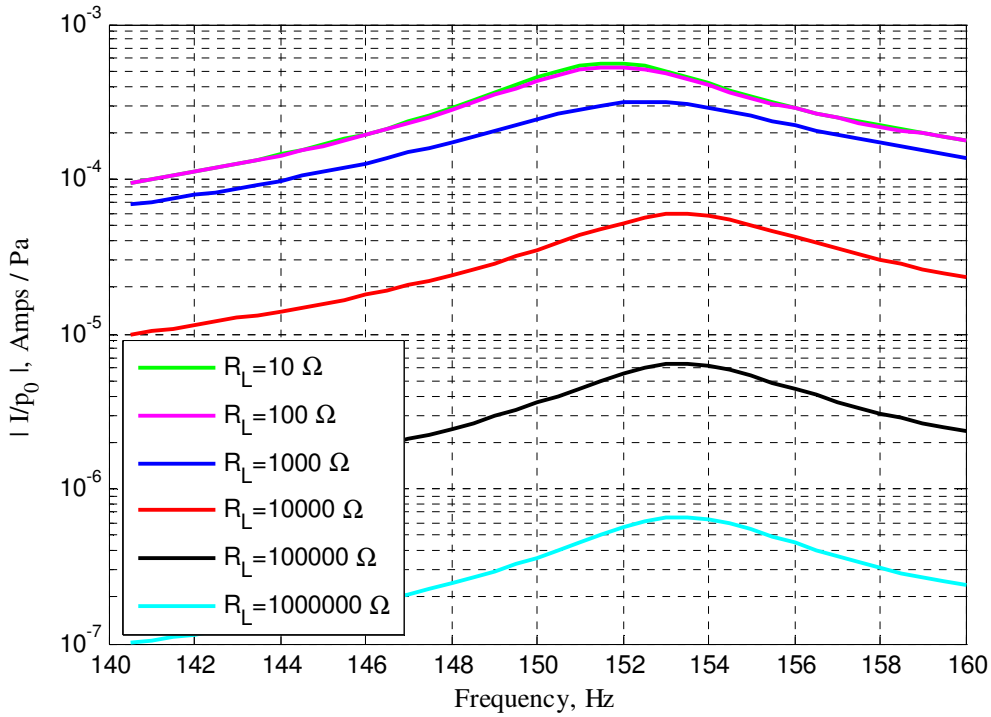

Figure 4.22: Current FRF of the piezoelectric energy harvester plate for different resistive loads

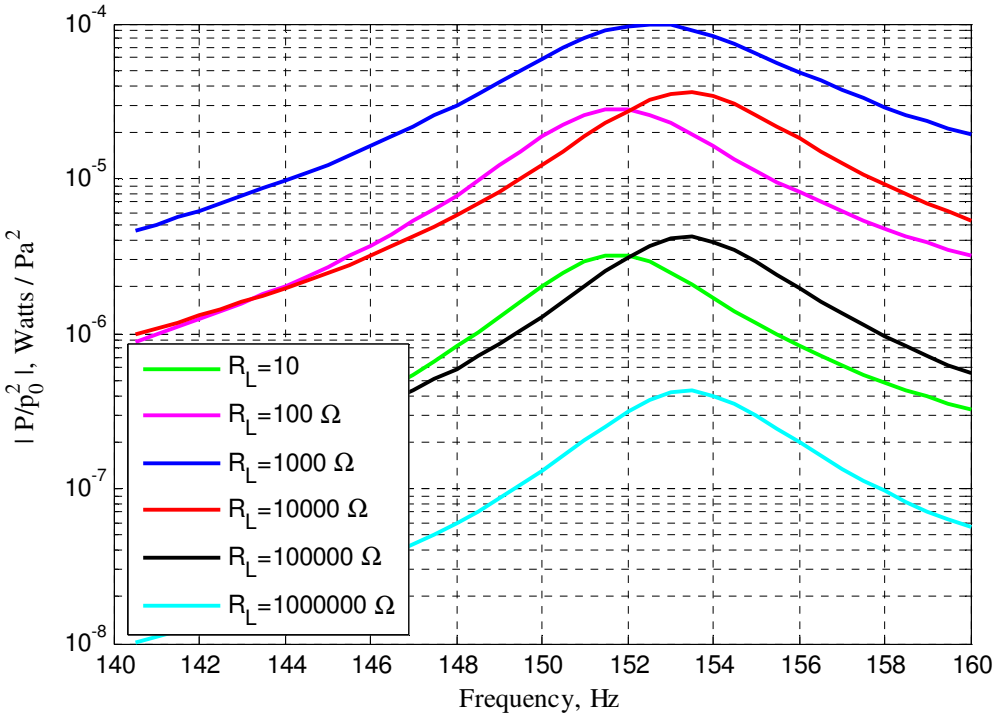

Figure 4.23: Power *FRF* of the piezoelectric energy harvester plate for different resistive loads

4.9. Conclusions

This chapter has presented a generic finite element modeling of piezoelectric energy harvesters which can harness the vibration energy propagating through a rigid acoustic cavity. The model predicts the mechanical displacement and electric power output of the harvester when the cavity is subjected to persistent harmonic pressure input excitations. Detailed analysis is presented of the modal frequencies and the mode shapes of the coupled piezoelectric energy harvester and acoustic cavity system.

The effectiveness of the energy harvester in capturing the vibrational energy resulting from the interaction between the oscillating fluid, filling the cavity, and the piezoelectric harvesting structure is demonstrated when the harvester is connected to

different resistive loads. It was found that the amplitude of the harvester electric voltage increases with increasing the load resistance and that the behavior is monotonic. On the other hand, the amplitude of the harvester electric current decreases with increasing the load resistance but the behavior is still monotonic.

The numerical examples presented to illustrate the behavior of the harvester at short-circuit (*SC*) and open-circuit (*OC*) resonant conditions indicate that the maximum electric power output of the harvester is approximately the same under both conditions.

The presented finite element model can be readily extended and applied to more complex fluid-structure systems where vibrational energy can be harnessed to potentially power various vibration, noise, and health monitoring instrumentation.

Chapter 5

5. Experimental Implementation of Piezoelectric Vibration Energy Harvesting from Coupled Structural-Acoustic Systems

5.1. Introduction

In the context of energy harvesting techniques by using piezoelectric materials, this chapter presents the experimental investigations of the specific problem representing a piezoelectric composite plate coupled with a rectangular acoustic cavity. In Chapter 4, a finite element model was developed to study this kind of problems where the electric power output from the piezoelectric patches is predicted for harmonic pressure input excitations. As a consequence, an experiment has been conducted to validate the previous results. The only difference here is that instead of having an acoustic source to excite the structural-acoustic coupled system from the open end of the cavity, a uniformly distributed load is applied on the outer surface (front surface) of the plate to excite the system mechanically. Figure 5.1 shows the experimental setup needed to predict and validate the previous finite element results. The all-fixed plate substructure is made of aluminum where a piezoelectric patch is attached right in the middle of each side of the plate as shown in Figure 5.2. A speaker is placed a small distance from the outer surface of the plate as the source of excitation to the system. The piezoelectric patches are connected in series to an electric resistive load and the electric power output is measured and compared with the electric power output obtained using the finite element model.

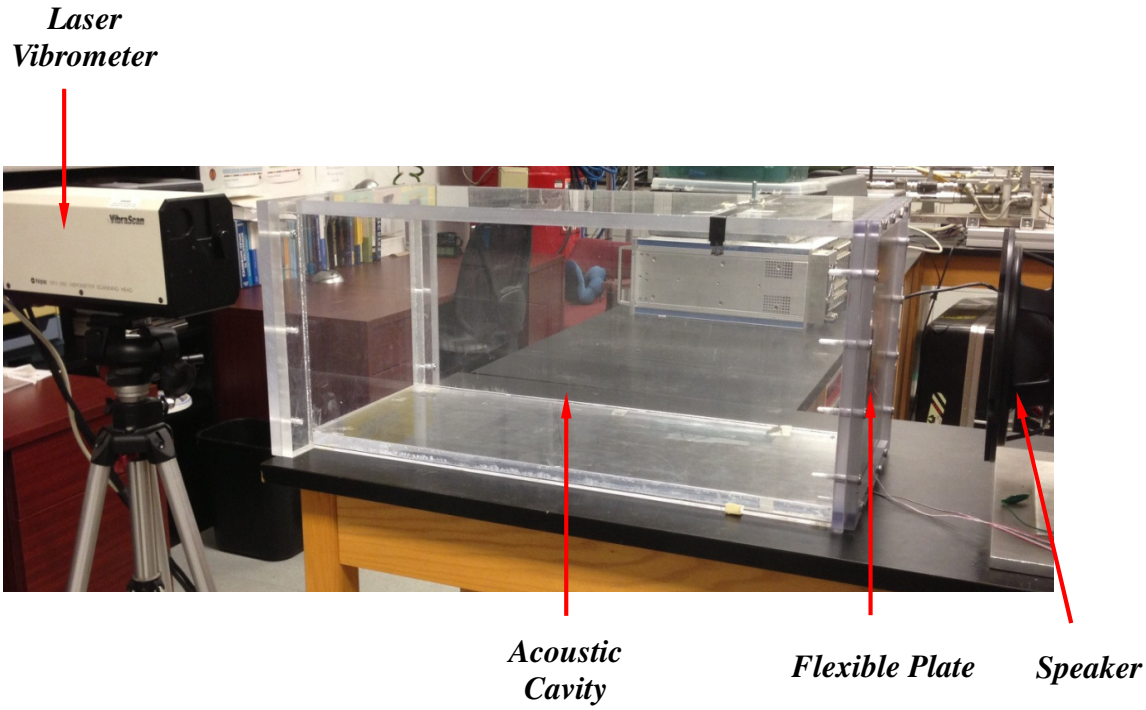

Figure 5.1: A photograph showing the experimental setup of the structural-acoustic coupled system

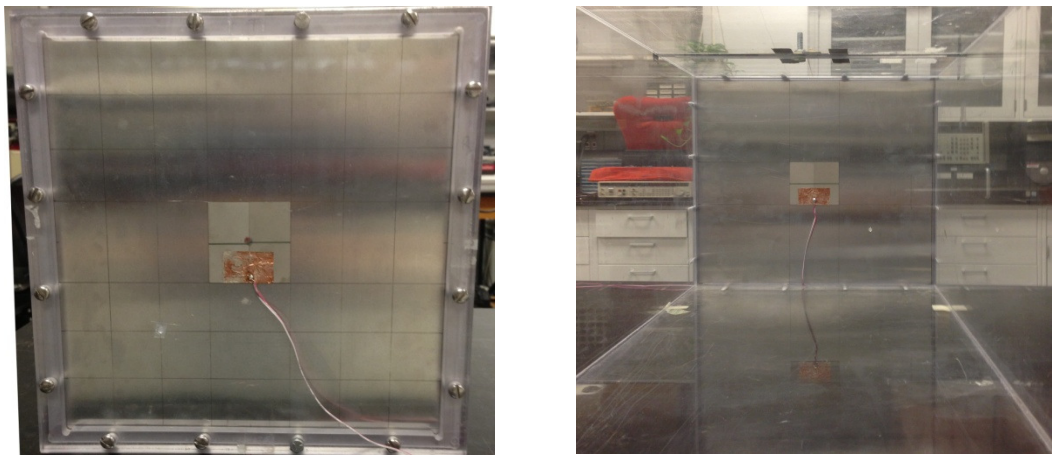

(a) **(b)**

Figure 5.2: Piezoelectric patches connected to the front side (a) and back side (b) of the all-fixed aluminum plate substructure

5.2. Finite Element Modeling

The details of the finite element modeling of piezoelectric energy harvesters from coupled structural-acoustic systems were documented in Chapter 4. However, since the experimental setup used here differs slightly from the one used previously, it is therefore worthwhile to briefly indicate where these differences occur in the mathematical model. The following discussion explains the main differences between the two models.

The following discretized variational equations (Equation (4.33)) of the coupled problem can be written in matrix-form

$$\begin{bmatrix} \hat{\mathbf{M}}_{uu} & \mathbf{0} & \mathbf{0} \\ \mathbf{0} & 0 & \mathbf{0} \\ \hat{\mathbf{C}}_{up}^{T} & \mathbf{0} & \hat{\mathbf{M}}_{pp} \end{bmatrix} \begin{Bmatrix} \ddot{\mathbf{U}} \\ \ddot{Q} \\ \ddot{\mathbf{P}} \end{Bmatrix} + \begin{bmatrix} \hat{\mathbf{D}}_{uu} & \mathbf{0} & \mathbf{0} \\ \mathbf{0} & R_L & \mathbf{0} \\ \mathbf{0} & \mathbf{0} & \hat{\mathbf{D}}_{pp} \end{bmatrix} \begin{Bmatrix} \dot{\mathbf{U}} \\ \dot{Q} \\ \dot{\mathbf{P}} \end{Bmatrix} + \begin{bmatrix} \hat{\mathbf{K}}_{uu} & \hat{\mathbf{C}}_{uV} & -\hat{\mathbf{C}}_{up} \\ \hat{\mathbf{C}}_{uV}^{T} & 2/C_P & \mathbf{0} \\ \mathbf{0} & \mathbf{0} & \hat{\mathbf{K}}_{pp} \end{bmatrix} \begin{Bmatrix} \mathbf{U} \\ Q \\ \mathbf{P} \end{Bmatrix} = \begin{Bmatrix} \mathbf{F}_u \\ 0 \\ \mathbf{0} \end{Bmatrix} \tag{5.1}$$

where $\hat{\mathbf{M}}_{uu}$ and $\hat{\mathbf{K}}_{uu}$ are the mechanical mass and stiffness matrices, $\hat{\mathbf{M}}_{pp}$ and $\hat{\mathbf{K}}_{pp}$ are the fluid mass and stiffness matrices, $\hat{\mathbf{C}}_{uV}$ is the electromechanical coupling matrix, $\hat{\mathbf{K}}_{VV}$ is the electric stiffness matrix, and $\hat{\mathbf{C}}_{up}$ is the fluid-structure coupling matrix. Moreover, $\mathbf{F}_u = \mathbf{F}$ and $\mathbf{Q}$ denote the applied mechanical load and charge vectors, respectively.

Introducing the transformations $\mathbf{U} = \mathbf{\Phi}_u \mathbf{h}_u$ and $\mathbf{P} = \mathbf{\Phi}_p \mathbf{h}_p$ into Equation (5.1), and premultiplying the first and third rows of Equation (5.1) by $\mathbf{\Phi}_u^T$ and $\mathbf{\Phi}_p^T$, respectively, yields

$$\begin{bmatrix} \bar{\mathbf{M}}_{uu} & \mathbf{0} & \mathbf{0} \\ \mathbf{0} & 0 & \mathbf{0} \\ \bar{\mathbf{C}}_{up}^T & \mathbf{0} & \bar{\mathbf{M}}_{pp} \end{bmatrix} \begin{Bmatrix} \ddot{\mathbf{h}}_u \\ \ddot{Q} \\ \ddot{\mathbf{h}}_p \end{Bmatrix} + \begin{bmatrix} \bar{\mathbf{D}}_{uu} & \mathbf{0} & \mathbf{0} \\ \mathbf{0} & R_L & \mathbf{0} \\ \mathbf{0} & \mathbf{0} & \bar{\mathbf{D}}_{pp} \end{bmatrix} \begin{Bmatrix} \dot{\mathbf{h}}_u \\ \dot{Q} \\ \dot{\mathbf{h}}_p \end{Bmatrix}$$
$$+ \begin{bmatrix} \bar{\mathbf{K}}_{uu} & \bar{\mathbf{C}}_{uV} & -\bar{\mathbf{C}}_{up} \\ \bar{\mathbf{C}}_{uV}^T & 2/C_P & \mathbf{0} \\ \mathbf{0} & \mathbf{0} & \bar{\mathbf{K}}_{pp} \end{bmatrix} \begin{Bmatrix} \mathbf{h}_u \\ Q \\ \mathbf{h}_p \end{Bmatrix} = \begin{Bmatrix} \bar{\mathbf{F}}_u \\ 0 \\ \mathbf{0} \end{Bmatrix} \tag{5.2}$$

where $\mathbf{\Phi}_u$ and $\mathbf{\Phi}_p$ are the mass normalized modal matrices associated with the structure (in *SC* conditions) and fluid (with open cavity), respectively, $\mathbf{h}_u$ and $\mathbf{h}_p$ are their corresponding vectors of modal coordinates.

For a harmonic input excitation at a frequency ω such that $\bar{\mathbf{F}}_u = \bar{\mathbf{F}}_{0u} e^{j\omega t}$, the output solution is assumed also in harmonic form as

$$\mathbf{h}_u = \mathbf{H}_{0u} e^{j\omega t}, \quad \mathbf{h}_p = \mathbf{H}_{0p} e^{j\omega t}, \quad Q = Q_0 e^{j\omega t} \tag{5.3}$$

Defining the structure and fluid impedance matrices, respectively, as $\bar{\mathbf{Z}}_u = \bar{\mathbf{K}}_{uu} + j\omega\bar{\mathbf{D}}_{uu} - \omega^2\bar{\mathbf{M}}_{uu}$ and $\bar{\mathbf{Z}}_p = \bar{\mathbf{K}}_{pp} + j\omega\bar{\mathbf{D}}_{pp} - \omega^2\bar{\mathbf{M}}_{pp}$, substituting Equation (5.3) into Equation (5.2), and carrying out some manipulations, we arrive at the following relations for the output modal amplitudes

$$Q_0 = \frac{\bar{\mathbf{C}}_{uV}^T \mathbf{\Theta}^{-1} \left(\bar{\mathbf{F}}_{0u} + \bar{\mathbf{C}}_{up} \bar{\mathbf{Z}}_p^{-1} \bar{\mathbf{F}}_{0p} \right)}{\bar{\mathbf{C}}_{uV}^T \mathbf{\Theta}^{-1} \bar{\mathbf{C}}_{uV} - j\omega R_L - 2/C_P}, \tag{5.4}$$

$$\mathbf{H}_{0u} = \mathbf{\Theta}^{-1} \left(\bar{\mathbf{F}}_{0u} + \bar{\mathbf{C}}_{up} \bar{\mathbf{Z}}_p^{-1} \bar{\mathbf{F}}_{0p} - \bar{\mathbf{C}}_{uV} Q_0 \right), \tag{5.5}$$

$$\mathbf{H}_{0p} = \bar{\mathbf{Z}}_p^{-1} \left(\bar{\mathbf{F}}_{0p} + \omega^2 \bar{\mathbf{C}}_{up}^T \mathbf{H}_{0u} \right) \tag{5.6}$$

where the matrix $\mathbf{\Theta}$ is given by

$$\mathbf{\Theta} = \left(\bar{\mathbf{Z}}_u - \omega^2 \bar{\mathbf{C}}_{up} \bar{\mathbf{Z}}_p^{-1} \bar{\mathbf{C}}_{up}^T \right) \tag{5.7}$$

5.3. Experimental and Numerical Results

The geometric, structure, fluid, and electromechanical parameters of the experimental setup shown in Figure 5.1 are listed in Table 5.1. The aluminum plate substructure is fixed from its four sides and the rectangular acoustic cavity is assumed to be rigid and filled completely with air.

Before going through an energy harvesting analysis, the fundamental natural frequency is obtained from the experiment and is compared with the one obtained numerically using the finite element model. The experiment shows that this frequency has a value of f_1=61.61 Hz whereas the one obtained numerically has a value of f_1=61.40 Hz. The fundamental natural mode is the focus of the subsequent energy harvesting results.

The fundamental mode shape of the composite plate is also compared for the experiment vs. numerical model. Here, a scanning laser vibrometer is used for this purpose where the frequency of excitation is set at the obtained fundamental natural frequency of the coupled system. Figure 5.3 shows such comparison and a good agreement is observed. The corresponding mode shape of the acoustic cavity is also included to show the internal pressure distribution.

Figure 5.4 shows the experimental vs. numerical output voltage of the coupled system for different electric load resistances. It can be seen from the plots that the proposed numerical model very well captures the experimental behavior of the energy harvester.

Table 5.1: Geometric, structure, fluid, and electromechanical properties of the experimental setup shown in Figure 5.1

Geometric Properties	Value
Size of plate substructure $L_X \times L_Y$	$0.34\ m \times 0.34\ m$
Size of each piezoelectric patch $L_{PX} \times L_{PY}$	$64\ mm \times 64\ mm$
Thickness of plate substructure h_S	$0.83\ mm$
Thickness of each piezoelectric patch h_P	$0.51\ mm$
Cavity size $L_X \times L_Y \times L_Z$	$0.34\ m \times 0.34\ m \times 0.762\ m$
Structure Properties	**Value**
Young's Modulus of plate substructure c_{11}^S	$69\ GPa$
Young's Modulus of each piezoelectric patch c_{11}^E	$120.3\ GPa$
Young's Modulus of each piezoelectric patch c_{22}^E	$120.3\ GPa$
Young's Modulus of each piezoelectric patch c_{33}^E	$110.9\ GPa$
Young's Modulus of each piezoelectric patch c_{12}^E	$75.2\ GPa$
Young's Modulus of each piezoelectric patch c_{23}^E	$75.1\ GPa$
Young's Modulus of each piezoelectric patch c_{13}^E	$75.1\ GPa$
Young's Modulus of each piezoelectric patch c_{66}^E	$22.7\ GPa$
Mass density of plate substructure ρ_S	$2700\ kg/m^3$
Mass density of each piezoelectric patch ρ_P	$7800\ kg/m^3$
Poisson's ratio of plate substructure	0.33
Fluid and Electromechanical Properties	**Value**
Mass density of air ρ_F	$1.0\ kg/m^3$
Piezoelectric constant e_{31}	$-5.2\ C/m^2$
Piezoelectric constant e_{32}	$-5.2\ C/m^2$
Piezoelectric constant e_{33}	$15.9\ C/m^2$
Permittivity $\in_{33}^{\varepsilon}$ *	$1800 \times \in_0\ pF/m$
Speed of sound for air c_F	$340\ m/s$

* Permittivity of free space $\in_0 = 8.854\ pF/m$

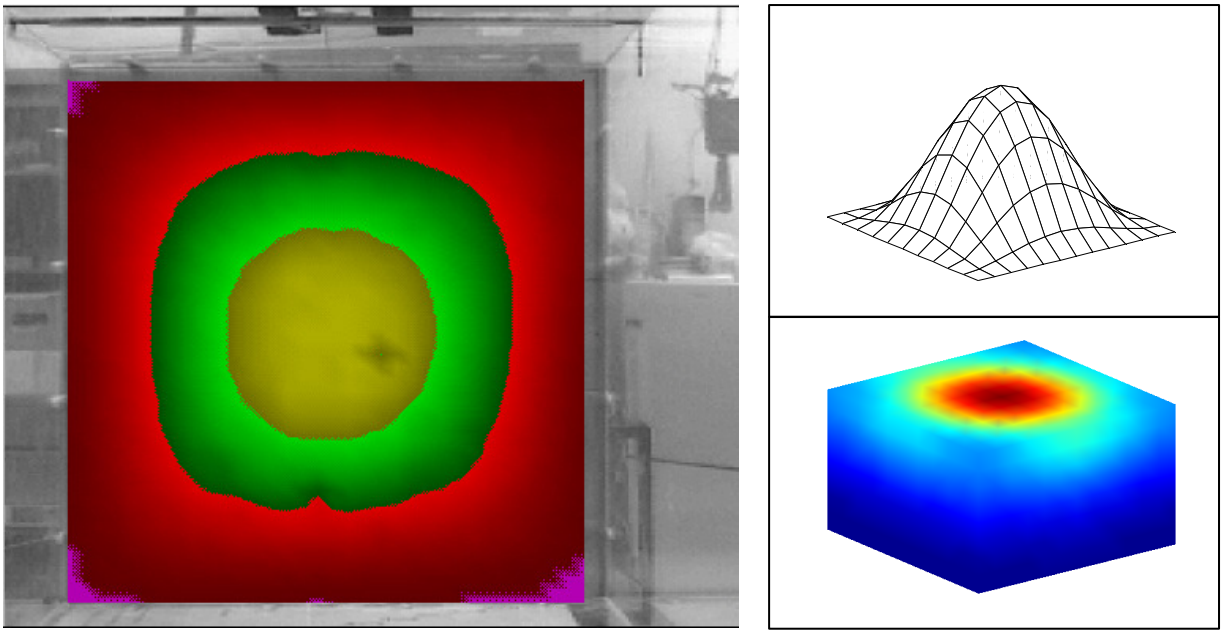

(a) **(b)**

Figure 5.3: Fundamental mode shape of the coupled system: (a) Experimental (plate), (b) Numerical (plate and acoustic cavity)

Figure 5.5 shows the variation of the experimental vs. numerical power output of the coupled system with electric load resistance at the *SC* resonant conditions of the first coupled vibration mode. Here, it can also be seen that the proposed finite element model captures the experimental behavior for the maximum power output achieved from the energy harvester as well as the optimal resistance needed to maintain that maximum power value. The optimal resistance is found to be R_L=30 $K\Omega$ and the corresponding electric power has a value of P_{max}=39.58 μW.

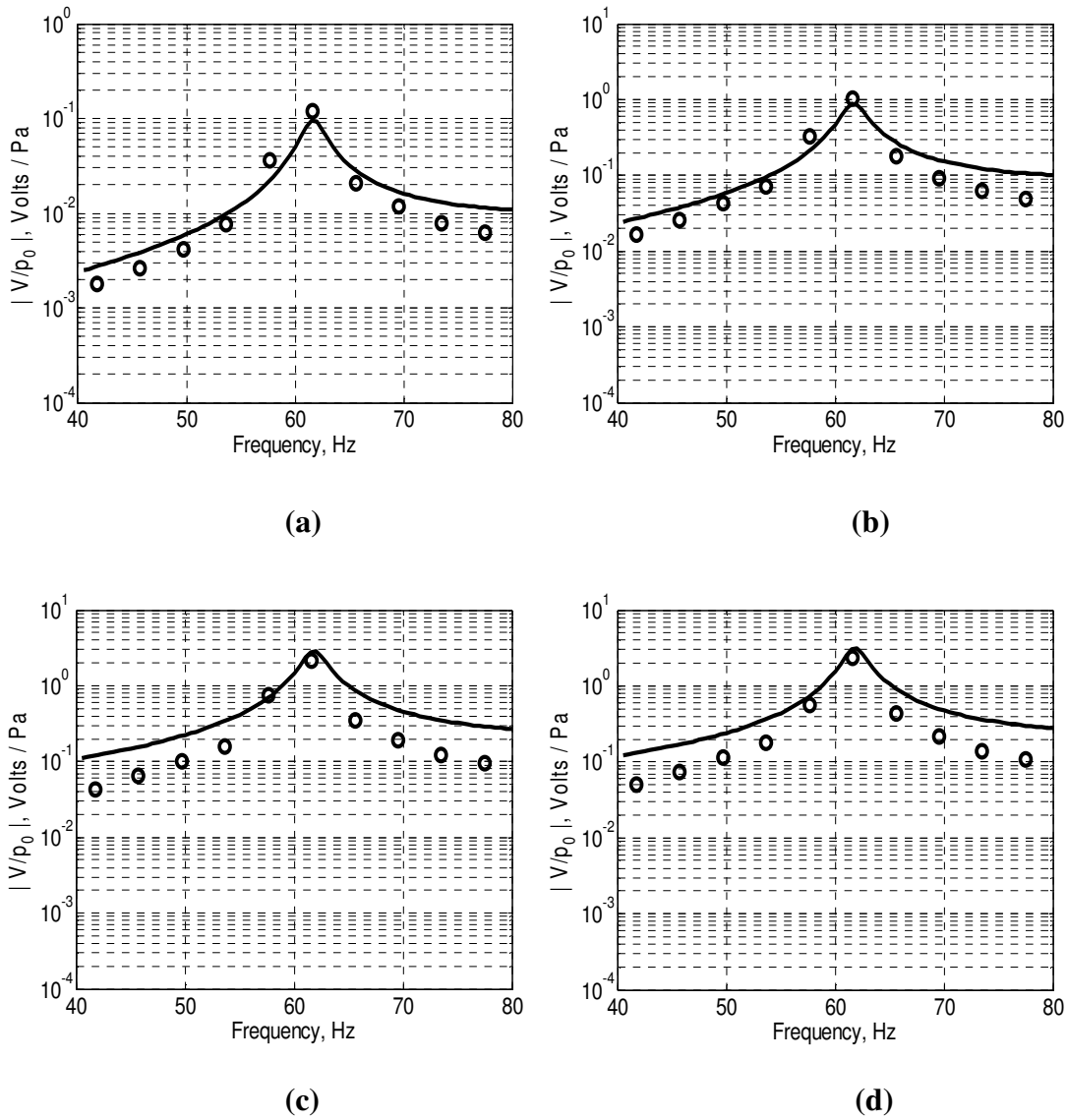

Figure 5.4: Experimental ○ vs. numerical ▬▬ output voltage of the coupled system for: (a) R_L=*1 kohm*, (b) R_L=*10 kohm*, (c) R_L=*100 kohm*, and (d) R_L=*1 Mohm*

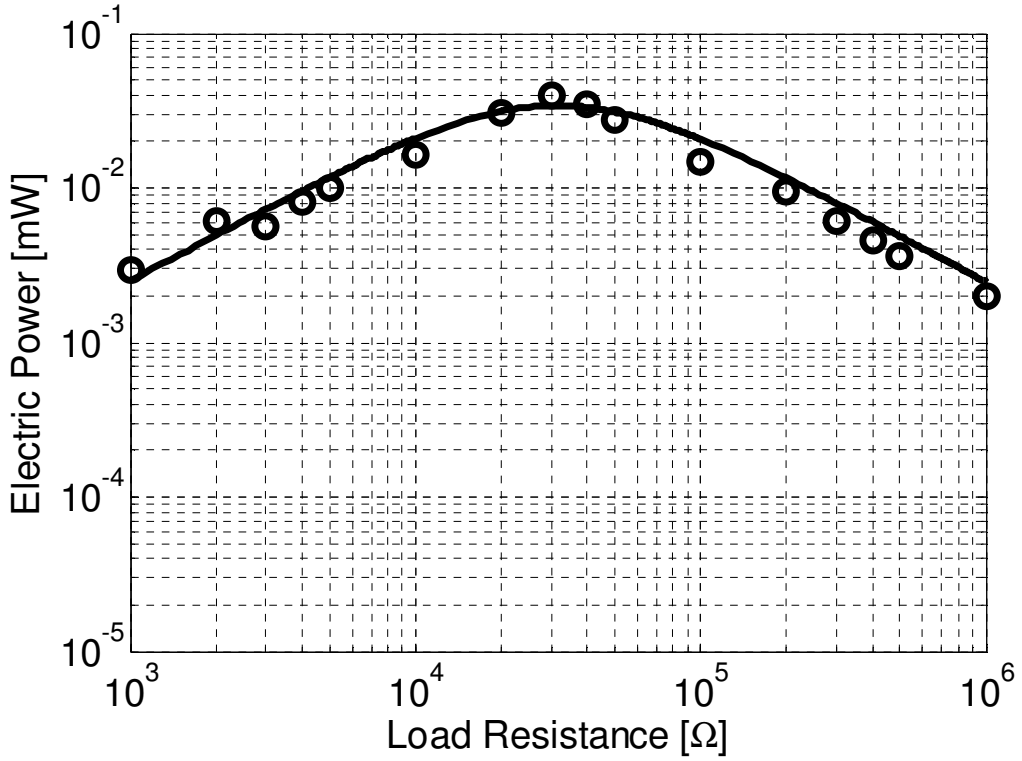

Figure 5.5: Variation of electric power with load resistance at the SC resonant conditions of the first coupled vibration mode (Experimental ○ vs. numerical ———)

5.4. Summary

This chapter has presented an experimental validation of the theoretical model developed in Chapter 4 to predict the energy harvesting from a plate coupled with a rectangular acoustic cavity. In the experimental set-up, the energy associated with the vibration of the plate is harvested using piezoelectric patches connected in series to an electric resistive load and the electric power output is measured and compared with the electric power output obtained using the finite element model at the SC resonant conditions of the first coupled vibration mode.

The obtained experimental results agree closely with the predictions of the finite element model. In particular, the developed finite element model captures the

experimental behavior for the maximum power output achieved from the energy harvester as well as the optimal resistance needed to maintain that maximum power value. It is found that the optimal resistance is R_L=30 $K\Omega$ and the corresponding electric power has a value of P_{max}=39.58 μW.

Further work is needed to provide the experimental energy harvesting system with dynamic magnification capabilities and utilize the obtained results to validate the prediction of a modified finite element model that would account for the behavior of the dynamic magnifier system.

Chapter 6

6. Conclusions and Future Work

6.1. Summary

This dissertation has presented a comprehensive theoretical and experimental study of the fundamentals and the underlying phenomena governing the operation of piezoelectric vibration energy harvesting from coupled fluid-structure systems. Analytical and finite element models are developed based on variational formulations to describe the energy harvesting from uncoupled structural elements as well as structural elements coupled with acoustic cavities. The developed models are augmented also with dynamic magnification means to enhance the energy harvesting capabilities and enable harnessing the vibration energy over a broader operating frequency range.

The predictions of all the models are validated experimentally using beam and plate like structural elements. Close agreements are demonstrated between the theoretical predictions and the obtained experimental results.

In Chapter 2, a class of cantilevered piezoelectric energy harvesters is considered. The theory governing the operation of this class of energy harvesters has been developed using distributed parameter and finite element methods. Numerical examples are presented to illustrate the merits of the *CPEHDM* in comparison with the conventional piezoelectric energy harvesters (*CPEH*). It was shown that with

proper selection of the design parameters of the *CPEHDM*, the harvested electric power can be amplified by a factor of 5 (*i.e.,* 500 percent) as compared to the *CPEH* and the effective bandwidth of the energy harvester can be widened to cover side bands that are about $\pm 21\%$ of the resonant frequency of the *CPEH*. The predictions of the distributed parameter model are compared with those obtained using the finite element approach and excellent agreement of the two models is observed for all the considered examples. The obtained results demonstrate the feasibility of the *CPEHDM* as a simple and effective means for enhancing the magnitude and spectral characteristics of the *CPEH*.

In Chapter 3, the feasibility of the concept of cantilevered piezoelectric energy harvesters with dynamic magnifier (*CPEHDM*) is demonstrated experimentally. The performance characteristics are validated against the predictions of a finite element model developed in Chapter 2. The obtained results illustrate the metrics of the *CPEHDM* in comparison with the conventional piezoelectric energy harvester (*CPEH*). Also, it is shown that the *CPEHDM* is a simple and effective means for enhancing the magnitude and spectral characteristics of the *CPEH*.

In Chapter 4, a finite element modeling is developed to model piezoelectric energy harvesters which can harness the vibration energy propagating through a rigid acoustic cavity. The model predicts the mechanical displacement and electric power output of the harvester when the cavity is subjected to persistent harmonic pressure input excitations. Detailed analysis is presented of the modal frequencies and the mode shapes of the coupled piezoelectric energy harvester and acoustic cavity system both in the 2-D and 3-D configurations.

The effectiveness of the energy harvester in capturing the vibrational energy resulting from the interaction between the oscillating fluid, filling the cavity, and the piezoelectric harvesting structure is demonstrated when the harvester is connected to different resistive loads. It was found that the amplitude of the harvester electric voltage increases with increasing the load resistance and that the behavior is monotonic. On the other hand, the amplitude of the harvester electric current decreases with increasing the load resistance but the behavior is still monotonic.

In Chapter 5, the experimental investigation of energy harvesting from a plate coupled with a rectangular acoustic cavity is considered. The energy associated with the vibration of the plate is harvested using piezoelectric patches that are bonded to it. A finite element model that differs slightly from the one developed in Chapter 4 is considered here. The predictions of the model are validated experimentally and the comparisons show excellent agreement between the two outputs.

It is important to note that the theoretical and experimental tools developed, in this dissertation, provide invaluable means for designing a wide variety of efficient energy harvesters for harnessing the vibrational energy inside automobiles, helicopters, aircraft, and other types of structures that interact internally or externally with a fluid medium. With such harnessed energy, a slew of on-board sensors can be powered to enable the continuous monitoring of the condition and health of these structures without the need for external power sources.

6.2. Recommendations and Future Work

In spite of the fact that this dissertation has presented a comprehensive theoretical and experimental study of the fundamentals and the underlying

phenomena governing the operation of piezoelectric vibration energy harvesting from coupled fluid-structure systems, it has opened also the door for many problems that can be considered as a natural extension to the presented study. For example, this dissertation has been limited to the study of basic structural elements such as beams and plates interacting with generic rectangular acoustic cavities. Therefore a natural extension of this work is to consider more complex structures interacting with acoustic cavities that are of more general configurations. This will enable the study of a wide variety of efficient energy harvesters for harnessing the vibrational energy inside automobiles, helicopters, aircraft, and other types of structures that interact internally or externally with a fluid medium.

Also, the presented study has also been limited to structures and/or fluid media which are excited tonally with sinusoidal excitations. A natural extension of this work can deal with structures and/or fluid media which are subjected to random excitation to closely emulate many practical situations.

Further studies are needed to consider more realistic harvesting circuitry other than resistively loaded systems. For example, the effect of resistive and inductive loading should be considered. Furthermore, the effect of including energy conditioning circuitry such as rectifiers, DC-to-DC converters, switching and non-switching circuitry should be accounted for.

Practical implementations of the proposed concepts are also essential to be considered for future studies where the dynamics of the energy storage and management systems should be included along with the structure and interacting fluids.

Appendices

Electromechanical Model Analogy:

1. Analytical Model:

<u>Equations of Motion:</u>

$$\frac{d^2\eta_r(t)}{dt^2}+2\zeta_r\omega_r\frac{d\eta_r(t)}{dt}+\omega_r^2\eta_r(t)-\Psi_r\frac{dQ(t)}{dt}=f_r(t)$$

$$\sum_{r=1}^{\infty}\Psi_r\frac{d\eta_r(t)}{dt}+\frac{C_p}{2}R_L^2\frac{d^2Q}{dt^2}+R_L\frac{dQ}{dt}=0$$

<u>Solution:</u>

$$Q(t)=\frac{\sum_{r=1}^{\infty}\frac{j\Psi_r F_r}{\omega_r^2-\omega^2+j2\zeta_r\omega_r\omega}}{\omega\frac{C_p}{2}R_L^2-jR_L+\sum_{r=1}^{\infty}\frac{\omega\Psi_r^2}{\omega_r^2-\omega^2+j2\zeta_r\omega_r\omega}}e^{j\omega t}$$

$$w_{rel}(x,t)=\sum_{r=1}^{\infty}\left[\frac{F_r+j\omega\Psi_r Q_0}{\omega_r^2-\omega^2+j2\zeta_r\omega_r\omega}W_r(x)\right]e^{j\omega t}$$

<u>Terminology:</u>

$$\Psi_r=\Gamma\left.\frac{dW_r(x)}{dx}\right|_{x=L}$$

$$F_r=\omega^2W_b\left[m_t\int_0^L W_r(x)\,dx+M_fW_r(0)+MW_r(L)\right]-j\omega W_bc_a\int_0^L W_r(x)\,dx$$

2. Finite Element Model:

<u>Equations of Motion:</u>

$$\bar{\mathbf{M}}_{uu}\ddot{\boldsymbol{\eta}} + \bar{\mathbf{D}}_{uu}\dot{\boldsymbol{\eta}} + \bar{\mathbf{K}}_{uu}\boldsymbol{\eta} - \boldsymbol{\Psi}\dot{Q} = \bar{\mathbf{F}}$$

$$\boldsymbol{\Psi}^T\dot{\boldsymbol{\eta}} + \frac{C_P}{2}R_L^2\ddot{Q} + R_L\dot{Q} = 0$$

<u>Solution:</u>

$$Q(t) = \frac{j\boldsymbol{\Psi}^T\bar{\mathbf{Z}}_u^{-1}\bar{\mathbf{F}}_0}{\omega\frac{C_P}{2}R_L^2 - jR_L + \omega\boldsymbol{\Psi}^T\bar{\mathbf{Z}}_u^{-1}\boldsymbol{\Psi}}e^{j\omega t}$$

$$\mathbf{U}(t) = \boldsymbol{\Phi}_u\bar{\mathbf{Z}}_u^{-1}\left(\bar{\mathbf{F}}_0 + j\omega\boldsymbol{\Psi}Q_0\right)e^{j\omega t}$$

<u>Terminology:</u>

$$\boldsymbol{\Psi} = \Gamma\bar{\mathbf{B}}$$

$$\bar{\mathbf{F}}_0 = \omega^2\boldsymbol{\Phi}_u^T\mathbf{M}_{uu}\boldsymbol{\Delta}_{base} - j\omega\boldsymbol{\Phi}_u^T\mathbf{D}_a\boldsymbol{\Delta}_{base}$$

Bibliography

[1] **ANSI/IEEE, 1987**, American National Standards/Institute of Electrical and Electronics Engineers "Standard on Piezoelectricity", ANSI/IEEE STD: 176-1987, IEEE, New York.

[2] **Roundy S., 2005**. On the effectiveness of vibration-based energy harvesting, *Journal of Intelligent Material Systems and Structures*, Vol. **16**, pp. 809-823.

[3] **Priya S., and Inman D.J., 2009**. *Energy Harvesting Technologies*, Springer, New York.

[4] **Erturk A., and Inman D.J., 2011**. *Piezoelectric Energy Harvesting*, John Wiley, UK.

[5] **Williams C.B., and Yates R.B., 1996**. Analysis of a micro-electric generator for microsystems, *Sensors and Actuators* A, Vol. **52**, pp. 8-11.

[6] **Daqaq M.F., Renno J.M. Farmer J.R., and Inman D.J., 2007**. Effects of system parameters and damping on an optimal vibration-based energy harvester, *Proceedings of the 48th AIAA/ASME/ASCE/AHS/ASC Structures, Structural Dynamics, and Materials Conference*, Honolulu, USA, 23-26 A, AIAA-2007-2361, pp. 1-11.

[7] **duToit N., 2005**. *Modeling and Design of a MEMS Piezoelectric Vibration Energy Harvester*, Master's Thesis, Massachusetts Institute of Technology, Cambridge, MA.

[8] **duToit, N., Wardle, B., and Kim, S.-G., 2006**. Design considerations for MEMS-scale piezoelectric mechanical vibration energy harvesters, *Integrated Ferroelectrics*, Vol. **71,** pp. 121–160.

[9] **Erturk A., and Inman D.J., 2008a**. Issues in mathematical modeling of piezoelectric energy harvesters, *Smart Materials and Structures*, **17**, 065016.

[10] **Erturk, A., and Inman D.J., 2008b**. A distributed parameter electromechanical model for cantilevered piezoelectric energy harvesters, *Journal of Vibration and Acoustics*, Vol. **130**, 041002.

[11] **Erturk, A., and Inman D.J., 2008c**. An experimentally validated bimorph cantilever model for piezoelectric energy harvesting from base excitations, *Journal of Vibration and Acoustics*, Vol. **18**, 025009.

[12] **Adhikari, S., Friswell, M. I., and Inman, D.J., 2009**. Piezoelectric energy harvesting from broadband random vibrations, *Smart Materials and Structures,* Vol. **18,** pp. 115005 1-5.

[13] **Aladwani, A., Arafa, M., Aldraihem, O., and Baz, A., 2012**. Cantilevered piezoelectric energy harvester with a dynamic magnifier, *Journal of Vibration and Acoustics*, Vol. **134**, 031004.

[14] **DeMarqui Jr. C., Erturk, A., and Inman, D.J., 2009**. An electromechanical finite element model for piezoelectric energy harvesting plates, *Journal of Sound and Vibration*, Vol. **327**, pp. 9-25.

[15] **El-Sabbagh A., and Baz A., 2011**. Maximization of the harvested power from piezoelectric bimorphs with multiple electrodes under dynamic excitation, *Finite Elements in Analysis and Design*, Vol. **47**, pp. 1232-1241.

[16] **Kong N.A., Ha D.S., Etrurk, A., and Inman, D.J., 2010**. Resistive impedance matching circuit for piezoelectric energy harvesting, *Journal of Intelligent Material Systems and Structures*, Vol. 21, pp. 1293-1302.

[17] **Liang J., and Liao W.H., 2010**. Impedance matching for improving piezoelectric energy harvesting systems, *Proceedings of Active and Passive Smart Structures and Intelligent Systems*, ed. by M. N. Ghassemi-Nejhad, SPIE Vol. 7643, pp. K-1-12, San Diego, CA.

[18] **Stephen N.G., 2006**. On the maximum power transfer theorem within electromechanical systems, *Proceedings Of the IMECH, Journal of Mechanical Engineering Science, Part C*:, Vol. **220,** pp. 1261-1267.

[19] **Chen Y.C., Wu S., and Chen P.C., 2004**. The impedance-matching design and simulation on high power electro-acoustical transducer, *Sensors and Actuators: A*, Vol. **115,** pp. 38-45.

[20] **Wu W.J., Chen Y.Y., Lee B.S., He J.J., and Pen Y.T., 2006**. Tunable resonant frequency power harvesting devices, *Proceedings of Smart Structures and Materials: Damping and Isolation*, Vol. 6169, edited by W. Clark, M. Ahmadian, and A. Lumsdaine.

[21] **Badel A., Guyomar D., Lefeuvre E., and Richard C., 2006**. Piezoelectric energy harvesting using a synchronized switch technique, *Journal of Intelligent Material Systems and Structures,* Vol. **17**, pp. 831–839.

[22] **Renno J.M., Daqaq M.F. and Inman D.J., 2009**. On the optimal energy harvesting from a vibration source, *Journal of Sound and Vibration*, Vol. **320,** pp. 386-405.

[23] **Xue H., Hu Y. and Wang Q.M., 2008**. Broadband piezoelectric energy harvesting devices using multiple bimorphs with different operating

frequencies, *IEEE Transactions on Ultrasonics, Ferroelectrics, and Frequency Control*, Vol. **55**, No. 9, pp. 2104-2108.

[24] **LeFeuvre E., Badel A., Richard C., and Guyomar D., 2007**. Energy harvesting using piezoelectric materials: case of random vibrations, *Journal of Electroceramic,* Vol. 19 , pp. 349–355.

[25] **Moehlis J., DeMartini B.E., Rogers J.L., and Turner K.L, 2009**. Turner, Exploiting nonlinearity to provide broadband energy harvesting, Paper#DSCC2009-2542, in: *Proceedings of the ASME 2009 Dynamic Systems and Control Conference,* D***SC***C2009, Hollywood, California, USA.

[26] **Meirovitch L., 2001**. *Fundamentals of Vibrations*, McGraw-Hill, New York.

[27] **Morand H.J.P., and Ohayon R., 1995**. *Fluid–Structure Interaction*, John Wiley, New York.

[28] **Olson L.G. and Bathe K.J., 1985**. Analysis of fluid–structure interactions. A direct symmetric coupled formulation based on the fluid velocity potential, *Computers and Structures*, Vol. **21**, pp. 21–32.

[29] **Everstine G.C., 1981**. A symmetric potential formulation for fluid–structure interaction, *Journal of Sound and Vibration*, Vol. **79**, pp. 157-160.

[30] **de Souza S.M., and Pedroso L.J., 2009**. Study of flexible wall acoustic cavities using beam finite element, *Mechanics of Solids in Brazil*, eds. H.S. da Costa Mattos and Marcílio Alves, pp. 223-237.

[31] **Akl W., El-Sabbagh A., Al-Mitani K., and Baz A., 2009**. Topology optimization of a plate coupled with acoustic cavity, *International Journal of Solids and Structures,* Vol. **46**, pp. 2060-2074.

[32] **Shields W., Ro J., and Baz A., 1998**. Control of sound radiation from a plate into an acoustic cavity using active piezoelectric damping composites, *Smart Materials and Structures*, Vol. **7**, pp. 1-11.

[33] **Ro J., and Baz A., 1999**. Control of sound radiation from a plate into an acoustic cavity using active constrained layer damping, *Smart Materials and Structures*, Vol. **8**, pp. 292-300.

[34] **Lefèvre J., and Gabbert U., 2003**. Finite element simulation of smart lightweight structures for active vibration and interior acoustic control, *Technische Mechanik*, Vol. **23**, pp. 59-69.

[35] **Larbi W., Deü J.F., and Ohayon R., 2006**. A new finite element formulation for internal acoustic problems with dissipative walls, *International Journal for Numerical Methods in Engineering*, Vol. **68**, pp. 381-399.

[36] **Larbi W., Deü J.F., and Ohayon R., 2007**. Vibration of axisymmetric composite piezoelectric shells coupled with internal fluid, *International Journal for Numerical Methods in Engineering*, Vol. **71**, pp. 1412-1435.

[37] **Deü J.F., Larbi W., and Ohayon R., 2008a**. Piezoelectric structural acoustic problems: symmetric variational formulations and finite element results, *Computer Methods in Applied Mechanics and Engineering*, Vol. **197,** pp. 1715-1724.

[38] **Deü J.F., Larbi W., and Ohayon R., 2008b**. Vibration and transient response of structural-acoustic interior coupled systems with dissipative interface, *Computer Methods in Applied Mechanics and Engineering*, Vol. **197,** pp. 4894-4905.

[39] **DeMarqui Jr. C., Vieira W.G.R, Erturk, A., and Inman, D.J., 2011**. Modeling and analysis of piezoelectric energy harvesting from aeroelastic vibrations using the doublet-lattice method, *Journal of Vibration and Acoustics,* Vol. **133**, 011033-1.

[40] **Arafa M., Akl W., Majeed M., Al-Hussain K., and Baz A., 2010**. Energy Harvesting of Gas Pipeline Vibration, Paper#7643-20, *Proceeding of the SPIE Conference on Active and Passive Smart Structures and Integrated Systems*, Vol. 7643, edited by Mehrdad N. Ghasemi-Nejhad, San Diego, CA.